

Effect of Pre-Oxidation and Thermal Exposure on the Microstructure of Superalloys and Thermal Barrier Coating Systems

by

Megan Walker

A thesis submitted to the Faculty of Graduate and Postdoctoral Affairs
in partial fulfillment of the requirements for the degree of

Master of Applied Science

in

Mechanical Engineering

Carleton University

Ottawa, Ontario

© 2016

Megan Walker

Effect of Pre-Oxidation and Thermal Exposure on the Microstructure of Superalloys and Thermal Barrier Coating Systems

By

Megan Walker

A thesis submitted to the Faculty of Graduate and Postdoctoral Affairs in partial fulfillment of
the requirements for the degree of

Master of Applied Science

in

Mechanical Engineering

Professor Xiao Huang, Thesis Supervisor

Dr. Qi Yang, Thesis Co-Supervisor

Professor Metin I. Yaras, Chair, Department of Mechanical and Aerospace Engineering

Abstract

Thermal barrier coatings (TBCs) enable the nickel-base superalloy gas turbine blades of modern gas turbine engines to run at their highest possible temperatures. Currently, a bond coat (BC) is utilized to adhere the yttria-stabilized zirconia (YSZ) top coat to the nickel-base superalloy substrate. However, the addition of this manufacturing step increases cost. In this study, three nickel-based superalloys: IN-738, CMSX-4 and Rene N5 are considered. Isothermal oxidation studies were conducted at 1150°C in atmosphere for holding times ranging from 30 minutes to 16 hours. YSZ top coats were applied directly to the nickel-base superalloy René N5 isothermally oxidized for 2hrs at 1150°C in atmosphere. Rene N5 oxidized at this time and temperature produced the most adherent, dense and uniform α -Al₂O₃ scale which was anticipated to enhance YSZ adhesion. YSZ coatings were then applied using suspension plasma spraying technology (SPS). Coatings of dense vertically cracked (DVC) and columnar morphologies were applied. Following YSZ application, the samples were subjected to a diffusion heat treatment in vacuum at 1080°C to promote YSZ/substrate adhesion. These samples were then cyclically and isothermally tested in atmosphere at 1150°C. Both SPS DVC and SPS Columnar coatings were found to have poor adhesion (delaminated in less than 25 cycles). The lack of adequate α -Al₂O₃ coverage, the rapid formation of spinel and grit blasting prior to coating deposition were determined to be the primary causes of poor performance.

Acknowledgements

Firstly, I would like to thank my supervisor Prof. Xiao Huang for her guidance, support and patience throughout this endeavour. I would also like to thank my co-supervisor Dr. Qi Yang for his feedback, insight and assistance with SEM and XRD analyses.

I would also like to thank the National Research Council of Canada for providing access to equipment, facilities and personnel which made this research possible.

I would like to thank my good friend Aditya Chattopadhyay who endured the trials and tribulations of undergraduate studies with me and who without I would not have the same understanding and appreciation of engineering that I do today.

And finally, I would like to thank my parents Douglas and Celeste Walker who have always been there for me and supported me in all that I do.

Table of Contents

Abstract	iii
Acknowledgements.....	iv
Table of Contents	v
List of Tables.....	viii
List of Figures	x
Nomenclature	xiv
1 Introduction, Objectives and Scope of Thesis.....	1
2 Literature Review	3
2.1 Nickel-Based Superalloys.....	5
2.1.1 IN-738.....	11
2.1.2 CMSX-4.....	12
2.1.3 René N5.....	14
2.2 Coatings	15
2.2.1 Diffusion Coatings.....	17
2.2.2 Overlay Coatings	18
2.2.3 Thermal Barrier Coatings.....	19
2.3 Theory.....	22
2.3.1 Thermodynamics	22
2.3.2 Oxidation Mechanisms	24
2.3.3 Oxidation Kinetics	26
2.3.4 Adhesion	27
2.3.5 Growth Stress	28
2.4 High Temperature Oxidation of Nickel-Based Superalloys	30
2.4.1 α -Al ₂ O ₃	30

2.4.2	Spinel.....	31
2.4.3	Reactive Elements.....	32
2.4.4	Other Elements	34
2.4.5	IN-738.....	35
2.4.6	CMSX-4.....	36
2.4.7	René N5.....	36
2.5	TBC system with no Bond Coat	37
3	Equipment, Sample Preparation and Experimental Procedures	39
3.1	Equipment	39
3.1.1	Buehler Automatic Grinder/Polisher	39
3.1.2	Struers Secotom-10	40
3.1.3	Atmospheric Furnace.....	40
3.1.4	Cyclic Furnace	41
3.1.5	Vacuum Furnace	41
3.1.6	SEM	42
3.1.7	XRD.....	43
3.2	Sample Preparation	44
3.2.1	Un-Coated	45
3.2.2	Coated.....	46
3.2.3	Preparation of Cross-Sections	46
3.2.4	Polished Samples	47
3.3	Experimental Procedures	48
3.3.1	Assessment of Samples Prior to Testing.....	48
3.3.2	Oxidation Testing of Uncoated IN-738, CMSX-4 and René N5	48
3.3.3	Oxidation Testing of Coated René N5.....	49
3.3.3.1	Coated René N5 Cycled to Failure.....	49
3.3.3.2	Cyclic Oxidation Testing of Coated René N5 Samples	50
3.3.3.3	Isothermal Oxidation Testing of Coated René N5	51

4	Results	53
4.1	Assessment of Samples Prior to Testing	53
4.1.1	IN-738.....	53
4.1.2	CMSX-4.....	56
4.1.3	René N5.....	59
4.1.4	René N5 SPS DVC	61
4.1.5	René N5 SPS Columnar	63
4.2	Oxidation Results of Uncoated IN-738, CMSX-4 and René N5.....	65
4.2.1	IN-738.....	66
4.2.2	CMSX-4.....	75
4.2.3	René N5.....	82
4.3	Oxidation Results of Coated René N5	96
4.3.1	René N5 SPS DVC	96
4.3.2	René N5 SPS Columnar	102
5	Discussion	109
5.1	Oxidation of IN-738, CMSX-4 and René N5.....	109
5.2	Coated Samples	114
6	Conclusions and Future Work	119
	References.....	123
	Appendix A	132

List of Tables

Table 1: Elements Required Producing a Certain Effect in a Nickel-Based Superalloy	8
Table 2: Composition of IN-738	11
Table 3: Composition of CMSX-4	12
Table 4: Composition of René N5	14
Table 5: Oxide structure of René N5.....	37
Table 6: Isothermal oxidation testing parameters	49
Table 7: Parameters for incremental cyclic oxidation testing.....	51
Table 8: Isothermal oxidation testing of coated samples.....	52
Table 9: Composition of IN-738	53
Table 10: IN-738: a) Average composition of Regions 1, 2 and 3, b) Difference between average composition of Regions 1, 2 and 3 and the composition provided in Table 9	54
Table 11: Composition of CMSX-4	56
Table 12: CMSX-4: a) Average composition of Regions 1 and 2, b) Difference between average composition of Regions 1 and 2 and the composition provided in Table 11	57
Table 13: Composition of René N5	59
Table 14: René N5 a) Average composition of Regions 1, 2 and 3, b) Difference between average composition of Regions 1, 2 and 3 and composition provided in Table 13	60
Table 15: Composition of regions identified in Figure 29.....	62
Table 16: Composition of regions identified in Figure 30.....	64
Table 17: Composition of regions identified in Figure 33.....	70
Table 18: Composition of regions identified in Figure 34.....	72
Table 19: Composition of regions identified in Figure 38.....	78

Table 20: Composition of regions identified in Figure 39.....	80
Table 21: Composition of regions identified in Figure 45.....	85
Table 22: Composition of regions identified in Figure 46.....	86
Table 23: Composition of regions identified in Figure 47.....	88
Table 24: Composition of regions identified in Figure 48.....	90
Table 25: Composition of regions identified in Figure 51.....	95
Table 26: Composition of regions identified in Figure 52.....	97
Table 27: Composition of regions identified in Figure 53.....	99
Table 28: Composition of regions identified in Figure 55.....	101
Table 29: Composition of regions identified in Figure 56.....	104
Table 30: Composition of regions identified in Figure 57.....	105
Table 31: Composition of regions identified in Figure 59.....	108

List of Figures

Figure 1: Superalloy Evolution in Terms of High-Temperature Capability over a 60 Year Period	6
Figure 2: The Unit Cells of a) γ' -Ni ₃ Al, b) NiAl and c) NiAl ₃	7
Figure 3: Manufacturing techniques commonly employed in the production of gas turbine blades: a) Polycrystalline Cast (PC), b) Directionally Solidified (DS) and c) Single Crystal (SC) [11].....	10
Figure 4: Microstructure of Solution Heat Treated IN-738.....	12
Figure 5: (a) Dendrites with secondary and tertiary arms extending from the primary dendrite, as well as γ/γ' eutectic areas in between. (b) Coarsening γ/γ' morphology approaching the eutectic region in the center.....	13
Figure 6: René N5. (a) BSE image of the γ/γ' microstructure, (b) BSE image of the dendritic microstructure.....	15
Figure 7: Schematic illustration of three common forms of coatings. a) relative coating life and relative temperature enhancement and b) relative coating cost.....	16
Figure 8: Thermal Barrier Coating System [4].....	19
Figure 9: SPS top coats a) Columnar and b) DVC [35].....	21
Figure 10: Oxide scale development resulting from a) cation transport, b) anion transport	24
Figure 11: Oxide scale development resulting when $\Delta G_{Box}^{\circ} > \Delta G_{Mox}^{\circ}$ and NB is sufficiently large such that $\Delta G_{Box} > \Delta G_{Mox}$	25
Figure 12: Monotonically decreasing pO ₂ from the scale/gas interface to the metal/scale interface	26
Figure 13: Oxide scale development resulting when a porous scale is formed	26
Figure 14: BSE image of oxide pegs formed the nickel-base superalloy Mar M200 with a CVD top coat and an aluminide bond coat following 40 cycles at 1100°C [74].....	33
Figure 15: Buehler Ecomet IV Automatic Grinder and Polisher	40
Figure 16: Struers Secotom-10	40

Figure 17: Lindberg (Watertown, WI, USA), Type 51123 Furnace.....	41
Figure 18: CM Inc. (Bloomfield, NJ, USA) 090788-1 High Temperature Furnace	41
Figure 19: Oxy-Gon Industries Inc. (Epsom, NH, USA) C700 Vacuum Furnace.....	42
Figure 20: Scanning Electron Microscopes a) Philips XL30S Schottky-based Field Emission Gun (FEG) SEM, b) VegaII XMU SEM (Tescan, Netherlands).....	42
Figure 21: Bruker AXS D8 Discover diffractometer.....	44
Figure 22: Overall dimensions of samples for a) IN-738, b) CMSX-4, c) René N5	45
Figure 23: Cyclic Furnace Temperature Profile.....	50
Figure 24: As-received IN-738 a) macrostructure, b) and c) BSE and SE images illustrating the compositionally different regions found on the surface	54
Figure 25: γ' microstructure of IN-738.....	56
Figure 26: As-received CMSX-4	57
Figure 27: γ' microstructure of CMSX-4.....	59
Figure 28: As-received René N5.....	60
Figure 29: As-coated DVC sample. a) macrostructure of coating, b) morphology of coating surface, c) round clusters of yttria partially stabilized zirconia, d) segmentation cracks and e) substrate/coating interface	62
Figure 30: As-coated Columbar sample. a) macrostructure of coating, b) morphology of coating surface, c) round clusters of yttria partially stabilized zirconia, d) columnar structure and e) substrate/coating interface	64
Figure 31: IN-738 oxidized at 1150°C for a) 0.5 hrs, b) 1 hr, c) 2 hrs, d) 4 hrs and e) 16 hrs.....	66
Figure 32: IN-738 oxidized at 1150°C for a) 0.5 hrs, b) 1 hr, c) 2 hrs, d) 4 hrs and e) 16 hrs.....	68
Figure 33: Surface of IN-738 oxidized at 1150°C. a) BSE image of sample oxidized for 0.5 hrs b) BSE image of sample oxidized for 1 hr, c) BSE image of sample oxidized for 2 hrs, d) SE image of sample oxidized for 2 hrs, e) BSE image of sample oxidized for 4 hrs f) SE image of sample oxidized for 4 hrs	69
Figure 34: Cross-section of IN-738 oxidized at 1150°C. a) BSE image of sample oxidized for 0.5 hrs b) BSE image of sample oxidized for 1 hr, c) BSE image of sample	

oxidized for 2 hrs, d) BSE image of sample oxidized for 4 hrs e) BSE image of sample oxidized for 16 hrs	72
Figure 35: XRD results for IN-738 isothermally oxidized at 1150°C for 2 hrs	74
Figure 36: CMSX-4 oxidized at 1150°C for a) 0.5 hrs, b) 1 hr, c) 2 hrs, d) 4 hrs and e) 16 hrs.....	75
Figure 37: CMSX-4 oxidized at 1150°C for a) 0.5 hrs, b) 1 hr, c) 2 hrs, d) 4 hrs and e) 16 hrs.....	77
Figure 38: Surface of CMSX-4 oxidized at 1150°C for a) 0.5 hrs b) 1 hr and c) 2 hrs.....	78
Figure 39: Cross-section of CMSX-4 oxidized at 1150°C for a) 0.5 hrs b) 1 hr and c) 2 hrs	79
Figure 40: XRD results for CMSX-4 isothermally oxidized at 1150°C for 2 hrs	81
Figure 41: CMSX-4 layer thickness vs oxidation time	82
Figure 42: Oxidation of CMSX-4 at 1150°C for showing spallation following a) 4 hrs of oxidation and b) 16 hrs of oxidation	82
Figure 43: René N5 oxidized at 1150°C for a) 0.5 hrs, b) 1 hr, c) 2 hrs, d) 4 hrs and e) 16 hrs.....	83
Figure 44: René N5 oxidized at 1150°C for a) 0.5 hrs, b) 1 hr, c) 2 hrs, d) 4 hrs and e) 16 hrs.....	84
Figure 45: Oxidation of René N5 at 1150°C. a) Hf and Ta rich oxides in a eutectic region after 0.5 hrs of oxidation, b) a eutectic region oxidized for 2 hrs and c) a eutectic region oxidized for 2 hrs.....	85
Figure 46: Oxidation of René N5 at 1150°C. a) Hafnium-rich oxide peg after 4 hrs of oxidation and b) Oxidation of the eutectic region after 16 hrs	86
Figure 47: Oxidation of dendritic and interdendritic regions of René N5. a) after 0.5 hrs, b) Nickel, Aluminum, Cobalt and Chromium rich oxides with trace amounts of Tantalum formed after 0.5 hrs, c) Aluminum and Nickel rich oxides formed after 2 hrs, d) morphology after 2 hrs.....	88
Figure 48: Cross-section of René N5 oxidized at 1150°C for a) 0.5 hrs b) 1 hr and c) 2 hrs	90
Figure 49: XRD results for René N5 isothermally oxidized at 1150°C for a) 0.5 hrs, b) 1 hr, c) 2 hrs, d) 4 hrs and e) 16 hrs	93
Figure 50: René N5 layer thickness vs oxidation time	94

Figure 51: Oxidation of René N5 at 1150°C. a) Spallation adjacent to eutectic regions following 4 hrs of oxidation and b) Interface between eutectic and interdendritic region with cracked ridges following 4 hrs of oxidation c) Ridged morphology and gross spallation following 16 hrs of oxidation and d) ridge morphology following 16 hrs of oxidation.....	95
Figure 52: Exposed substrate of DVC coated René N5 sample. a) photograph of sample, b) overall appearance, c) light region, d) grey region	97
Figure 53: Backside of spalled top coat of DVC coated René N5 sample. a) photograph of sample, b) overall appearance, c) cracks, grey and light region and d) light region and oxides surrounding light region	98
Figure 54: DVC coated René N5 following 6 cycles. a) front, b) right c) back and d) left.....	100
Figure 55: DVC coated René N5 sample following 6 cycles. a) general appearance of top coat, b) general appearance of TGO, c) top coat, d) substrate and e) substrate.....	101
Figure 56: Exposed substrate of Columnar coated René N5 sample. a) photograph of sample, b) overall appearance, c) light, grey and dark regions and d) light region and surrounding oxides.....	103
Figure 57: Columnar coated René N5 sample following 10 hrs isothermal heat treatment: a) photograph of backside of spalled top coat, b) backside of spalled top coat, c) exposed substrate following top coat spallation and d) exposed substrate following top coat spallation.....	105
Figure 58: Columnar coated René N5 following 6 cycles. a) front, b) right c) back and d) left.....	106
Figure 59: Columnar coated René N5 sample. a) general appearance of top coat following 4 hrs isothermal heat treatment, b) general appearance of substrate/top coat interface following 6 cycles, c) oxides adhered to top coat following 6 cycles and d) oxides adhered to substrate following 6 cycles	107
Figure 60: Oxidation kinetics of René N5.....	110
Figure 61: CMSX-4 oxidation kinetics	112
Figure 62: Coated René N5 following spallation. a) exposed substrate of DVC coated sample, b) backside of spalled top coat of DVC coated sample, c) exposed substrate of DVC coated sample, d) backside of spalled top coat of DVC coated sample	116

Nomenclature

BSE	Back-scattered electron
CMSX-4	A single crystal Ni-based superalloy manufactured by Canon Muskogan
DVC	Dense Vertically Cracked
DS	Directionally Solidified
EB-PVD	Electron beam physical vapor deposition
EDAX	Energy Dispersive Analysis of X-Rays
IN-738	Inconel 738. A polycrystalline Ni-based superalloy manufactured by Inco Ltd.
LPPS	Low pressure plasma spray
PC	Polycrystalline Cast
RE	Reactive Element
René N5	A directionally solidified Ni-based superalloy manufactured by General Electric
SC	Single Crystal Cast
SE	Secondary electron
SEM	Scanning electron microscope
SPS	Suspension Plasma Spray
TBC	Thermal barrier coating
TGO	Thermally grown oxide
TC	Top Coat
XRD	X-ray diffraction
YSZ	Yttria partially-stabilized zirconia

1 Introduction, Objectives and Scope of Thesis

The gas turbine engine is predominantly used in aircraft applications due to its excellent thrust/weight ratio [1]. However, gas turbine engines are also finding increasing application in the power generation sector as well as in other applications such as offshore platforms predominantly due to their compactness and the wide range of fuels which they can use [1, 2]. Increasing the turbine inlet temperature by 56°C increases the overall efficiency by approximately 1.5% [1, 2]. With new cooling methods and advances in materials, gas turbine thermal efficiencies have improved substantially from approximately 15% in the 1950s to a modern¹ gas turbine efficiency of approximately 45-50% [2]. Nickel-base superalloys achieve the highest temperature/strength combination of all superalloys and as such are utilized in the hot section of the gas turbine engine [3]. By applying a yttria-stabilized zirconia (YSZ) coating metal temperatures can be reduced by 50–150°C [2], allowing further increases in turbine inlet temperature and even greater efficiencies. The YSZ coating is adhered to the nickel-based superalloy using a bond coat. The bond coat also serves another important function: to prevent oxidation of the nickel-based superalloy substrate by developing a “thermally grown oxide” (TGO) [4] composed of either Al₂O₃ or Cr₂O₃ [5]. The application of a bond coat has a direct impact on cost and removal of this step would represent a significant cost reduction in the production of thermal barrier coatings. As such, the purpose of this work is to investigate the

¹ As of 2006

possibility of eliminating the need for this bond coat. This requires that the substrate is able to develop its own stable TGO and to adhere to the YSZ top coat. Several nickel-based superalloys are considered: IN-738, CMSX-4 and René N5. The materials can be evaluated based on the TGO they form when isothermally oxidized. The best candidate is then coated with suspension plasma sprayed (SPS) dense-vertically cracked (DVC) and columnar coatings. Cyclic and isothermal testing is used to evaluate the nickel-based superalloy/YSZ adhesion.

2 Literature Review

Gas turbines emerged in the early 1900s and Frank Whittle was granted the first patent for using a gas turbine to produce a propulsive jet in 1930 [1, 6]. The Whittle engine completed its first flight eleven years later [1]. Due to its excellent thrust/weight ratio, the gas turbine engine continues to be the engine of choice for aircraft applications [1]. However, it has also found increasing application in the power generation and petrochemical industries [2]. The combined cycle power plant, which utilizes the gas turbine engine, is replacing the large steam turbine plants which predominated in North America and Europe until the 1980s [2]. This is due to several factors: the initial costs associated with a steam power plant are approximately 50% more than that of a gas turbine plant [2], a steam power plant from conception to production requires approximately 42-60 months whereas a combined cycle plant requires 22-36 months [2] and the efficiency of the modern steam plant is about 35% versus a combined cycle power plant which has an efficiency of approximately 55% [1, 2]. Furthermore, gas turbines can operate using a wide range of fuels, including natural gas, diesel fuel, naphtha, methane, crude, low-Btu gases, gasified coal, flue gas from steel mills, liquor from paper waste, vaporized fuel oils, and biomass gases [1, 2]. The compactness, efficiency and versatility (in terms of the fuels that can be used) have also led to wide spread use of gas turbine engines in mechanical drive applications; particularly in remote locations, such as offshore platforms [1].

Gas turbine efficiencies have improved substantially from approximately 15% in the 1950s to a modern gas turbine efficiency of approximately 45-50%² [2]. Theoretically, increasing the pressure ratio and/or turbine inlet temperature (the temperature of the hot gases entering the turbine) has a direct impact on efficiency [2]. The limiting factor for most gas turbines has been the turbine inlet temperature [2]. The effect of turbine inlet temperature on overall efficiency is substantial – for every 56°C increase in temperature, the efficiency increases approximately 1.5% [1, 2]. With new cooling methods and advances in materials, turbine inlet temperatures as high as 1427°C and pressure ratios of 40:1 have been achieved [2].

Gas turbine materials must be resistant to various forms of environmental attack including oxidation, corrosion and erosion [4]. Oxidation occurs when the materials react with oxygen, producing oxides [7]. The production of oxides involves the consumption of the base material which degrades the material and reduces component life [8]. Oxidation has long been the primary form of environmental attack on gas turbine materials as it is the primary form of environmental attack seen in most aviation applications [9]. Corrosion did not become a topic of interest until the 1960s when gas turbine engines in military aircraft suffered severe corrosion while operating over sea water during the Vietnam War [2]. Hot corrosion can occur rapidly and is generally associated with alkali metal contaminants, such as sodium and potassium, reacting with sulfur in the fuel to form molten sulfates [2]. The presence of only a

² Thermal efficiency of a gas turbine engine based on data collected from 2006 [2]

few parts per million (ppm) of such contaminants in the fuel, or the equivalent in the air, is sufficient to cause corrosion [2]. In general, corrosion which occurs above the melting point of the salt is called 'type I hot corrosion', while corrosion occurring at lower temperatures is called 'type II hot corrosion' [5]. Erosion results when particulate in the gas stream impacts the blade thereby removing material from the component [10, 11].

2.1 Nickel-Based Superalloys

Superalloys are alloys based on group VIII elements to which a variety of alloying elements are added to produce an alloy which has excellent mechanical properties at high temperatures [3]. There are three kinds of superalloys: nickel-based, cobalt-based and nickel-iron based. Nickel-base superalloys have the highest temperature/strength combination [3]. Nickel-iron-base superalloys, a more economical alternative, are characterized by their high toughness and ductility and are typically only used in their wrought condition [3]. Cobalt-base alloys are primarily used in less structurally demanding, highly corrosive or oxidative environments [3]. The evolution of superalloys in terms of their high-temperature (creep) capability from the 1940's to 2010 is summarized in Figure 1.

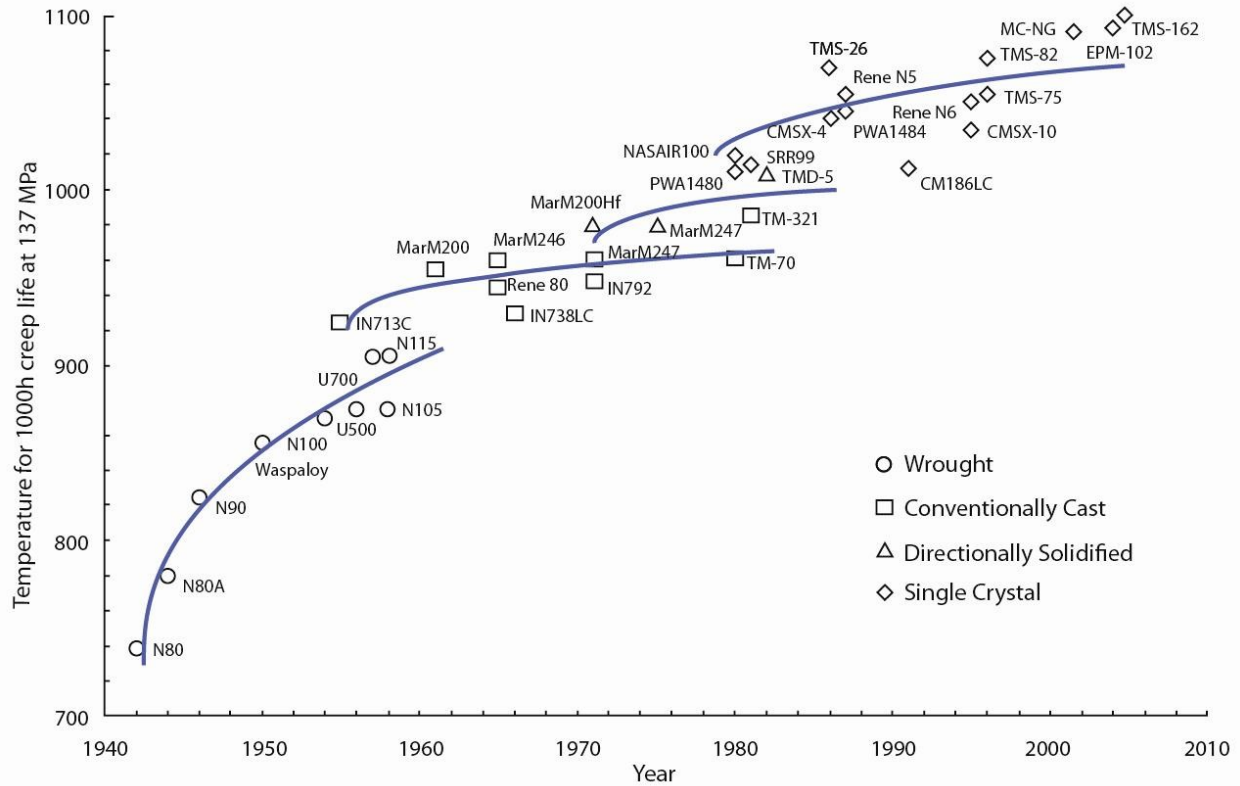


Figure 1: Superalloy Evolution in Terms of High-Temperature Capability over a 60 Year Period [4]

Nickel has a face centered cubic (FCC) crystal structure and is both tough and ductile due to the bonding of the outer d electrons [4]. FCC nickel is stable until it reaches its melting point of 1455°C, making it ideal for high temperature applications [4]. Nickel-base superalloys are based upon Ni, Cr, Al, Ti, Mo and C and have an FCC γ matrix composed of Ni and Al [12]. Both Ni and Al have an FCC crystal structure therefore, complete mutual solid solubility may be anticipated; however, the binary Ni-Al system exhibits a number of solid phases other than FCC [4]. There is a significant degree of directional, covalent bonding which produces precise stoichiometric relationships between Ni and Al within each unit cell [4]. Furthermore, Ni-Al bonds are preferred over Ni-Ni or Al-Al resulting in a strong degree of chemical order [4]. These

phases include: Ni_3Al , NiAl , Ni_2Al_3 , NiAl_3 and Ni_2Al_9 [4]. Unit cells of γ' - Ni_3Al , β - NiAl and NiAl_3 are shown in Figure 2 [13].

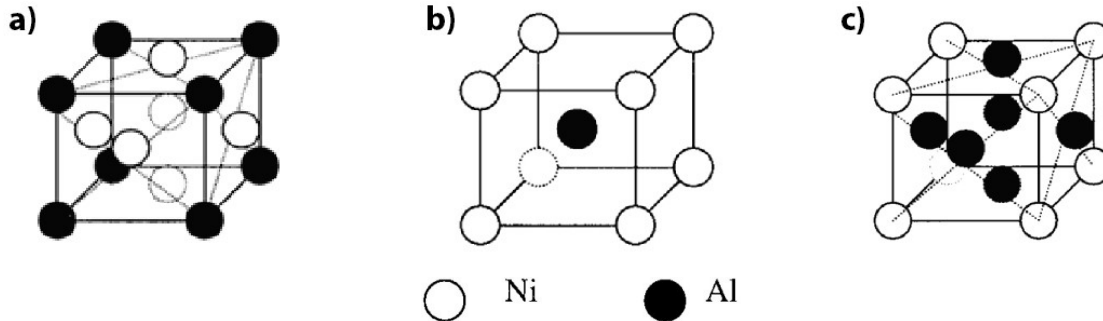


Figure 2: The Unit Cells of a) γ' - Ni_3Al , b) NiAl and c) NiAl_3 [13]

The mechanisms which confer high temperature strength in nickel-based superalloys are quite complex and the γ' - $\text{Ni}_3(\text{Al},\text{Ti})$ phase (Figure 2a) is the most significant in terms of its positive impact on high-temperature superalloy properties [4]. The strength conferred by this precipitate is largely due to the fact that it is often coherent with the γ matrix [4].

Superalloys are compositionally complex; however, in general, there are certain elements which are added to produce a desired effect in a nickel-based superalloy (Table 1).

Table 1: Elements Required Producing a Certain Effect in a Nickel-Based Superalloy [3]

Effect	Element
Solid-solution strengtheners	Co, Cr, Fe, Mo, W, Ta, Re, Al, Ti
Carbide formation:	
MC	W, Ta, Ti, Mo, Nb, Hf
M ₇ C ₃	Cr
M ₂₃ C ₆	Cr, Mo, W
M ₆ C	Mo, W, Nb, Ta
Carbonitride (MCN) precipitation	C, N
γ' Ni ₃ (Al,Ti) precipitation	Al, Ti
Raises solvus temperature of γ'	Co
Hardening precipitates and/or intermetallics	Al, Ti, Nb, Ta
Oxidation resistance	Al, Cr, Y, La, Ce
Improves hot corrosion resistance	La, Th
Sulfidation resistance	Cr, Co, Si
Improves creep properties	B, Ta, Re
Increases rupture strength	B
Grain-boundary refiners	B, C, Zr, Hf
Facilitates working	Fe, B, C
Retards γ' coarsening	Re

The composition of a superalloy impacts the superalloy's microstructure and therefore, influences the superalloy's mechanical properties. However, the macrostructure of the superalloy can be tailored via manufacturing techniques and also has a significant impact on the properties of the superalloy.

Most nozzle and blade castings are made using the conventional investment casting process in which the majority are polycrystalline (PC), but others are directionally solidified (DS) [9]. In the PC casting process, the molten metal is poured into a ceramic mold in a vacuum which prevents the highly reactive elements in the superalloy from reacting with the oxygen and nitrogen in the air [9]. By controlling metal and mold thermal conditions the molten metal solidifies from the surface to the center of the mold, creating a grain structure with approximately round or "equiaxed" grains (Figure 3a) [2]. In polycrystalline superalloys, diffusion and creep deformation favourably occur at grain boundaries, leading to the formation

of voids which produce cracks [3]. Thermal fatigue cracks may initiate at grain boundaries [3]. The damage is often located at the grain boundaries which are perpendicular to the direction of principal stress [3]. To prevent this failure mechanism, one approach has been the reduction and/or complete removal of grain boundaries [3]. This led to the introduction of directionally solidified (DS) castings. By exercising careful control over temperature gradients, a planar solidification front is developed in the blade and the part is solidified by moving this planar front longitudinally through the entire length of the part (Figure 3b) [2]. This produces a blade with a grain structure oriented parallel to the major axis of the part which contains no transverse grain boundaries (Figure 3b) [2]. Better still, is the complete elimination of grain boundaries achieved via single crystal (SC) casting methods. This is achieved by adding a “grain selector” to the base of the wax mould or via the addition of a “seed” at the base of the casting (Figure 3c) [9]. The grain selector or seed promote the growth of a single grain producing a blade composed of a single crystal with no grain boundaries (Figure 3c) [3, 9].

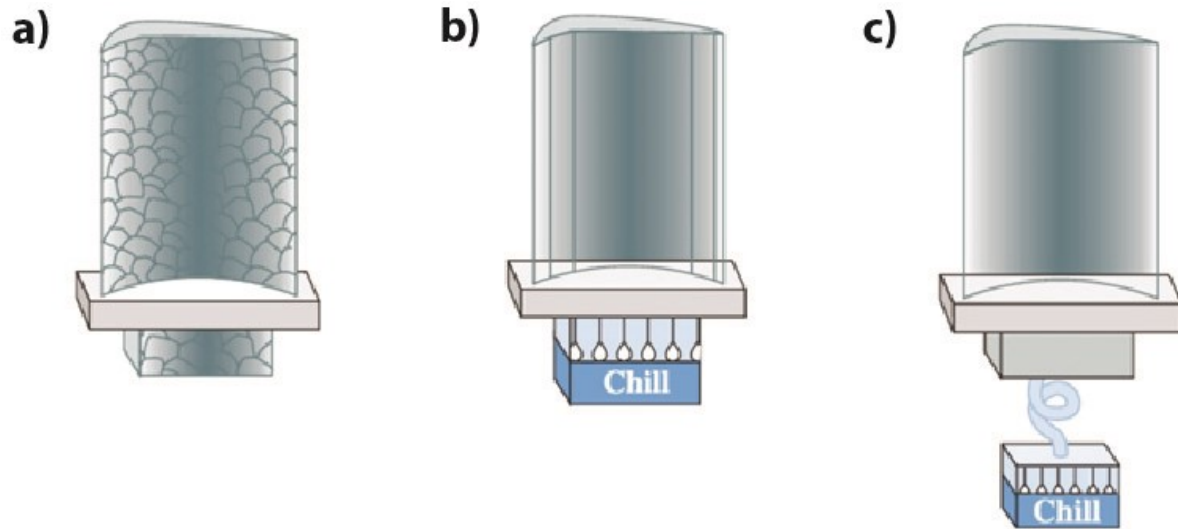


Figure 3: Manufacturing techniques commonly employed in the production of gas turbine blades: a) Polycrystalline Cast (PC), b) Directionally Solidified (DS) and c) Single Crystal (SC) [11]

Any casting (polycrystalline, directionally solidified or single crystal) will exhibit a characteristic dendritic structure. Each dendrite consists of primary arms, secondary arms, tertiary arms and interdendritic regions [14]. The interdendritic regions contain micropores and eutectic phases. Each of these regions (arms, interdendritic regions) has a slightly different composition. This non-equilibrium solidification deteriorates material properties because the local composition deviates from the optimized total composition [14]. In superalloys with a high volume fraction of eutectic ($\gamma + \gamma'$) after casting, the complete dissolution of γ' during heat treatment is very important [14]. As a result, high solutionizing heat treatment temperatures and times are desirable because these are required to dissolve the eutectic phase and achieve chemical homogeneity [14].

2.1.1 IN-738

Although IN-738 emerged in the aerospace industry, it has been primarily adapted for power gas turbines [9]. IN-738 is a vacuum investment cast, polycrystalline, nickel-based superalloy [3, 12, 15, 16]. The nominal composition is provided in Table 2.

Table 2: Composition of IN-738 [4]

	Al	Co	Cr	Mo	Nb	Ni	Ta	Ti	W	Zr
at. % *	7.16	8.2	17.49	1.04	0.55	59.58	0.55	4.04	0.8	0.02
wt. % **	3.4	8.5	16	1.75	0.9	61.54	1.75	3.4	2.6	0.04

* 0.05 at. %B and 0.52 at. %C

** 0.01 wt. %B and 0.11 wt. %C

The microstructure of as-cast IN-738 is dendritic with the formation of secondary solidification microconstituents including MC carbides, M_2SC sulpho-carbides, γ - γ' eutectic, M_3B_2 boride, Ni-Zr and Ni-Ti intermetallic compounds in the interdendritic regions and extensive precipitation of intergranular and intragranular γ' phases [17]. After casting, it is typically solutionized at 1120°C for 2h [18]. This heat treatment results in partial dissolution of the primary γ' precipitates producing a microstructure consisting of cuboidal primary γ' with an average size of $\sim 0.7 \mu m$ and re-precipitated fine secondary γ' precipitates (Figure 4) [17].

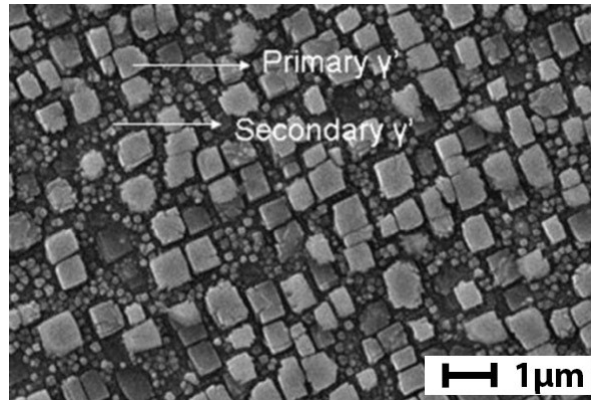


Figure 4: Microstructure of Solution Heat Treated IN-738 [17]

The solutionizing heat treatment is followed by an aging heat treatment at 845°C for 24h [18] to promote the precipitation of a relatively high volume fraction [16] of fine, ordered L12 intermetallic γ' -Ni₃Al and γ' -Ni₃Ti phases [12, 15], which confer additional strength to the alloy.

2.1.2 CMSX-4

CMSX-4 is a second generation single crystal nickel-based superalloy. Elimination of grain boundaries allows for the removal of grain-boundary strengthening elements such as boron and carbon which in turn permits better heat treatments to reduce microsegregation and eutectic content induced by casting while also avoiding melting during heat treatment [4].

Table 3: Composition of CMSX-4 [19]

	Al	Co	Cr	Hf	Mo	Ni	Re	Ta	Ti	W
at. %	12.59	9.26	7.58	0.03	0.38	63.75	0.98	2.18	1.27	1.98
wt. %	5.6	9	6.5	0.09	0.6	61.7	3.01	6.5	1	6

This results in a significant improvement in fatigue life [4]. The second generation single crystal alloys are characterized by the addition of 3 wt. % Re [4]. In particular, the composition of CMSX-4 (the nominal composition is provided in Table 3) is complex and is characterized by

rather high refractory element content (Mo, Ta, W and Re) of greater than 10 wt. % [14]. Additions of Mo, Ta, W and Re provide solid solution strengthening, are characterized by slow diffusion rates and tend to lower diffusion rates of other alloying elements during heat treatment [20]. In the as-cast condition, the superalloy is characterized by a γ matrix, γ' phase precipitates, and $(\gamma + \gamma')$ eutectic regions [20, 21] (Figure 5a). Relatively fine γ' precipitates become coarser near the eutectic regions [21] (Figure 5b).

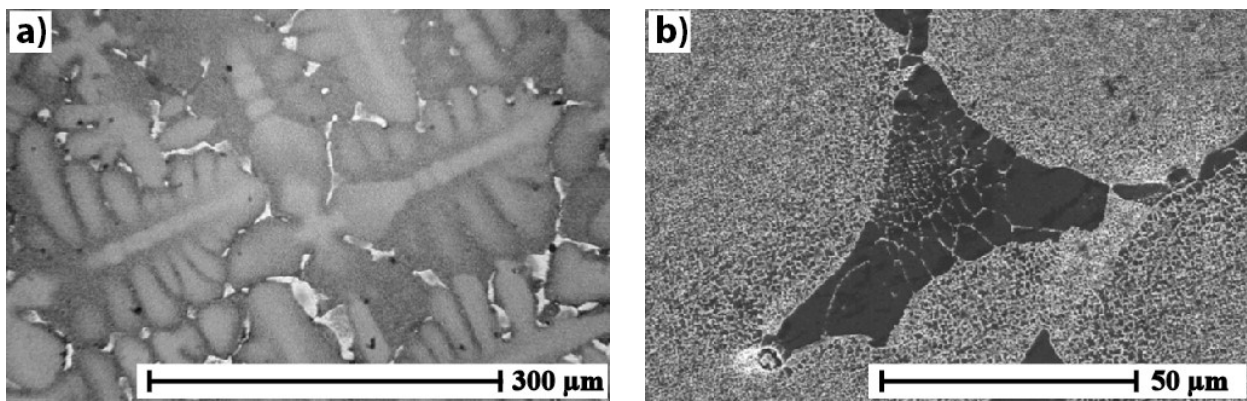


Figure 5: (a) Dendrites with secondary and tertiary arms extending from the primary dendrite, as well as γ/γ' eutectic areas in between. (b) Coarsening γ/γ' morphology approaching the eutectic region in the center [21]

In the as-cast condition; Ta, Al and Ti enrich the interdendritic region [14, 22, 23]. Some authors have suggested that in addition to these elements, Ni also partitions to the interdendritic region [23]. Whether Cr distributes homogeneously [22] or whether it partitions to the dendrite cores [14, 23] is debatable. Co, W and Re segregate strongly to the dendrite core [14, 23]. CMSX-4 is solutionized at temperatures between 1277°C and 1318°C for nearly 24 hours then it is aged for an additional 26 hours [21]. Despite solutionizing heat treatments, CMSX-4 exhibits higher Ta concentrations within interdendritic regions [21, 24]. Ta, Ti and Al are depleted within dendrites and enrich the eutectic phases [21]. Concentrations of Re and W

are lower within the interdendritic regions [21] with eutectic regions being depleted of these elements [21]. Furthermore, there are slightly lower Co concentrations within the dendritic regions [24]. The lower concentration of Re and W within the interdendritic regions results in an inhomogeneity in strength [24].

2.1.3 René N5

René N5 is a nickel-base, second generation, single crystal superalloy. René N5 has a γ/γ' microstructure (Figure 6a) and contains a high volume fraction (>50%) of the γ' phase [25]. The nominal composition of René N5 is provided in Table 4.

Table 4: Composition of René N5 [26]

	Al	Co	Cr	Hf	Mo	Ni	Re	Ta	W
at. %	13.82	7.65	8.09	0.05	0.94	64.69	0.97	2.16	1.64
wt. %	6.2	7.5	7	0.15	1.5	63.14	3	6.5	5.01

In addition to solid solution strengthening via γ' precipitation, solid solution strengthening may be achieved via elemental additions Co, Cr, W, Re and Mo [27]. In particular, Ta strengthens the γ' precipitates by substituting for Al sites in Ni_3Al [27]. René N5 has a dendritic microstructure (Figure 6b). The dendrite cores are enriched with both W and Re and are depleted of Ta and Al [25].

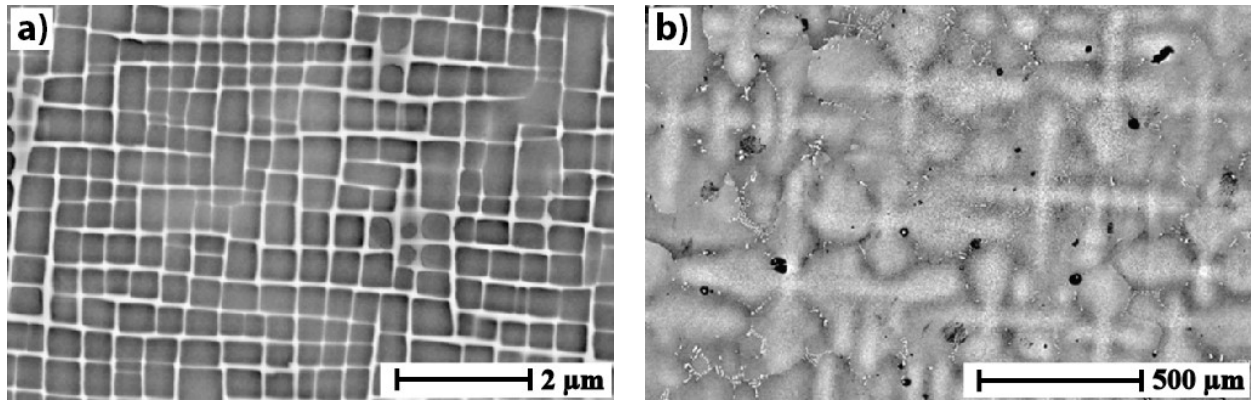


Figure 6: René N5. (a) BSE image of the γ/γ' microstructure, (b) BSE image of the dendritic microstructure [25]

Research conducted on a René N5 alloy with an elemental composition in atomic percent of 8.19% Co, 1.26% Mo, 2.33% Ta, 0.25% C and with all other elements corresponding to the values listed in Table 4; found that 61-63% of the alloy was comprised of the γ' phase [28]. The γ' phase was enriched with Al, Ta and Co [28]. Eutectic γ/γ' comprised 3.6 to 6.0 wt. % [28].

2.2 Coatings

There are three basic types of coatings: diffusion, overlay and thermal barrier. The three general types of coatings are illustrated in Figure 7 in terms of the temperature enhancement conferred and coating life [4].

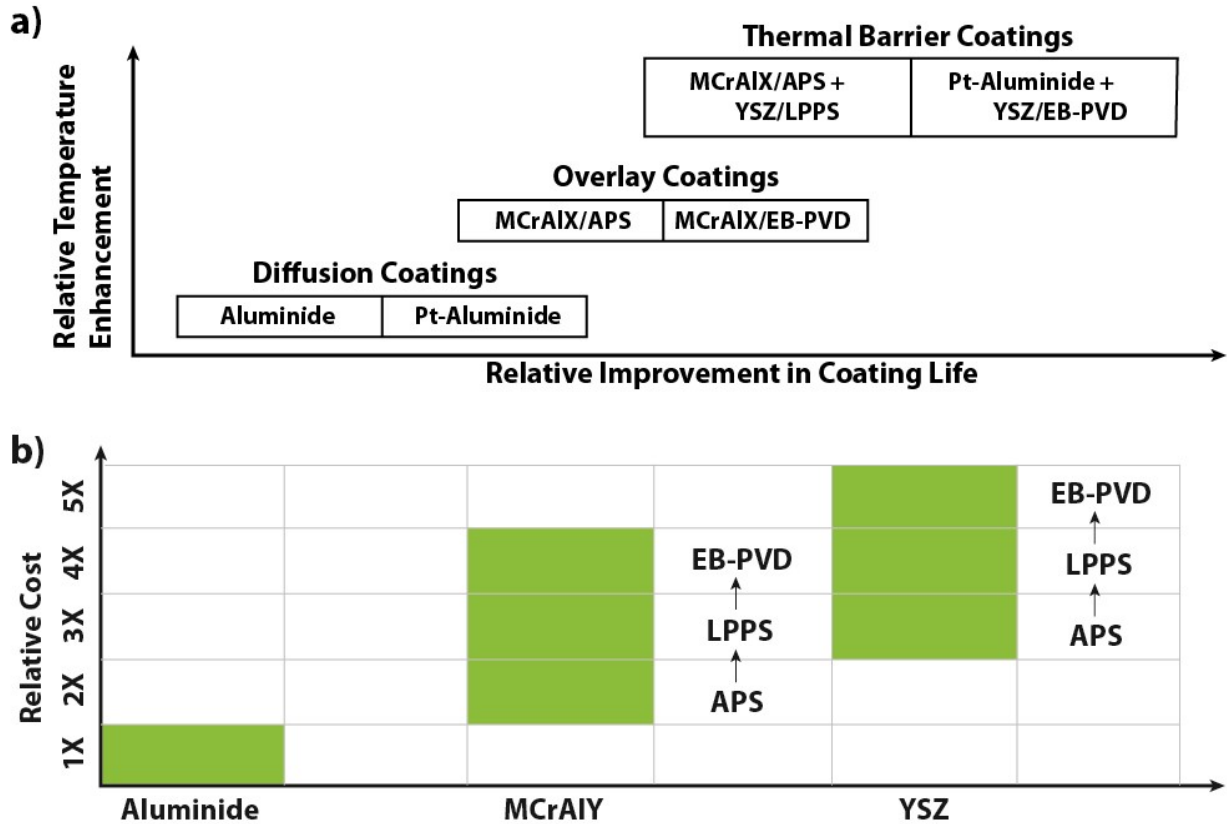


Figure 7: Schematic illustration of three common forms of coatings. a) relative coating life and relative temperature enhancement and b) relative coating cost [4, 9, 29, 30]

Diffusion (Pt-Aluminide) and overlay coatings (MCrAlX, M=Ni, Co or NiCo and X is a reactive element or a combination of reactive elements) are used as bond coats in TBC systems (Figure 7a). Aluminide diffusion coatings are based on the use of the β -NiAl phase whereas overlay coatings are based on a mixture of β -NiAl and γ' -Ni₃Al or γ phases (Figure 2) [31, 32]. The accumulated relative cost for the production of TBCs is quite high given that either an Aluminide or an MCrAlY bond coat must first be applied before the ZrO₂-Y₂O₃ coating is applied (Figure 7b).

2.2.1 Diffusion Coatings

Metallic Cr_2O_3 or Al_2O_3 forming diffusing coatings, which are referred to as the “first generation coatings” are the oldest coating technology and have been in use since the 1960s [4, 31]. These coatings have been extensively used in gas turbine engines for aero-jet propulsion, land-based industrial power generation and in industrial boilers for power generation [5]. Diffusion coatings which promote the growth of Al_2O_3 are referred to as “aluminide” coatings and have more widespread applications than Cr_2O_3 formers [5]. These coatings continue to be the most common form of surface protection [4].

Diffusion coatings are often deposited via “pack diffusion” which is a variant of the chemical vapour deposition (CVD) process [9]. In pack cementation the surface of the component is saturated with aluminum in a powder mixture containing aluminum, aluminum oxide and a halide activator [31]. When heated the aluminum halides diffuse through the powder mixture and encounter the component to be coated, depositing on the surface as well as partly diffusing into it [9]. Platinum-modified aluminide coatings are produced by electroplating a thin layer of Pt onto the surface of the component [4], followed by the aluminum pack cementation process. Often the component is grit blasted prior to deposition to encourage adherence [4]. Thickness required is between 25 and 75 μm and composition is typically 30% Ni/Co with a remainder being aluminum [2]. Generally speaking, in diffusion coatings aluminum is deposited directly on the surface and interdiffused with the substrate so that an aluminum rich $\beta\text{-NiAl}$ layer is produced [4].

2.2.2 Overlay Coatings

The second-generation coatings are referred to as overlay coatings (MCrAlX), the majority of which contain small amounts of yttrium (MCrAlY). The primary advantage of overlay coatings over diffusion coatings is that they can be tailored for specific applications [5]. Typical Cr contents are 16-24 wt. % with Al ranging from 13-18 wt. % [5].

Overlay coatings are manufactured using EB-PVD or plasma spraying. The Electron Beam Physical Vapour Deposition (EB-PVD) method was introduced by Pratt & Whitney in the late 1960s for production of overlay coatings [4]. In general, this technique produces higher-quality coatings at a greater cost than the alternatives [9]. Coating materials are deposited via vapour transport in a vacuum without the need for a chemical reaction [9]. The vapour source can be produced by several methods but electron beam (EB) evaporation is the most commonly used technique [9]. The metal atoms impinge on the preheated part surface and condense into equilibrium or metastable phases [9]. EB-PVD has emerged as the technology of choice for the application of ceramic top coats in TBC systems [4]. However, although EB-PVD is still used in the application of overlay coatings, it is not as common in modern manufacturing practices as plasma spraying has emerged as the manufacturing method of choice for overlay coatings [4].

Plasma sprayed coatings are produced by injecting a pre-alloyed powder into a high temperature plasma gas stream and depositing the metal particles on the component surface [9]. If the process is carried out in atmospheric air it is referred to as Air Plasma Spraying (APS) and if the process is carried out in a low-pressure vacuum chamber the process is called low pressure plasma spraying or LPPS [9].

2.2.3 Thermal Barrier Coatings

The stage 1 turbine blade must withstand the most severe combination of temperature, stress and environment and is generally the limiting component of the gas turbine engine [2]. A stage 1 turbine blade (designed for the most demanding of gas turbine applications) is typically composed of a nickel-base superalloy substrate coated with yttria partially stabilized zirconia, $ZrO_2\text{-}Y_2O_3$ (YSZ). YSZ coatings typically have an insulation layer of 100–300 μm thick and can reduce metal temperatures by 50–150°C [2]. The coating also reduces the impact of thermal fatigue on the blade substrate material by attenuating rapid changes in temperature [9]. Historically YSZ coatings are not applied directly to the substrate material. Instead, a bond coat is applied which enables the coating to adhere [33]. In general, the YSZ top coat and the bond coat form the thermal barrier coating (TBC) system (Figure 8).

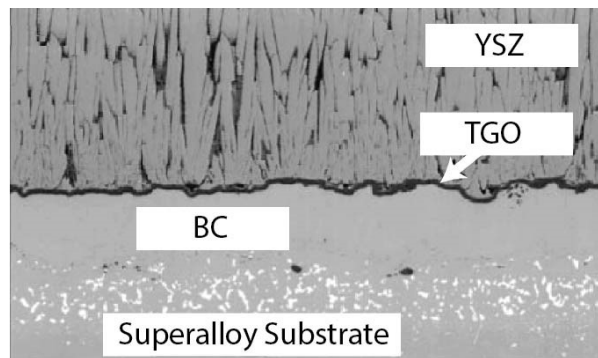


Figure 8: Thermal Barrier Coating System [4]

The top coat is transparent to oxygen [4]. Therefore, to prevent oxidation of the substrate material, the bond coat (either a diffusion or overlay coating) is designed to develop a protective “thermally grown oxide” (TGO) [4] composed of either Al_2O_3 (in its most

thermodynamically stable α phase) or Cr_2O_3 because these oxides form slow-growing, stable and adherent surface scales (Figure 8) [5].

Thermal expansion mismatch between the top coat and the substrate produces large stresses. The approach taken to mitigate the impact of thermal stress is to change the morphology of the top coat. The top coats in thermal barrier coating systems are applied using the same techniques (EB-PVD and plasma spraying) used for the application of overlay coatings. In the APS technique, heat treatments are used to form a network of microcracks [10]. In the EB-PVD technique, a columnar structure is formed [10]. When a stress is applied, the ceramic fragments or columns expand to fill the openings between them, thereby mitigating the stress applied to the bond coat/top coat interface.

Suspension plasma spraying is a relatively new technique used to produce coatings with a variety of microstructures [34]. It is a variant of plasma spraying in which a suspension of fine powder is prepared, enabling powders on a nanometer scale to be applied [34]. Suspension spraying can produce highly porous coatings with columnar or vertically cracked morphology (Figure 9) [34]. SPS is emerging as a more economical alternative for top coat application (in contrast to EB-PVD and LPPS) and can produce microstructures similar to that of EB-PVD or LPPS coatings.

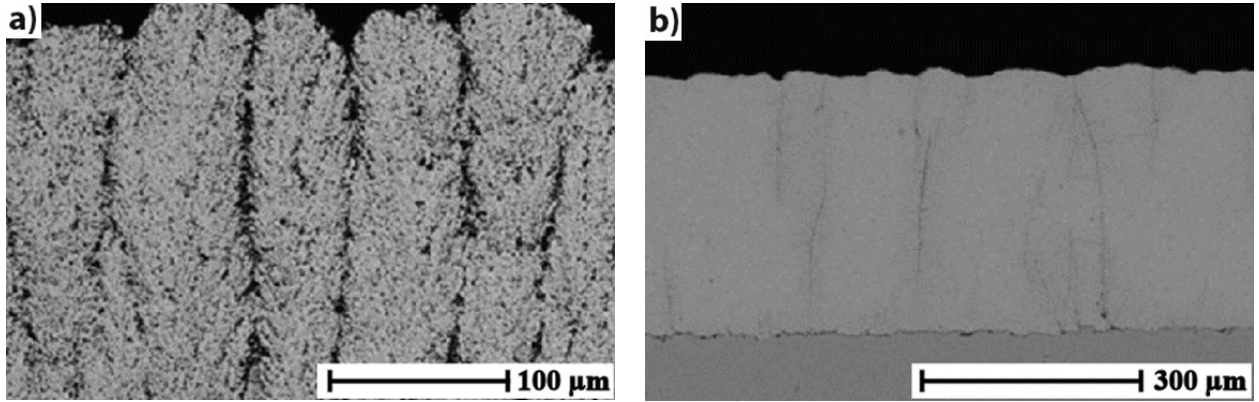


Figure 9: SPS top coats a) Columnar and b) DVC [35]

2.3 Theory

Metallic elements, particularly lightweight elements such as aluminum [36], have inherent resistance to atmospheric oxidation due to the presence of a protective film (in the form of an oxide) that forms immediately upon contact with air [36]. In order for this film to confer any protection, it must be an external, dense, adherent and uniform scale. Thermodynamics, oxidation mechanisms, oxidation kinetics, principles of adhesion and an understanding of growth stress provide the insight necessary to understand this scales development and ultimately to be able to evaluate its effectiveness as a TGO.

2.3.1 Thermodynamics

The Gibbs free energy (G) of a reaction is a measure of the thermodynamic driving force for that reaction. An isothermal, isobaric system is at equilibrium when the change in free energy ($\Delta\bar{G}$) is zero [7]:

$$\Delta\bar{G} = \bar{G}_P - \bar{G}_R = 0 \quad 1$$

Where $\Delta\bar{G}$ is the change in free energy of the system in kJ/mol. The change in free energy is equal to the difference in free energy of the products ($\Delta\bar{G}_P$) and the reactants ($\Delta\bar{G}_R$).

The change in the free energy of the reactants may be expressed as [7]:

$$\bar{G}_R = \sum_{i=1}^m \bar{G}_i n_i \quad 2$$

Where \bar{G}_i is the change in free energy of component i , n_i is the number of mols of component i and m is the total number of components in the reactants. By analogy, Equation 2

may be used to determine the free energy change of the products. Utilizing the ideal gas assumption, the change in free energy of component i can be expressed as follows [7]:

$$\bar{G}_i = \bar{G}_i^\circ + \bar{R}T \ln(k_i) \quad 3$$

Where \bar{G}_i (kJ/mol) is the change in free energy of component i relative to the standard reference temperature and pressure. Values of \bar{G}_i° for oxides of elements considered in this study can be found in Table A-1. All experiments conducted in this study were performed at 1150°C (~1425K) and atmospheric pressure (1 atm). As such, all values of \bar{G}_i° provided in Table A-1 are evaluated at 1 atm and 1425K relative to a reference state of 1 atm and 298.15K. \bar{R} (kJ/K·mol) is the ideal gas constant and T (K) is the temperature of the system. k_i is the equilibrium constant of species i . For an ideal gas [7]:

$$k_i = \left(\frac{p_i}{p_i^\circ} \right) = \frac{n_i}{V_i} = N_i \quad 4$$

p_i is the partial pressure of component i . If component i is a solid (or is approximated as a solid as may be the case for oxides) then $p_i = 1$. p_i° is the partial pressure of component i at the reference pressure (defined as 1 atm). V_i is the volume occupied by component i and N_i is the molarity of component i (mol/L). Equation 4 relates the concentration of species i to the free energy. Essentially, whether reaction will occur is depends on: 1) the standard free energy of the product at the system temperature and 2) the concentration of the reactants at the reaction interface.

2.3.2 Oxidation Mechanisms

Since all metals are ionic in nature, ions and electrons must migrate in order for an oxidation-reduction reaction to proceed [37]. In a pure metal, M, cation migration refers to the movement of metal cations (M^{a+}) and anion migration refers to the movement of oxygen anions (O^{2-}); where a represents the oxidation state of M.

When the metal does not exhibit oxygen solubility, the reaction begins at the metal/gas interface and the products of this reaction form a scale of an oxide of M (MO) between the alloy and the gas [37]. For the reaction to continue either anions (O^{2-}) or cations (M^{a+}) must penetrate the scale [9, 37]. If the cation rate of diffusion through the scale is greater than the rate of anion diffusion than the scale will continue to grow at the scale/gas interface (Figure 10a) [37]. If the rate of anion diffusion is greater than the rate of cation diffusion than the scale will continue to grow at the metal/scale interface (Figure 10b) [37].

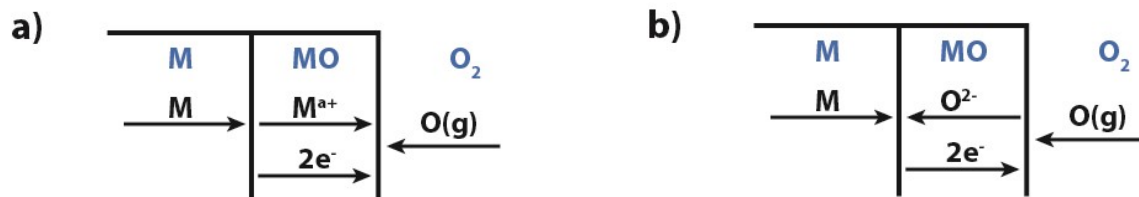


Figure 10: Oxide scale development resulting from a) cation transport, b) anion transport [37]

In an alloy composed of base metal M and alloying element B in which $\Delta\bar{G}_{B_{ox}}^{\circ} > \Delta\bar{G}_{M_{ox}}^{\circ}$, than oxides of B may form at any interface in which N_B is sufficiently large such that $\Delta\bar{G}_{B_{ox}}^{\circ} > \Delta\bar{G}_{M_{ox}}^{\circ}$ [8, 37]. This may occur after M oxidizes for some time and the concentration of M at the surface decreases, thereby increasing N_B [8, 37].

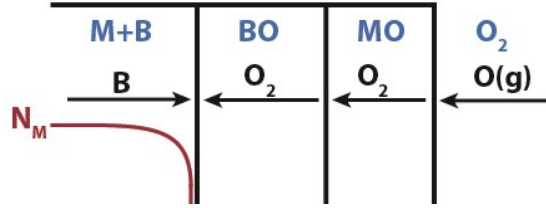


Figure 11: Oxide scale development resulting when $\Delta\bar{G}_{B_{ox}}^{\circ} > \Delta\bar{G}_{M_{ox}}^{\circ}$ and N_B is sufficiently large such that $\Delta\bar{G}_{B_{ox}} > \Delta\bar{G}_{M_{ox}}$ [37]

Another scenario results when the concentration of oxygen at the reaction interface N_O is sufficiently small such that $\Delta\bar{G}_{M_{ox}}$ is positive (a positive value of $\Delta\bar{G}_{M_{ox}}$ indicates that the reaction will not occur) [7, 8, 37]. N_O may be small at the scale/gas interface in a low oxygen environment (low partial pressure of oxygen, p_{O_2}) such as a vacuum furnace [8, 37]. In this case, preferential oxidation of B may occur as long as $\Delta\bar{G}_{B_{ox}}$ is negative and $\Delta\bar{G}_{M_{ox}}$ is positive [8, 37].

Each oxide layer creates a barrier for O^{2-} anion transfer, with some oxides forming more effective barriers than others [8]. Therefore, N_O (more appropriately referred to as p_{O_2} since oxygen is in a gaseous state [7]) decreases monotonically from the scale/gas interface to the metal/scale interface with each successive oxide layer [8]. This promotes the preferential oxidation of elements with relatively higher standard free energy changes at interfaces closer to the metal/scale interface [8].

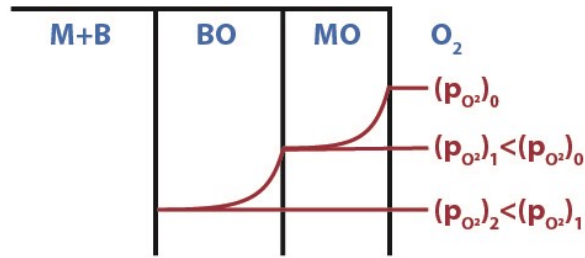


Figure 12: Monotonically decreasing p_{O_2} from the scale/gas interface to the metal/scale interface [37]

Another scenario results when the oxide scale does not form a coherent layer [37, 38]. In this case, N_{O_2} will be quite high as oxygen anions diffuse through pores or cracks within the oxide layer(s) [37, 38]. As a result, diffusion within the oxide layer is irrelevant, since oxygen reaches the metal/scale interface more rapidly than diffusion through the oxide layer takes place [37]. The oxide is built up from the bottom and eventually spalled from the surface [37].

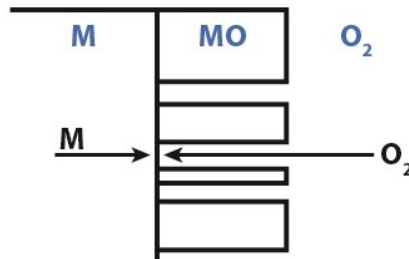


Figure 13: Oxide scale development resulting when a porous scale is formed [37]

2.3.3 Oxidation Kinetics

The time dependent growth of an oxide scale can be expressed as [8]:

$$\frac{d\xi}{dt} = f(t) \quad 5$$

In which the general solution is [39]:

$$\xi^n = kt \quad 6$$

Where ξ is the mass gain or change in height of the oxide scale, t is the oxidation time and k is the growth constant. The growth exponent, n , provides information as to the mechanism under which oxide growth occurs since the overall rate of reaction is dictated by the slowest reaction [8]. If the growth of the scale is dictated by diffusion of an element within the scale itself than $n=2$ [8].

When oxygen diffusion is rapid as is the case when the oxide layer is not coherent or in the earlier stages of oxidation when the oxide layer is quite thin and the flux of species through the layer is high, $n=1$ [38]. In this case, the analytical solution is easily derived from Equation 5 assuming $f \neq f(t)$ [8]. Quadakkers et al. illustrated that the oxidation kinetics of $\alpha\text{-Al}_2\text{O}_3$ may be described by Equation 6 but with a growth exponent of 3, given that the primary mechanism of diffusion through an $\alpha\text{-Al}_2\text{O}_3$ scale is via oxide grain boundaries [40].

2.3.4 Adhesion

The strength of an adhesively bonded joint is limited by the weakest of the interfaces within the bond [41]. A TBC system is in fact composed of metal and ceramic interfaces. The work required to break the adhesive bond, called the “work of separation” and denoted “ W ” (J/m^2), can be presented in terms of the Dupré relation [42, 43]:

$$W = \gamma^A + \gamma^B - \gamma^{AB} \quad 7$$

Where γ^A, γ^B and γ^{AB} are the surface energy of surface A, B and the interface, respectively; and are measured in units of energy per unit area (J/m^2) [42]. Strong adhesive bonds correspond to a large work of separation [42].

Adhesion may be improved by increasing the interfacial contact area, thereby maximizing W (J/m^2). In this case, the interlocking of voids, such as pores and holes improves the strength of the adhesive joint [41]. Interfacial contact area will be maximized by the growth of a dense and uniform TGO. A non-uniform or porous TGO will not make consistent contact with the top coat or substrate resulting in reduction in the work of separation. Interfacial contact area may be reduced by the formation of voids. Voids may be created by the Kirkendall effect [31, 44, 45], sulphur, or by TGO growth. Adhesion may also be improved by selecting materials which may optimize the cohesive forces (i.e., decrease γ^{AB} , increase γ^A and γ^B). Christensen et al. conducted a comprehensive review of atomistic modelling studies done prior to 2001 and concluded that rare earth or transition metals with open d- or f- shells show the greatest adhesion to ceramics [42]. Table A-2 contains a list of all rare earth and transition metals and indicates how many electron vacancies there are for each shell (3, 4 or 5) for each d- or f- subshell.

2.3.5 Growth Stress

Scale “rumpling” and “ratcheting” also contribute to oxide/alloy debonding and are related to thermal and growth stresses generated within the TBC system [45]. Rumpling is characterized by an upward displacement of the bond coat into the top coat; whereas ratcheting involves only downward penetration of the TGO into the bond coat [46]. In both cases, stresses developed within the TGO are relaxed by pushing material either up or down [46].

Compressive stresses developed within the α -Al₂O₃ phase due to growth and thermal stress can be on the order of several GPa in which growth stresses are considered to be the larger contributor to the overall stress [4]. To relieve the compressive stress, tensile stresses are generated parallel to the TGO/top coat interface. This leads to the development of horizontal micro-cracks, which eventually result in spallation of the top coat [33, 47]. Oxidation behavior of the TGO is inherently related to spallation of the top coat and therefore failure of the system [4].

Growth stress is often the primary contributing factor to oxide/alloy debonding and hence, TBC system failure [48]. The mechanisms of growth stress are quite complex and not fully understood; however, it is believed that growth stress is strongly affected by the volumes of the metal and oxide, the crystal structures of the oxide and metal, and the growth mechanism of the oxide [13]. The volume change due to the formation of an oxide at the oxide/metal interface can be quantified using the Pilling-Bedworth ratio (PBR) [49, 50, 51]:

$$PBR = \frac{M_O \rho_M}{n M_M \rho_O} \quad 8$$

Where M and ρ are the molecular mass and density, respectively. Subscripts O and M denote oxide and metal, respectively. n is the number of atoms of metal per one molecule of oxide. In general, when the PBR > 1 a compressive stress develops in the oxide scale and when the PBR < 1 a tensile stress is generated [13, 50, 51]. The farther from 1, the greater the stress is anticipated to be [13, 50, 51]. However, the PBR is only a rough quantification of growth stress and cannot be directly correlated to any actual stress values [8, 13]. In general, a PBR between 1 and 2 is considered to form a protective surface scale [51]. A PBR greater than 2

produces a non-protective scale prone to spallation [51]. A PBR of less than 1 forms a scale that does not provide sufficient coverage to be protective [51].

2.4 High Temperature Oxidation of Nickel-Based Superalloys

As additional elements are added, the oxidation process becomes increasingly complex. Heat treatment (either isothermal or cyclic) of Ni-based alloys (Ni, Al, Cr as well as other alloying elements) with or without bond coat and/or top-coat, in the transient period (within the first 24 hrs of oxidation) at high temperatures (between 930°C to 1200°C) generally exhibit a layer of Al_2O_3 at the alloy/oxide interface [47, 52, 53, 54, 55, 56, 57]. In some cases, Al_2O_3 formation is localized with regions of Cr_2O_3 , NiO, $\text{Ni}(\text{Al,Cr})_2\text{O}_4$ [52, 58, 59, 60, 61]. Generally, the layer adjacent to the scale/gas interface will contain one of the following or a mixture of any of the following: Al_2O_3 , Cr_2O_3 , NiCr_2O_4 , NiAl_2O_4 and NiO [47, 52, 53, 56, 62].

It is well-established that for an alloy to have good oxidation resistance an element such as aluminum in the alloy must be selectively oxidized to form a continuous external scale which is resistant to cracking and spalling [63]. Furthermore, in the event that the oxide spalls, it is essential that the selectively formed oxide be formed again to heal the spalled region [63].

2.4.1 $\alpha\text{-Al}_2\text{O}_3$

To prevent oxidation of the substrate material, the bond coat (either a diffusion or overlay coating) is designed to develop a protective “thermally grown oxide” (TGO) [4] composed of either Al_2O_3 (in its most thermodynamically stable α phase) or Cr_2O_3 because these oxides form slow-growing, stable and adherent surface scales [5].

Al_2O_3 in its α phase has a dense HCP crystal structure with few defects and passes through no phase transformations between room temperature and its melting point [64]. There are several polymorphs of Al_2O_3 . The $\alpha\text{-Al}_2\text{O}_3$ phase is the most thermodynamically stable and therefore all other phases of Al_2O_3 will tend to transform to $\alpha\text{-Al}_2\text{O}_3$ with transformation beginning at the oxide/metal interface [4]. For this reason, these metastable phases are often referred to as “transient” phases. Enhanced oxidation kinetics ($n < 3$) are often observed during the transient period of oxidation when less dense transient alumina polymorphs (e.g. δ , γ and θ) are developing before later transforming into stable $\alpha\text{-Al}_2\text{O}_3$ [65, 55, 66]. Transformation from θ to α has been reported to result in a change in topography from whiskers to a network of ridges for both Ni-Al and (Ni,Pt)-Al systems due to growth stresses generated when $\theta\text{-Al}_2\text{O}_3$ transforms to $\alpha\text{-Al}_2\text{O}_3$ [4, 67]. The transformation is accompanied by a change in volume: the PBR value for $\theta\text{-Al}_2\text{O}_3$ on NiAl is 1.95 and is 1.78 for $\alpha\text{-Al}_2\text{O}_3$ [55]. This growth stress produces microcracks along the ridges. As oxidation proceeds, the microcracks act as short-circuit paths for outward diffusion of Al^{3+} , resulting in an increased growth of the ridges [4, 67, 68].

2.4.2 Spinel

Spinel, in the context of superalloys, generally refers to oxides of composition $\text{Ni}(\text{Al},\text{Cr})_2\text{O}_4$ or $\text{Co}(\text{Al},\text{Cr})_2\text{O}_4$. In the context of nickel-base superalloys specifically spinel refers to $\text{Ni}(\text{Al}, \text{Cr})_2\text{O}_4$. Spinel is often reported in literature [47, 52, 53, 56, 58, 59, 60, 61, 62, 69] as it is generally associated with unwanted volume expansion [65]. It is particularly deleterious due to its specific volume mismatch and rapid growth rate [61, 68, 70]. Spinel is known to manifest

during the transient period of oxidation [65]. The thicker and more continuous the spinel layer is, the greater the deleterious impact on TGO performance [65]. Spinel is most susceptible to grow on top of Ni/Co/Cr-rich alloy phases (notably γ) [65].

2.4.3 Reactive Elements

A number of elements may be considered reactive elements (REs). However, the most effective reactive elements are yttrium, lanthanum and cerium [3]. It is now well established that these elements can be used to substantially improve oxide scale adherence [63]. Multiple RE additions may have a synergistic effect [3, 4]. Generally, RE additions improve the oxidation lifetime by a factor of 10 [3]. Yttrium is present in MCrAlY coatings to improve the adherence of Al_2O_3 scales to these coatings [63].

Sulphur segregates to the cavities formed at the oxide/alloy interface during oxidation and stabilizes them preventing any further oxide development which may have otherwise filled the cavities [71]. Reactive elements have been found to prevent the formation of vacancies at the interface by eliminating dissociated sulphur [5]. Although reactive elements may improve scale adhesion by limiting the amount of dissociated sulphur, sulphur has been found to diminish scale adhesion even in the absence of voids [71]. An atomistic modelling method known as Tight Binding was used by Hong et al. [72] in a study focused on the interface of the Ni/ Al_2O_3 system and found that sulphur impurities significantly decrease the interface strength, due to S^{2-} , O^{2-} closed-shell repulsions increasing the distance of the Al^{3+} cation from the Ni surface layer. Anderson et al. [73] calculated the adherence of Al_2O_3 on Ni-Al with and without

Y using the Tight-Binding method and attributed the mixing of the unoccupied d shells with the O-2p orbitals to be responsible for the increased adhesion seen in these systems.

“Dynamic segregation theory” has been established to explain the benefits of the “reactive element effect” on TGO uniformity. Reactive elements have a strong affinity for oxygen and therefore, a tendency to segregate towards grain boundaries of α -Al₂O₃ and form rare earth oxides [4, 31]. This impedes the outward diffusion of the Al³⁺ cation resulting in a more uniform Al diffusion rate throughout the alloy and a more uniform oxide scale [4, 31].

Reactive elements may also improve scale adhesion by “pegging” the alumina scale to the underlying metal [5, 33]. Pegs are RE oxides which form by internally oxidizing the substrate, thereby mechanically keying the oxide scale to the alloy surface [3]. Oxide pegs formed on an aluminide bond coat on substrate material Mar M200 are shown in Figure 14.

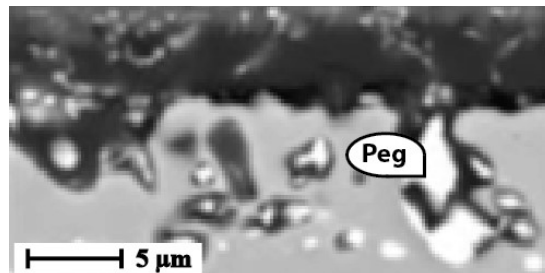


Figure 14: BSE image of oxide pegs formed the nickel-base superalloy Mar M200 with a CVD top coat and an aluminide bond coat following 40 cycles at 1100°C [74]

Experimental results have shown that pegs are composed of a reactive element rich oxide core and an outer alumina sheath [45].

2.4.4 Other Elements

Hafnium is considered by some authors to be a RE as it has many properties of a RE [3]. However, hafnium is not considered to be as effective as a RE as Ce, La or Y [3]. McVay et al. performed isothermal oxidation studies on single crystal nickel-base superalloys and found that Hf and Y improve oxidation resistance but the effects of Yttrium are substantially greater than Hafnium [63]. Hafnium has a high affinity for sulfur and acts as a getter [3]. In the CMSX series of alloys, CMSX-2 was modified with 0.1 at. %Hf and commercialized as CMSX-3 to improve alumina coating adherence [3].

At temperatures above approximately 800°C and at an oxygen partial pressure of 0.53 atm pure Ta rapidly oxidizes ($n \sim 2$) and subsequently spalls, producing overall near-linear growth kinetics ($n \sim 1$) [75]. The principal reaction product is Ta_2O_5 which initially forms an adherent scale but eventually detaches [75]. A metastable sub-oxide, TaO_2 (which eventually transforms to Ta_2O_5) forms at the Ta_2O_5 /Ta interface [75]. Pawel and Campbell found that large growth stresses are produced by oxides of Nb and Ta in the Nb and Ta pure metal systems, respectively [76]. The stresses were concluded to be responsible for the high porosity of the pentoxides of Nb and Ta [76].

Several authors have shown that titanium has a detrimental effect on oxidation performance. Nagai and Okabayashi [77] performed oxidation testing at 1 atm on an Ni-20Cr alloy at temperatures between 1273 and 1473K. They found that Ti content was directly proportional to the degree of spallation [77]. The Ti in the scale was proposed to lead to the creation of voids which decreased interfacial contact area and increased oxygen activity which

lead to enhanced growth kinetics [77]. Yang [78] conducted high temperature oxidation studies on an alloy containing Ni-4.2Co-4.8Cr-12.8Al-1.6W-3.1Mo-1.0Re (at. %) with varying additions of 1-3 at. %Ti and 1-3 at. %Ta at temperatures between 1000°C and 1100°C in atmosphere. It was found that a concentration of 1at. %Ta improved oxidation resistance, while 1 at. %Ti had no effect [78]. However, concentrations of 3 at. %Ti or 3 at. %Ta degraded oxidation resistance and the degradation was particularly severe for Ta [78]. It was proposed that at higher concentrations, these elements form complex, less protective oxides [78]. Cade et al. found that additions of Ti had a detrimental impact on the oxidation of directionally solidified nickel-based superalloy, Rene 80 [79].

2.4.5 IN-738

In work done by Zhu et al. [80], IN-738 samples were isothermally oxidized at 1073°C for 4, 8 and 11 hrs. After 4 hours, Cr₂O₃, TiO₂, Al₂O₃ and Ni₃TiO₅ were reported. As oxidation time increased, Cr₂O₃ and Ni₃TiO₅ became more prevalent; whereas Al₂O₃ and TiO₂ maximized at 4 hours. Enlarged particles identified as rutile TiO₂ were identified after 4 hours. As oxidation continued, some of the TiO₂ was converted to Ni₃TiO₅ and was eventually covered by a layer of faster growing Cr₂O₃ oxide. Cr₂O₃ was reported to have a faster growth rate than either Al₂O₃ or TiO₂.

Cade et al. [79] conducted studies on IN-738 oxidized at 1 atm and 900°C. Growth kinetics were determined by weighing samples after removing them from a furnace and were determined to be parabolic (n=2) with a correlation coefficient of 0.9376. The scale was found

to be composed of a dense outer scale of Cr_2O_3 mixed with Ni and Ti oxides. A discontinuous internally oxidized subscale of Al_2O_3 was also present.

2.4.6 CMSX-4

CMSX-4 heat treated isothermally at 1100°C for durations ranging from 5 to 10 hrs has been found to develop a uniform Al_2O_3 layer. This layer is covered locally with (starting with the layer adjacent to the Al_2O_3 layer and ending with the oxide layer situated at the scale/gas interface): a layer of mixed Cr and Ta oxides, a layer of Ti oxides and a layer of Ni oxides. These oxides were suggested to be CrTaO_4 , TiO and NiO [81]. The overall oxide scale thickness was found to be 2-5 μm thick [81]. The substrate adjacent to the oxide is depleted of the γ' phase. The γ' as well as the $(\gamma + \gamma')$ eutectic phases beneath the γ' free region are coarser [81]. Some small pores and voids form along various layers within the oxide and along the surface [81].

2.4.7 René N5

A dense, slow-growing and well-adherent alumina scale has been reported to develop on René N5 following high temperature ($\sim 1000^\circ\text{C}$) oxidation [82, 83, 84]. A summary of the oxides formed on René N5 for different heat treatment temperatures and times are outlined in Table 5, where numbered items indicate the sequence of oxides (1=adjacent to substrate).

Table 5: Oxide structure of René N5

Temp (°C)	Time (hours)	Oxides	Ref
980	26	1. Al ₂ O ₃ 2. NiO, CoO 3. NiAl ₂ O ₄ , NiTa ₂ O ₆ and Cr ₂ O ₃	[83]
1000	100	1. Al ₂ O ₃ w/Ta, Ni and O 2. NiO w/ Ni, Al, O, Ta and Cr	[83]
980	10	1. Al ₂ O ₃ 2. Interlayer high in Re (~ 5 at. %) 3. Top layer containing NiO	[83]
980	50	1. α-Al ₂ O ₃ 2. α-Al ₂ O ₃ , Cr ₂ O ₃ , NiTa ₂ O ₆ , TaO ₂ , NiCr ₂ O ₄ , NiAl ₂ O ₄ , CoTa ₂ O ₆ 3. NiO w/ small amounts of Co ₃ O ₄	[82]

In kinetic studies, increased mass loss has been noted at 980°C in comparison to 1000°C suggesting that a protective α-Al₂O₃ layer forms earlier at 1000°C than at 980°C [83]. In the samples oxidized for 26 hrs at 980°C it was noted that both the NiO/CoO layer and the layer containing NiAl₂O₄, NiTa₂O₆ and Cr₂O₃ were porous [83].

2.5 TBC system with no Bond Coat

The gas turbine engine continues to be the engine of choice for aircraft applications and is increasing in popularity in other sectors as well [1, 2]. To increase efficiency, the turbine inlet temperature must be increased [2]. Currently, this is limited by the capability of the materials used [2]. Nickel-base superalloys achieve the highest temperature/strength combination [3] and as such are used in the highest temperature applications of the gas turbine engine. YSZ coatings may reduce metal temperatures by an additional 50–150°C [2]; allowing further increases in turbine inlet temperature and even greater efficiencies. Unfortunately, these coatings are transparent to oxygen and do not provide protection from oxidation [4]; a form of environmental degradation which results in the consumption of the base metal [8]. This increases the cost to produce TBCs since either a diffusion or overlay coating must be applied

prior to YSZ application (Figure 7b) [4, 9, 29, 30]. Generally speaking, diffusion and overlay coatings work by producing a layer of $\alpha\text{-Al}_2\text{O}_3$ which acts as a cation diffusion barrier; preventing the loss of substrate material [4, 5]. The YSZ adheres well to this layer and adhesion is improved with the addition of REs [63]. However, $\alpha\text{-Al}_2\text{O}_3$ scales are known to develop on oxidized nickel-based superalloy substrate materials as well; such as IN-738, CMSX-4 and René N5 [79, 80, 81, 82, 83, 84]. Theoretically, if an $\alpha\text{-Al}_2\text{O}_3$ scale were formed directly on a nickel-based superalloy than a YSZ should be able to adhere directly to the substrate material itself.

In work done by Wu et al. [85] Pt was electroplated on to single crystal alloys SRR99, CMSX-4, TMS-82+, PWA-1484 and TMS-138A. No diffusion or overlay bond coats were applied. EB-PVD YSZs were then directly applied to the substrate. These samples performed better in cyclic testing than samples of the same substrate material with Pt-Al bond coats. It was also found that coating life was strongly dependent upon substrate composition. This work proves that the interfacial adhesive strength of TBCs is correlated to the composition of the substrate material and that a bond coat may not always be required.

3 Equipment, Sample Preparation and Experimental Procedures

The equipment used for sample preparation, conducting experiments and performing analysis as well as the procedures used to prepare samples for testing and for analysis are described in this section.

3.1 Equipment

The equipment used for sample preparation, conducting experiments and for analysis is described in the following sections.

3.1.1 Buehler Automatic Grinder/Polisher

The sample surfaces were prepared using a Buehler Ecomet[®] IV automatic grinding/polishing machine with a Buehler Euromet[™] I Power Head (Figure 15).



Figure 15: Buehler Ecomet IV Automatic Grinder and Polisher

3.1.2 Struers Secotom-10

All samples were cut using a Struers Secotom-10 (Figure 16) equipped with a Struers M1D20 Diamond Cut-off Wheel with a rotational speed of 1000 RPM and a feed speed of 0.0015mm/s.



Figure 16: Struers Secotom-10

3.1.3 Atmospheric Furnace

All isothermal high temperature testing was conducted using a Lindberg (Watertown WI, USA) furnace Figure 17.



Figure 17: Lindberg (Watertown, WI, USA), Type 51123 Furnace

3.1.4 Cyclic Furnace

All cyclic high temperature testing was conducted using a CM Inc. (Bloomfield, NJ, USA) 090788-1 High Temperature Furnace (Figure 18).



Figure 18: CM Inc. (Bloomfield, NJ, USA) 090788-1 High Temperature Furnace

3.1.5 Vacuum Furnace

Diffusion heat treatments were conducted to encourage top coat/substrate adherence using an Oxy-Gon Industries Inc. (Epsom, NH, USA) C700 Vacuum Furnace (Figure 19).

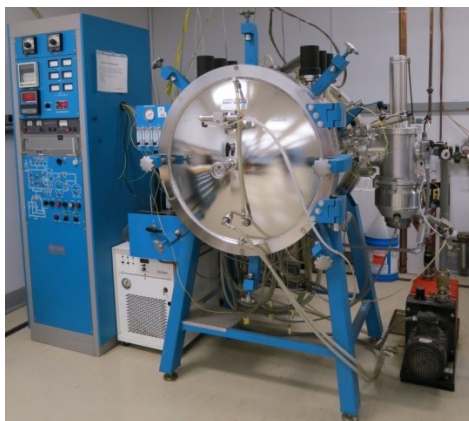


Figure 19: Oxy-Gon Industries Inc. (Epsom, NH, USA) C700 Vacuum Furnace

3.1.6 SEM

All images and composition data were obtained using a Phillips XL30S Schottky-based FEG (Field Emission Gun) SEM (Scanning Electron Microscope) coupled with an EDAX (Energy Dispersive Analysis of X-Rays) detector system (Figure 20a) or a VegaIXMU SEM (Tescan, Netherlands) and INCA x-act EDAX system (Oxford, England) (Figure 20b).

a)



b)



Figure 20: Scanning Electron Microscopes a) Philips XL30S Schottky-based Field Emission Gun (FEG) SEM, b) VegaIXMU SEM (Tescan, Netherlands)

SEM was used to acquire images as well as to determine composition. In SEM the electron beam interacts with atoms within the sample, exciting the emission of X-rays with

energies characteristic of the atomic number of the atoms involved [8]. A detector “collects” these emitted x-rays. A back-scattered electron (BSE) detector specifically collects electrons scattered as a function of sample composition and produces a BSE image in which coloration is proportional to average atomic weight (lighter areas have relatively higher average atomic weight). A secondary electron (SE) detector collects electrons scattered as a function of surface topography. In conjunction with a BSE detector, x-rays can be collected, analysed according to energy, and counted using the EDAX technique in order to acquire compositional data [8]. The spatial resolution of EDAX is limited by electron scattering within the solid and is typically 1-2 μm [8]. When appropriate standards and correction procedures are used, the technique is quantitative, yielding reliable compositional data for metals, but only semi-quantitative results for oxygen and, at best, qualitative results for carbon [8]. Although oxygen quantities can only be measured semi-quantitatively, it is reported that a phase containing <8 at. % Ni and >35 at. % Al+Cr can be confidently identified as $(\text{Cr}, \text{Al})_2\text{O}_3$ whereas NiAl_2O_4 contains 13-16 at. % Ni and 27-30 at. %Al [86]. To further increase confidence, EDAX was used in conjunction with X-Ray Diffraction technology (3.1.7).

3.1.7 XRD

XRD analysis was performed using a Bruker AXS D8 Discover diffractometer, shown in Figure 21, controlled with General Area Detector Diffractometer Software (GADDS). The samples were scanned from 25-100° (of 2θ angle) with a step size of 0.02/step (1S).



Figure 21: Bruker AXS D8 Discover diffractometer

In X-ray diffraction (XRD), the reacted sample is placed horizontally into the specimen holder of the diffractometer (Figure 21), so that the X-ray beam falls on the flat surface, and the intensity of diffracted beams can be measured using a detector [8]. Matching the resulting diffraction pattern with tabulated standards then leads to phase identification [8]. At the wavelengths and intensities normally used, X-rays penetrate only a short depth (1-3 μm) into the sample, so the technique only provides information near the sample surface [8].

3.2 Sample Preparation

Three substrate materials, IN738LC, CMSX-4 and René N5, were used in this study. IN738LC was cast by Sophisticated Alloy, Inc., CMSX-4 was cast by Howmet International and René N5 was provided by General Electric. The following section describes how these samples were prepared for various experiments described in detail in Section 3.3.

3.2.1 Un-Coated

IN-738 and CMSX-4 were received as 3/4" (~19 mm) and 5/8" (~16 mm) diameter solid bars, approximately 200 mm long. René N5 was received as 7/16" (~11 mm) x 1/4" (~6 mm) rectangular bars, approximately 75 mm long. René N5 samples were cut to a height of approximately 3 mm due to limited raw material; whereas IN-738 and CMSX-4 were both cut to heights of approximately 5 mm. The samples were cut using a Struers Secotom-10 (3.1.2). Sample surfaces were prepared using a Buehler Automatic Grinder/Polisher (3.1.1). BuehlerMet® II silicon carbide grinding papers of 180, 240, 320, 400, and 600 grit were used successively to achieve a final surface finish of 600 grit for all samples. Grinding reduced the heights of samples by approximately 1 mm yielding the approximate dimensions illustrated in Figure 22.

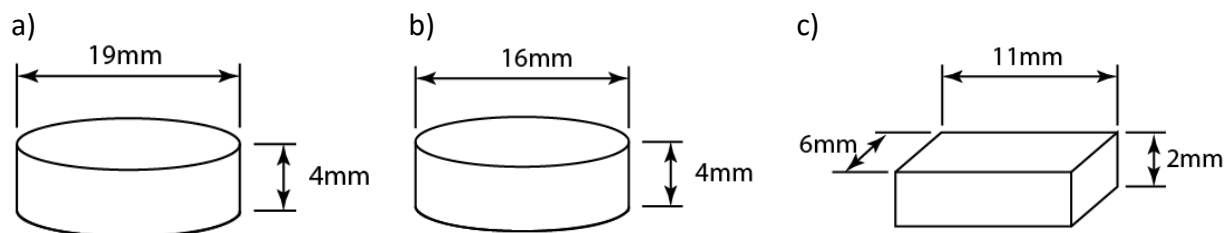


Figure 22: Overall dimensions of samples for a) IN-738, b) CMSX-4, c) René N5

After grinding, samples were ultrasonically cleaned in a Cole-Parmer 18001 ultrasonic cleaner using UltraMet® 2 sonic cleaning solution for 5 minutes followed by an ultrasonic cleaning in an acetone bath for 5 minutes and then rinsed with distilled water.

3.2.2 Coated

Only René N5 samples were coated based on oxidation results as shown in Section 4.2. Following the sample preparation procedure outlined in 3.2.1, the samples were placed in an atmospheric furnace (3.1.3) at 1150°C for 2 hrs, and then air-cooled to room temperature. SPS Columnar coatings were applied to [10] of these samples and SPS DVC coatings were applied to another [10] samples by Northwest Mettech utilizing Axial III Suspension Plasma Spraying (SPS) technology. In order for samples to adhere, grit blasting was required prior to coating deposition.

After coating, the samples were heat treated in a vacuum furnace (Section 3.1.5) to promote top coat/substrate adhesion. The samples were heated to 1080°C at a rate of 4°C/min, held for 4 hrs at 1080°C then furnace-cooled to room temperature.

3.2.3 Preparation of Cross-Sections

The procedure used to prepare all cross-sections prior to analysis regardless of whether the samples were coated or uncoated remains the same. In an attempt to preserve as much of the oxidized surface as possible, the entire sample was first cold-mounted with the oxidized or coated surface facing upward using a ratio of 1 part Buehler EpoxiCure® epoxy hardener to 5 parts Buehler EpoxiCure® epoxy resin. Once cured, the sample was cut using a Struers Secotom-10 (3.1.2) in such a way as to expose the cross-section. The sample was then cold-mounted a second time to achieve the proper orientation required for grinding and polishing. The sample surfaces were ground using the Buehler Automatic Grinder/Polisher (3.1.1).

BuehlerMet® II silicon carbide grinding papers of 180, 240, 320, 400, 600, 800 and 1200 were used successively. It should be noted that a minimum of 1/8" (~3 mm) of material was removed in the initial step of grinding utilizing the 180 grit silicon carbide grinding paper. This was done to ensure that any surface which may have been damaged in the cutting process was removed. Grinding was followed by polishing. Polishing was also done on a Buehler Automatic Grinder/Polisher (3.1.1). For polishing, 3 Micron Diamond K-Spray (Beta Diamond Products Inc.) was applied to an MD Chem polishing cloth, followed by ultrasonic cleaning in a Cole-Parmer 18001 ultrasonic cleaner using UltraMet® 2 sonic cleaning solution for 5 minutes. The samples were then polished further using 1 Micron Diamond K-Spray (Beta Diamond Products Inc.) applied to an MD Chem polishing cloth. Again, the polishing was followed by ultrasonic cleaning in a Cole-Parmer 18001 ultrasonic cleaner using UltraMet® 2 sonic cleaning solution for 5 minutes. The final polishing step was completed using MasterMet™ Colloidal Silica Polishing Suspension on an MD Chem polishing cloth. Polishing was followed by ultrasonic cleaning using UltraMet® 2 sonic cleaning solution and then by acetone for 5 minutes each.

3.2.4 Polished Samples

Several samples were polished to assess the as-received condition. The samples were prepared in the same way as is described in Section 3.2.1; however, grinding was continued using BuehlerMet® II silicon carbide grinding papers of 800 and 1200 grit. Grinding was followed by polishing which was also done using a Buehler Automatic Grinder/Polisher (3.1.1). For polishing, Beta Diamond Products Inc. 3 Micron Diamond K-Spray was applied to an MD Chem polishing cloth, followed by ultrasonic cleaning in a Cole-Parmer 18001 ultrasonic cleaner

using UltraMet® 2 sonic cleaning solution for 5 min. The samples were then polished further using Beta Diamond Products Inc. 1 Micron Diamond K-Spray applied to an MD Chem polishing cloth. Again, the polishing was followed by ultrasonic cleaning in a Cole-Parmer 18001 ultrasonic cleaner using UltraMet® 2 sonic cleaning solution for 5 minutes. The final polishing step was completed using MasterMet™ Colloidal Silica Polishing Suspension on an MD Chem polishing cloth. After all grinding and polishing, samples were ultrasonically cleaned in a Cole-Parmer 18001 ultrasonic cleaner using UltraMet® 2 sonic cleaning solution for 5 minutes followed by an ultrasonic cleaning in an acetone bath for 5 minutes.

3.3 Experimental Procedures

Experimental procedures used in this work are described in the following sections.

3.3.1 Assessment of Samples Prior to Testing

To assess the as-received condition of substrate materials; [1] CMSX-4, [1] IN-738 and [1] René N5 sample were prepared as per Section 3.2.4. These samples were then analyzed using SEM (3.1.6). To assess the condition of the as-coated samples, prepared as per Section 3.2.2, cross-sections were prepared as per Section 3.2.3 and analyzed using SEM (3.1.6).

3.3.2 Oxidation Testing of Uncoated IN-738, CMSX-4 and René N5

All isothermal oxidation tests were carried out using the atmospheric furnace (Section 3.1.3). All samples were prepared as per Section 3.2.1 prior to heat treatment. In all tests,

samples were placed in the atmospheric furnace (3.1.3) at 1150°C, held for a period of time (Table 6) and then removed from the furnace and air-cooled.

Table 6: Isothermal oxidation testing parameters

Sample	Duration (hrs)
[2] CMSX-4, [2] IN-738, [2] René N5	0.5
[2] CMSX-4, [2] IN-738, [2] René N5	1
[2] CMSX-4, [2] IN-738, [2] René N5	2
[2] CMSX-4, [2] IN-738, [2] René N5	4
[2] CMSX-4, [2] IN-738, [2] René N5	16

The surfaces of the samples were then analyzed using XRD (3.1.7) and SEM (3.1.6). One sample from each pair was cold-mounted as per Section 3.2.3. The cold mounted samples were analyzed using SEM (3.1.6).

3.3.3 Oxidation Testing of Coated René N5

Based on the preliminary results of the oxidation testing of the uncoated IN-738, CMSX-4 and René N5 (Section 0), it was decided that René N5 samples would be coated and tested further. To obtain an estimate of the number of cycles to failure (where failure is defined as 100% spallation of the top coat) the René N5 samples were cycled to failure as described in Section 3.3.3.1. Based on these results experiments were formulated to determine the progression of oxidation prior to failure under cyclic heating/cooling (Section 3.3.3.2) as well as at different isothermal oxidation times (Section 3.3.3.3).

3.3.3.1 *Coated René N5 Cycled to Failure*

All cyclic testing was conducted using a cyclic furnace (3.1.4). All samples were prepared as per Section 3.2.2 prior to testing. To determine the life of the samples, [3] samples

with a DVC top coat and [3] samples with a Columnar top coat were subjected to cyclic oxidation testing. Each cycle consisted of ramping up to 1150°C, holding for 50 min and cooling for 10 min; resulting in a furnace temperature profile as shown in Figure 23 for the first [3] complete cycles.

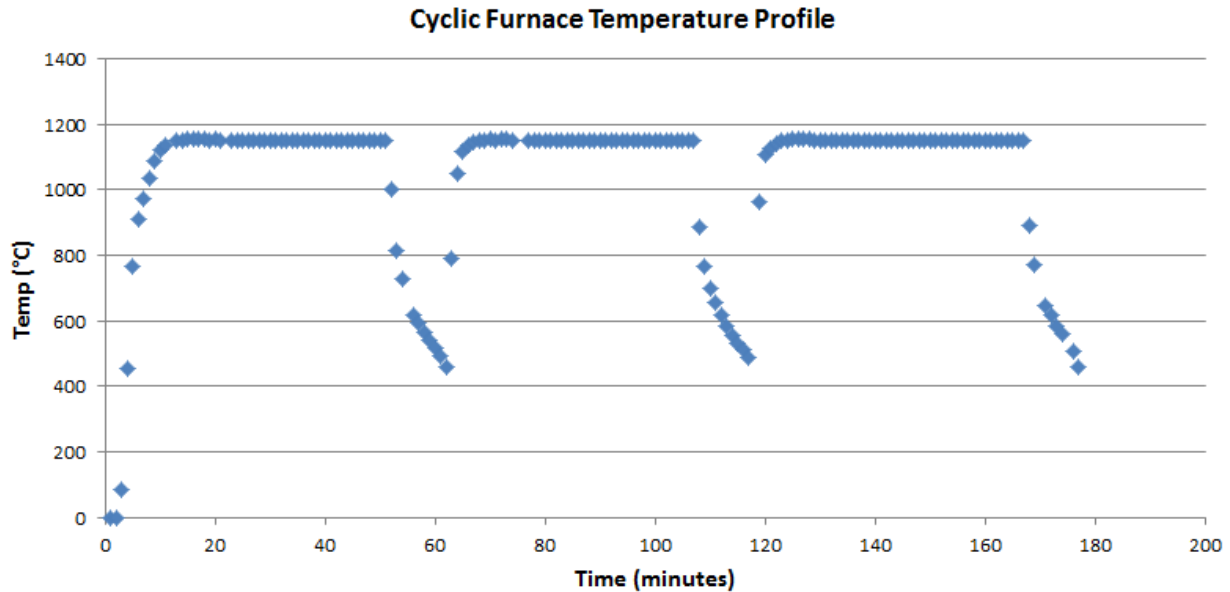


Figure 23: Cyclic Furnace Temperature Profile

The temperature of the samples will not match the profile provided in Figure 23 exactly as these measurements were obtained from a thermocouple mounted to the sample table and not directly to the samples themselves. After every [25] cycles the samples were removed from the furnace and the condition of the samples was documented prior to commencing another set of [25] cycles.

3.3.3.2 Cyclic Oxidation Testing of Coated René N5 Samples

The following tests were conducted to assess the progression of oxide growth and top coat degradation to failure. All samples were prepared as per Section 3.2.2. Samples were

placed in the cyclic furnace (3.1.4) for sets of [3] cycles with the goal of obtaining the total number of cycles indicated in Table 7.

Table 7: Parameters for incremental cyclic oxidation testing

Sample	Total Number of Cycles
[1] Columnar, [1] DVC	3
[1] Columnar, [1] DVC	6
[1] Columnar, [1] DVC	9

After every [3] cycles the samples were removed from the furnace and the condition of the samples was documented prior to commencing another set of [3] cycles. Each set of [3] cycles follows the temperature profile shown in Figure 23; however at the end of the third cycle, the samples are cooled to room temperature prior to the commencement of the next set of three cycles. Surfaces of the samples were analyzed using SEM (3.1.6). Additionally, cross-sections were prepared as per Section 3.2.3. The cross-sections were analyzed using SEM (3.1.6).

3.3.3.3 Isothermal Oxidation Testing of Coated René N5 Samples

The following tests were conducted to assess the progression of oxide growth and top coat degradation. All samples were prepared as per Section 3.2.2. The heat treatment used for all samples in this test was the same with the exception of holding time. In all tests, the atmospheric furnace (3.1.3) was pre-heated to 1150°C before the sample was placed inside and held for a period of time (Table 8). Samples were then air-cooled.

Table 8: Isothermal oxidation testing of coated samples

Sample	Number of Hours
[1] Columnar	4
[1] Columnar	6
[1] Columnar	10
[1] DVC	4
[1] DVC	6
[1] DVC	10

Once testing was complete, the surface of each sample was analyzed using SEM and XRD. Cross-sections were then prepared as per Section 3.2.3. The cross-sections were analyzed using SEM (3.1.6).

4 Results

This section summarizes the results of the experimental procedures described in Section 3.3.

4.1 Assessment of Samples Prior to Testing

This section summarizes the results of the experimental procedure described in Section 3.3.1 for IN-738, CMSX-4 and René N5 as well as for the DVC and Columnar samples.

4.1.1 IN-738

The average composition of IN-738 used in this study was measured and is provided in Table 9. It is comparable to compositions reported in literature (Table 2) [4].

Table 9: Composition of IN-738

	Al	Co	Cr	Mo	Nb	Ni	Ta	Ti	W	Zr
at. %	6.93	8.2	18.06	1.23	0.53	58.99	0.68	4.28	1.04	0.07
wt. %	3.24	8.38	16.29	2.05	0.85	60.06	2.13	3.55	3.32	0.11

The macrostructure of IN-738 can be seen in Figure 24. There are three regions as illustrated in Figure 24b and Figure 24c. The border between regions 2 and 3 is often not distinct as can be noted in Figure 24a, indicating that there is a gradual shift in composition between these regions. However, some distinct boundaries between these regions can be observed as can be seen in Figure 24a, Figure 24b and Figure 24c. The average composition of each region as well as the difference between the compositions of each region and the composition listed in Table 9 is provided in Table 10.

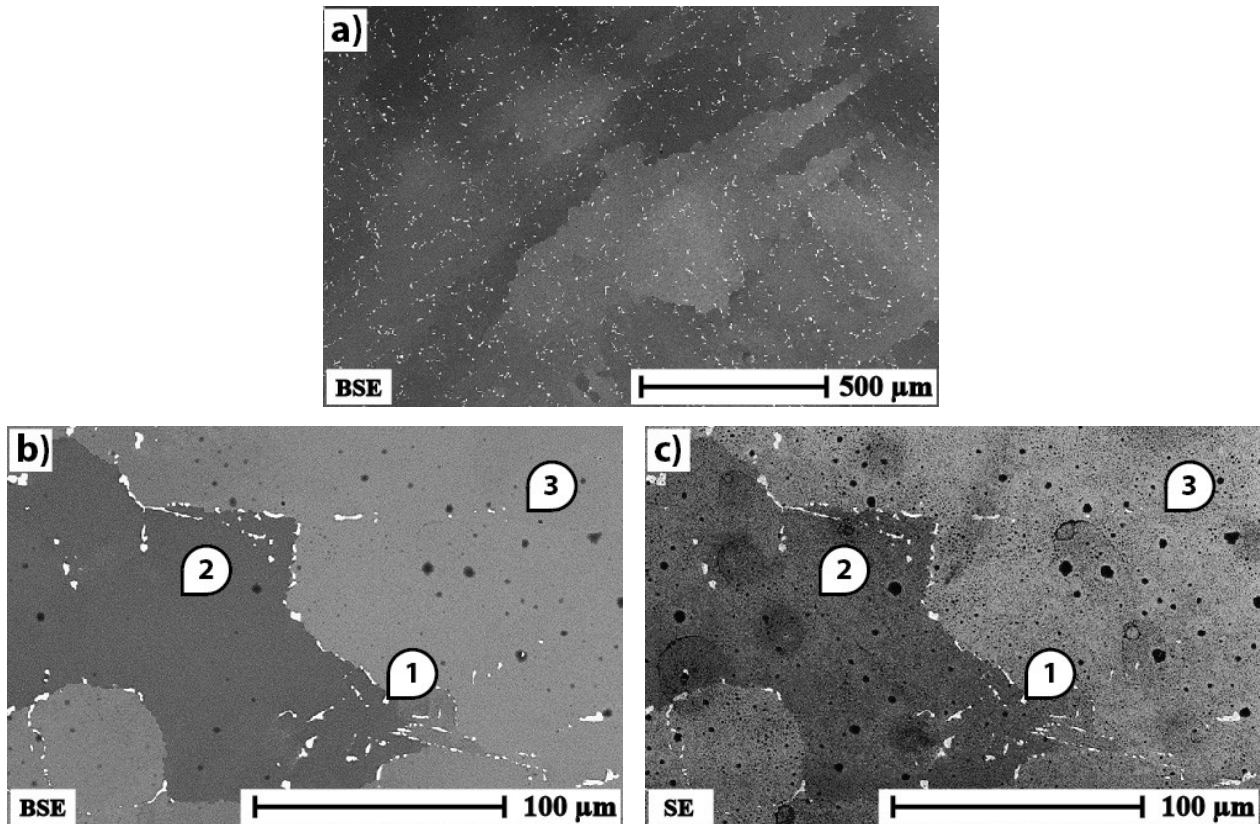


Figure 24: As-received IN-738 a) macrostructure, b) and c) BSE and SE images illustrating the compositionally different regions found on the surface

Table 10: IN-738: a) Average composition of Regions 1, 2 and 3, b) Difference between average composition of Regions 1, 2 and 3 and the composition provided in Table 9

a)				b)			
	Average (at. %)				Difference (at. %)		
Element	Region 1	Region 2	Region 3	Element	Region 1	Region 2	Region 3
Al	0.28	6.84	7.17	Al	-6.65	-0.09	0.24
Co	1.28	8.00	7.97	Co	-6.92	-0.20	-0.23
Cr	3.81	17.92	17.9	Cr	-14.25	-0.14	-0.16
Mo	2.70	1.25	1.11	Mo	1.47	0.02	-0.12
Nb	20.12	0.46	0.43	Nb	19.59	-0.07	-0.10
Ni	9.34	59.52	59.47	Ni	-49.65	0.53	0.48
Ta	15.59	0.37	0.38	Ta	14.91	-0.31	-0.30
Ti	43.32	4.85	4.72	Ti	39.04	0.57	0.44
W	2.92	0.66	0.73	W	1.88	-0.38	-0.31
Zr	0.68	0.13	0.13	Zr	0.61	0.06	0.06

a)

	Average (wt. %)		
Element	Region 1	Region 2	Region 3
Al	0.09	3.25	3.41
Co	0.89	8.31	8.28
Cr	2.34	16.42	16.41
Mo	3.07	2.11	1.88
Nb	22.12	0.75	0.7
Ni	6.49	61.55	61.54
Ta	33.38	1.18	1.21
Ti	24.54	4.09	3.98
W	6.35	2.14	2.37
Zr	0.73	0.21	0.21

b)

	Difference (wt. %)		
Element	Region 1	Region 2	Region 3
Al	-3.15	0.01	0.17
Co	-7.49	-0.07	-0.1
Cr	-13.95	0.13	0.12
Mo	1.02	0.06	-0.17
Nb	21.27	-0.1	-0.15
Ni	-53.57	1.49	1.48
Ta	31.25	-0.95	-0.92
Ti	20.99	0.54	0.43
W	3.03	-1.18	-0.95
Zr	0.62	0.1	0.1

Titanium, Niobium and Tantalum segregate significantly to Region 1 and there is some Tungsten and molybdenum segregation to this region as well. Regions 2 and 3 have no substantial compositional difference as would be expected for a fully homogenized material.

A higher magnification reveals the γ' microstructure of the material as shown in Figure 25 with γ' precipitates averaging approximately 800 nm across the diagonal, which is similar to the 700 nm reported by other authors [17]. These precipitates are relatively fine as is expected of a fully solutionized material.

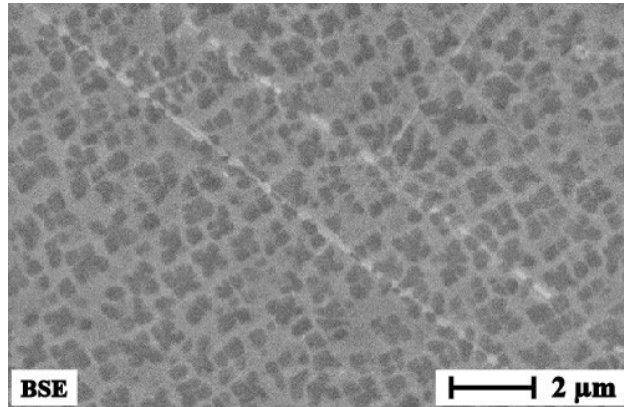


Figure 25: γ' microstructure of IN-738

4.1.2 CMSX-4

The average composition of CMSX-4 used in this study was measured and is provided in Table 11. It is comparable to that which is reported in literature (Table 3) [19].

Table 11: Composition of CMSX-4

	Al	Co	Cr	Hf	Mo	Ni	Re	Ta	Ti	W
at. %	11.94	10.11	7.82	0.09	0.4	62.47	1.18	2.13	1.4	2.47
wt. %	5.22	9.65	6.59	0.26	0.62	59.41	3.56	6.24	1.09	7.36

The macrostructure of the as-received CMSX-4 can be seen in Figure 26. There is a very slight compositional difference resulting from the dendritic structure which has persisted in spite of homogenizing heat treatments. Primary dendrite arms and dendrite cores are labeled as Region 1 and interdendritic regions are labeled as Region 2 in Figure 26.

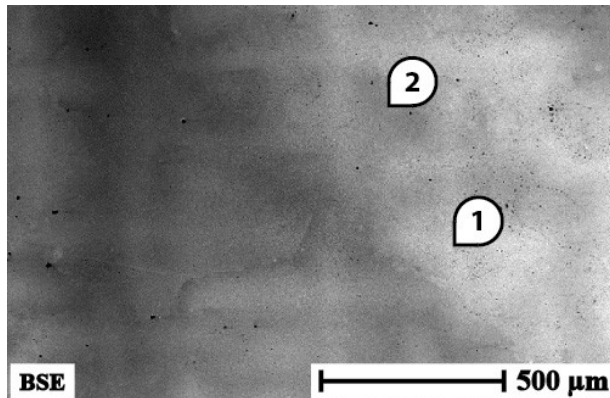


Figure 26: As-received CMSX-4

The average composition of each region as well as the difference between the compositions of each region and the composition listed in Table 11 is provided in Table 12.

Table 12: CMSX-4: a) Average composition of Regions 1 and 2, b) Difference between average composition of Regions 1 and 2 and the composition provided in Table 11

a)

Element	Average (at. %)	
	1	2
Al	11.81	12.48
Co	10.28	10.02
Cr	7.87	7.37
Hf	0.12	0.04
Mo	0.54	0.47
Ni	61.99	62.93
Re	1.49	1.02
Ta	1.97	2.03
Ti	1.39	1.5
W	2.56	2.17

b)

Element	Difference (at. %)	
	1	2
Al	-0.13	0.54
Co	0.17	-0.09
Cr	0.05	-0.45
Hf	0.03	-0.05
Mo	0.14	0.07
Ni	-0.48	0.46
Re	0.31	-0.16
Ta	-0.16	-0.10
Ti	-0.01	0.10
W	0.09	-0.30

a)

Element	Average (wt. %)	
	1	2
Al	5.13	5.53
Co	9.75	9.71
Cr	6.58	6.3
Hf	0.34	0.12
Mo	0.83	0.74
Ni	58.53	60.71
Re	4.46	3.12
Ta	5.73	6.04
Ti	1.07	1.18
W	7.57	6.56

b)

Element	Difference (wt. %)	
	1	2
Al	-0.09	0.31
Co	0.1	0.06
Cr	-0.01	-0.29
Hf	0.08	-0.14
Mo	0.21	0.12
Ni	-0.88	1.3
Re	0.9	-0.44
Ta	-0.51	-0.2
Ti	-0.02	0.09
W	0.21	-0.8

From the data summarized in Table 12 the composition of CMSX-4 is quite homogenous. However, there does appear to be slight segregation of Al, Ni and Ti to the interdendritic regions. Segregation of Al, Ta, Ti and Ni have been reported by other authors; however, this segregation was noted prior to solutionizing heat treatments [14, 23, 22]. Ta, Ti and Al are reported to enrich the eutectic phase even after solutionizing heat treatments [21] and as the eutectic and interdendritic regions could not be distinguished using BSE, it is possible that Region 2 is an average of both interdendritic and eutectic regions and the slight enrichment of Al and Ti observed is due to the enrichment of the eutectic region. Cr, Re and W segregate to the dendritic regions which has been reported in other work [21, 24]. Overall, there is no significant segregation and oxidation is anticipated to proceed uniformly. A higher magnification reveals the γ' microstructure (Figure 27) with γ' precipitates averaging approximately 490 nm across the diagonal.

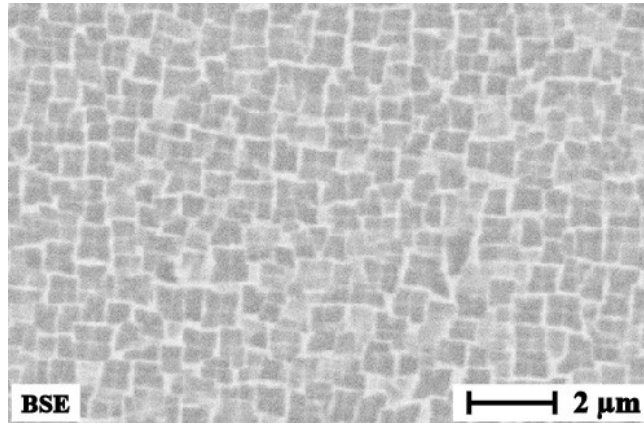


Figure 27: γ' microstructure of CMSX-4

4.1.3 René N5

The average composition of René N5 used in this study was measured and is provided in Table 13. The composition is comparable to the nominal composition reported in literature (Table 4) [26].

Table 13: Composition of René N5

	Al	Co	Cr	Hf	Mo	Ni	Re	Ta	W
at. %	12.45	7.7	8.2	0.19	1.15	65.09	0.91	2.3	2.03
wt. %	5.47	7.39	6.94	0.55	1.8	62.23	2.76	6.78	6.08

The macrostructure can be seen in Figure 28, in which three distinct regions have been identified. Region 1 corresponds to a eutectic phase. Region 2, immediately adjacent to the eutectic region, is an interdendritic region. Region 3 corresponds to the dendritic regions. The average composition of each region as well as the difference between the compositions of each region and the composition listed in Table 13 is provided in Table 14.

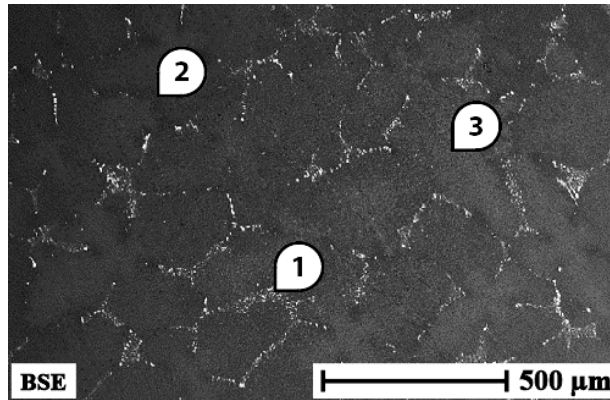


Figure 28: As-received René N5

Table 14: René N5 a) Average composition of Regions 1, 2 and 3, b) Difference between average composition of Regions 1, 2 and 3 and composition provided in Table 13

a)

Element	Average (at. %)		
	1	2	3
Al	12.53	13.13	12.23
Co	7.34	7.68	8.21
Cr	8.36	8.28	8.51
Hf	0.29	0.21	0.03
Mo	1.22	0.88	1.04
Ni	63.22	64.57	64.71
Re	0.59	1.1	1.32
Ta	4.69	2.24	1.83
W	1.76	1.95	2.13

b)

Element	Difference (at. %)		
	1	2	3
Al	0.08	0.68	-0.22
Co	-0.36	-0.02	0.51
Cr	0.16	0.08	0.31
Hf	0.1	0.02	-0.16
Mo	0.07	-0.27	-0.11
Ni	-1.87	-0.52	-0.38
Re	-0.32	0.19	0.41
Ta	2.39	-0.06	-0.47
W	-0.27	-0.08	0.1

a)

Element	Average (wt. %)		
	1	2	3
Al	5.31	5.79	5.38
Co	6.79	7.4	7.9
Cr	6.83	7.04	7.22
Hf	0.81	0.61	0.09
Mo	1.84	1.38	1.63
Ni	58.28	61.95	61.98
Re	1.73	3.35	4.01
Ta	13.33	6.63	5.4
W	5.08	5.86	6.39

b)

Element	Difference (wt. %)		
	1	2	3
Al	-0.16	0.32	-0.09
Co	-0.6	0.01	0.51
Cr	-0.11	0.1	0.28
Hf	0.26	0.06	-0.46
Mo	0.04	-0.42	-0.17
Ni	-3.95	-0.28	-0.25
Re	-1.03	0.59	1.25
Ta	6.55	-0.15	-1.38
W	-1	-0.22	0.31

Ta and Hf segregate to the eutectic phase. The eutectic region is depleted of W and Re. The dendritic region is enriched with W and Re and is depleted of Al and Ta as has been reported elsewhere [25]. The dendritic regions also have slightly higher concentrations of Co and Cr and are depleted of Hf. The interdendritic regions have slightly higher Al concentration and lower Mo concentration.

4.1.4 René N5 SPS DVC

Images of the DVC coated samples prepared as per Section 3.3.1 are provided in Figure 29. Compositions of regions identified in Figure 29 are provided in Table 15.

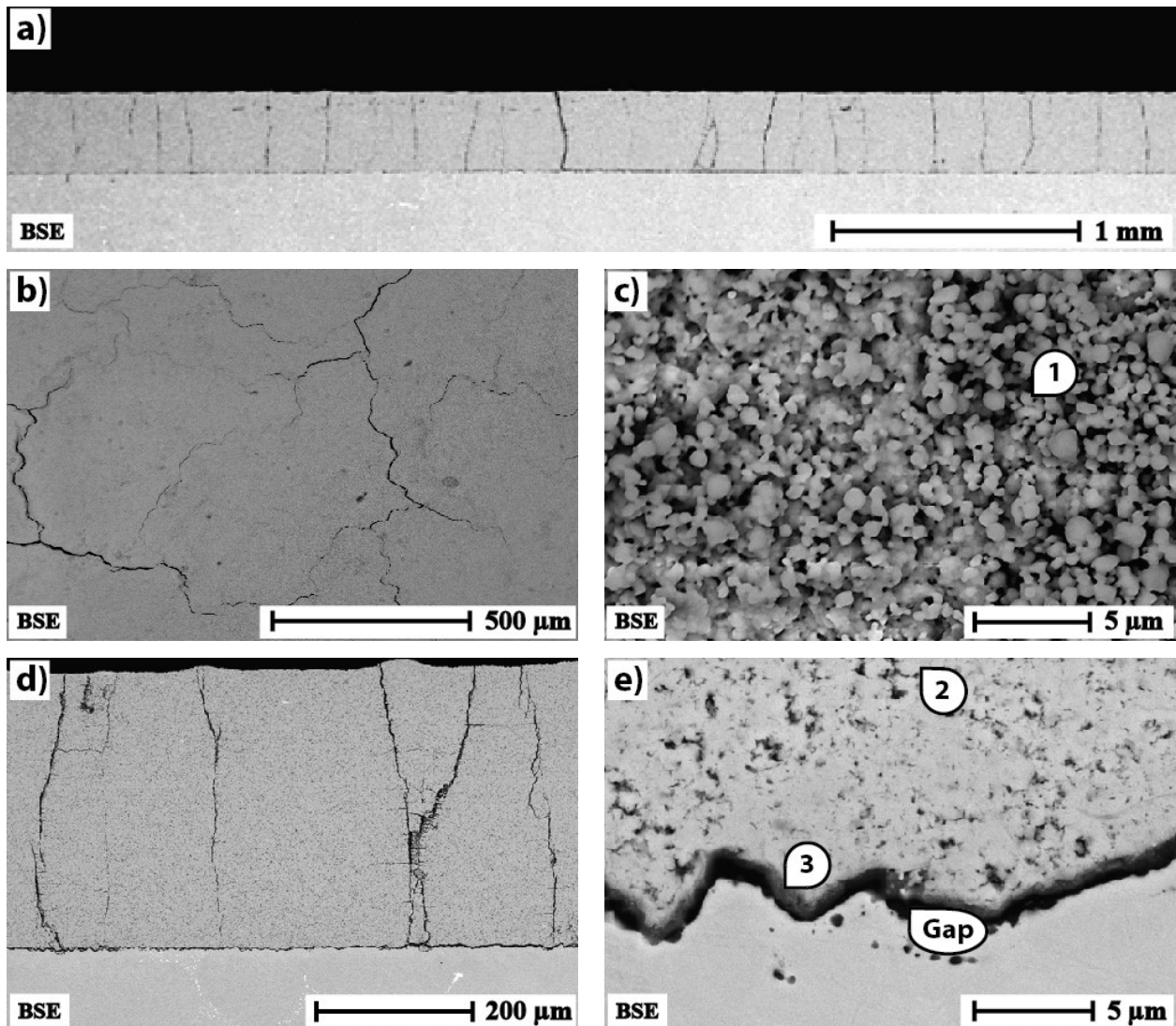


Figure 29: As-coated DVC sample. a) macrostructure of coating, b) morphology of coating surface, c) round clusters of yttria partially stabilized zirconia, d) segmentation cracks and e) substrate/coating interface

Table 15: Composition of regions identified in Figure 29

Element	at. %		
	1	2	3
Al	-	1.52	22.67
Co	-	1.00	2.46
Cr	-	1.51	2.90
Ni	-	9.90	17.48
O	72.54	57.52	45.61
Y	3.58	1.75	-
Zr	23.88	26.79	8.89

Element	wt. %		
	1	2	3
Al	-	0.96	17.61
Co	-	1.38	4.17
Cr	-	1.83	4.34
Ni	-	13.58	29.53
O	31.73	21.51	21
Y	8.7	3.64	-
Zr	59.56	57.11	23.34

The coating has an average height of 348 μm with regular, repeating segmentation cracks extending through the coating thickness (Figure 29a, Figure 29b and Figure 29d) and is quite similar in appearance to SDS DVC coatings reported in literature (Figure 9) [35]. As seen from the surface the coating morphology consists of small, round clusters of yttria partially stabilized zirconia with a Zr to Y ratio in at. % of approximately 6.7:1 (Figure 29c). There is a significant amount of Ni diffused into the coating (Figure 29e, Region 2), about 5-10 μm from the substrate/coating interface, presumably resulting from the diffusion heat treatment.

There is a gap between the substrate and the coating (Figure 29e). Inside the gap, pieces of dark-coloured oxide with an average thickness of approximately 1.25 μm are adhered intermittently to either the substrate or top coat (Figure 29e, Region 3). As EDAX resolution is 1-2 μm , definitive conclusions cannot be reached as to the composition of this region. However, there is a higher proportion of Al.

4.1.5 René N5 SPS Columnar

Images of the columnar coated samples prepared as per Section 3.3.1 are provided in Figure 30. Compositions of regions identified in Figure 30 are provided in Table 16.

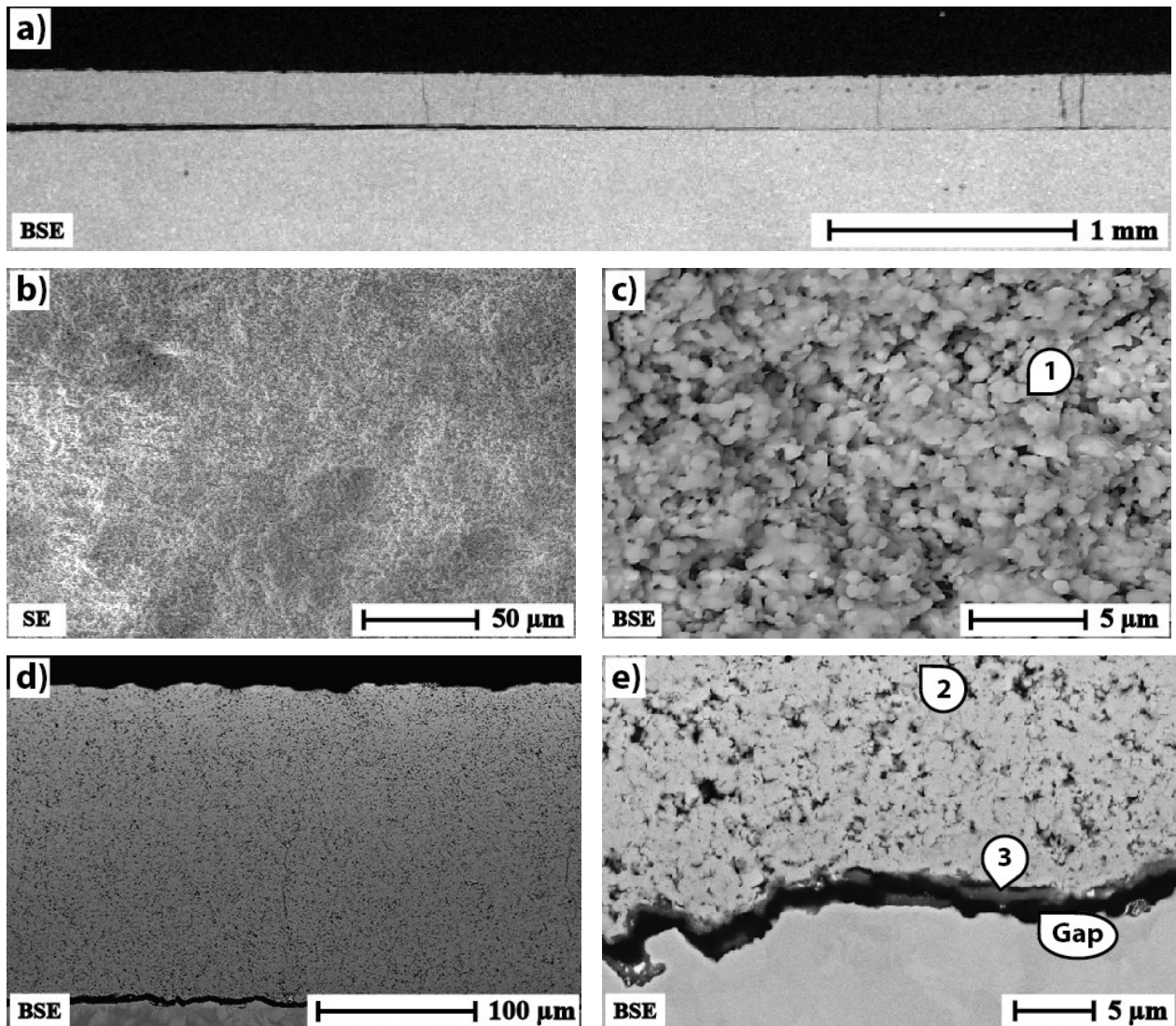


Figure 30: As-coated Columnar sample. a) macrostructure of coating, b) morphology of coating surface, c) round clusters of yttria partially stabilized zirconia, d) columnar structure and e) substrate/coating interface

Table 16: Composition of regions identified in Figure 30

Element	at. %		
	1	2	3
Al	-	1.44	22.63
Co	-	1.12	1.48
Cr	-	1.5	1.96
Ni	-	9.49	11.14
O	71.26	58.19	56.54
Y	3.58	2.3	0.07
Zr	25.16	25.96	6.17

Element	wt. %		
	1	2	3
Al	-	0.92	20.86
Co	-	1.56	2.98
Cr	-	1.84	3.48
Ni	-	13.13	22.34
O	30.37	21.94	30.9
Y	8.48	4.82	0.21
Zr	61.15	55.81	19.23

The coating has an average height of 224 μm . Although there are sporadically located vertical cracks which extend, in some cases, through the coating thickness; a definitive columnar coating structure is not evident (Figure 30a, Figure 30b and Figure 30d) and it does not seem to match the structure of SPS Columnar coatings reported in literature (Figure 9) [35]. As seen from the surface; the coating morphology consists of small, round clusters of yttria partially stabilized zirconia with a Zr to Y ratio in at. % of approximately 7:1 (Figure 30c). There is a significant amount of Ni diffused into the coating (Figure 30e, Region 2) within approximately 10-15 μm from the substrate/coating interface, presumably resulting from the diffusion heat treatment.

There is a gap between the substrate and the coating which varies in width across the length of the sample (Figure 30a). At the lowest point, the gap is approximately 2.39 μm . Inside the gap, pieces of dark-coloured oxide are adhered intermittently to either the substrate or top coat (Figure 30c). The average height of these pieces of oxide is approximately 1 μm (Figure 30e, Region 3). As EDAX resolution is 1-2 μm , definitive conclusions cannot be reached as to the composition of this region. However, the Al concentration is greater than that measured in the substrate.

4.2 Oxidation Results of Uncoated IN-738, CMSX-4 and René N5

This section details the results obtained from the experiment described in Section 3.3.2.

4.2.1 IN-738

Images of the samples after heat treatment are provided in Figure 31.

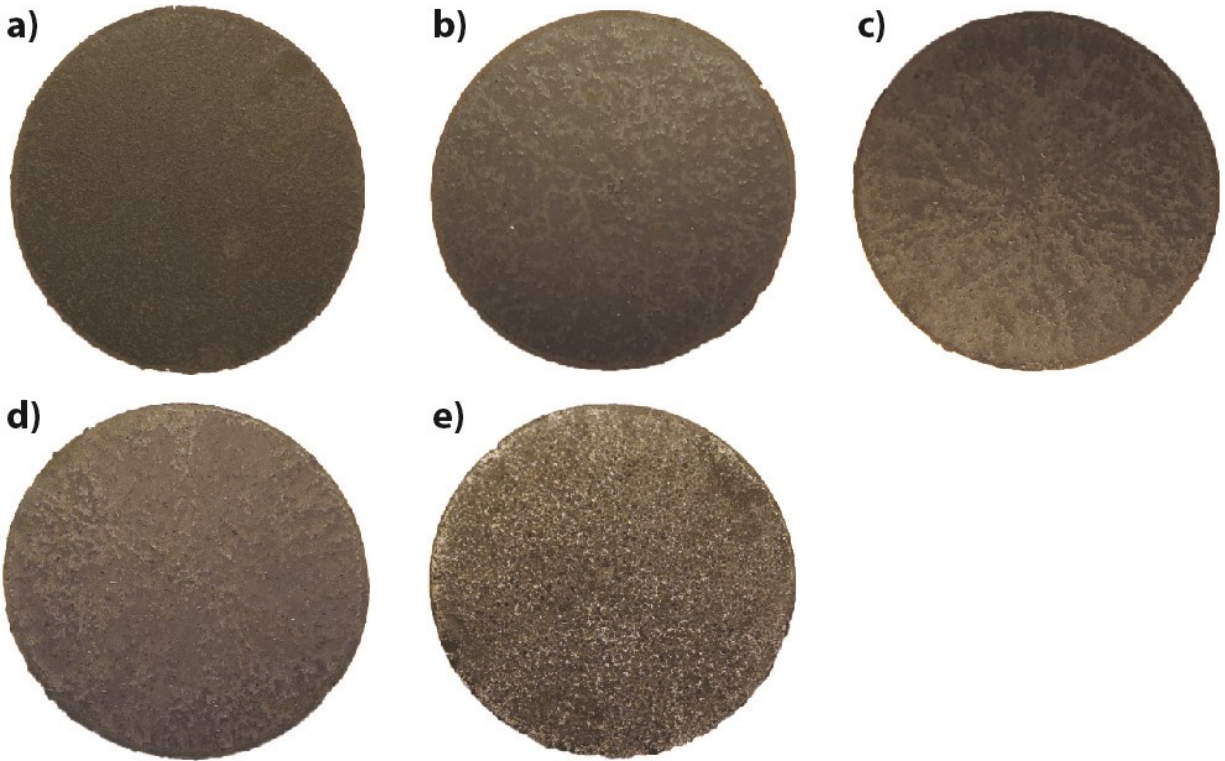


Figure 31: IN-738 oxidized at 1150°C for a) 0.5 hrs, b) 1 hr, c) 2 hrs, d) 4 hrs and e) 16 hrs

The appearance of the sample surface changes slightly between 4 and 16 hours suggesting spallation of previously developed oxides.

Images of the sample surface at 0.5, 1, 2, 4 and 16 hrs are provided in Figure 32. Dark regions in Figure 32 are oxides of relatively lower average atomic weight than those of the surrounding areas. These oxides develop in the earlier stages of oxidation (Figure 32a). As oxidation continues the proportion of the surface covered by these oxides decreases (Figure 32b, Figure 32c). After 4 hours of oxidation, only spalled fragments of these oxides remain on

the surface (Figure 32d) and the overall appearance of the surface changes slightly. After 16 hours of oxidation (Figure 32e) the surface has a noticeably different appearance suggesting the growth of new and most likely different oxides than were seen on the sample surface for 0.5, 1, 2 and 4 hours.

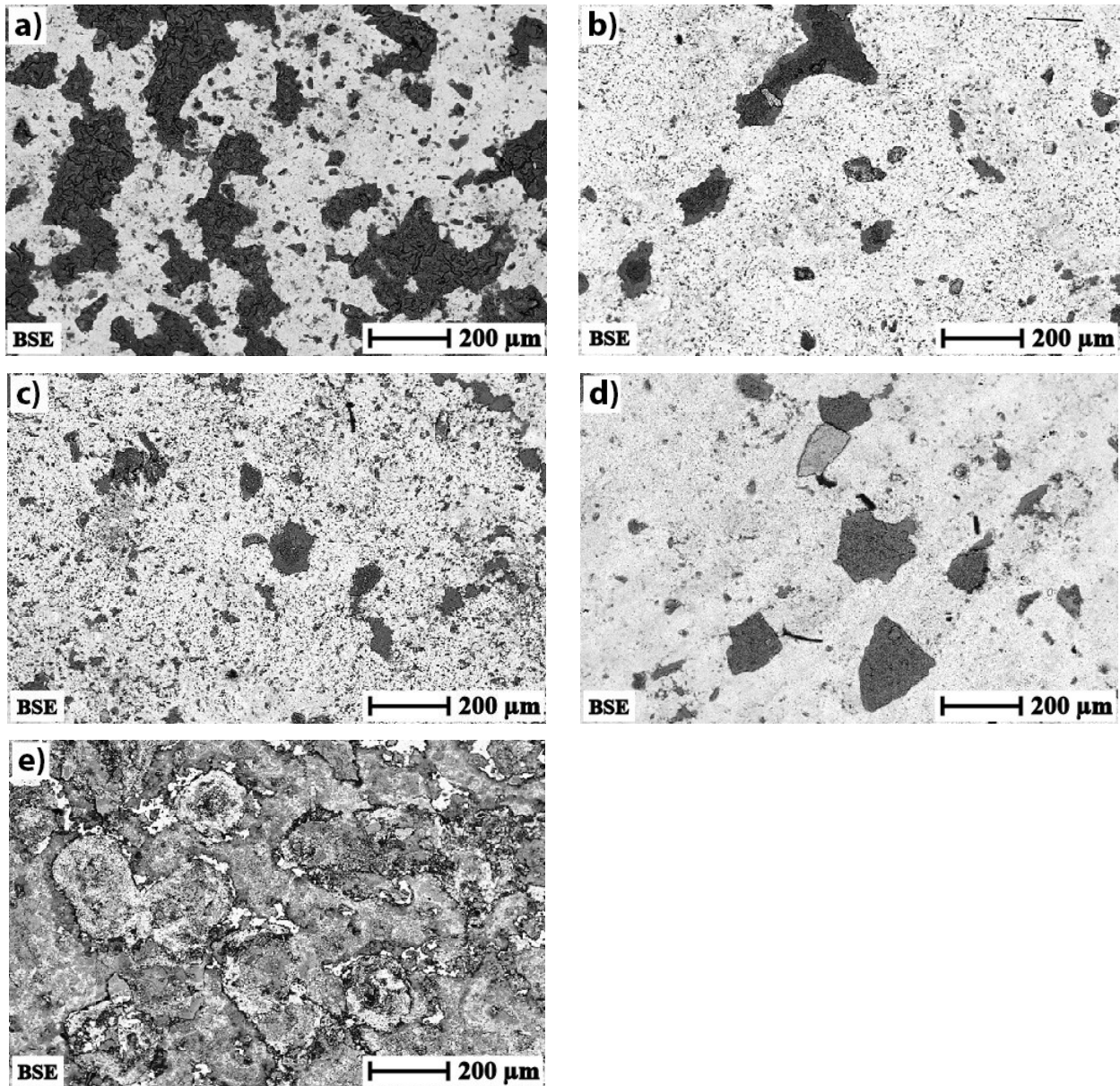


Figure 32: IN-738 oxidized at 1150°C for a) 0.5 hrs, b) 1 hr, c) 2 hrs, d) 4 hrs and e) 16 hrs

Figure 33 shows the progression of oxidation on the surface of the sample; where the labels on Figure 33 indicate the region number (1-4) and the letters indicate the heat treatment time (a=0.5 hrs, b=1 hr, c=2 hrs, d=4 hrs and e=16 hrs). Compositions of regions identified in Figure 33 are provided in Table 17. Region 1 is characterized by a high titanium and chromium content. Region 2 is characterized by high tantalum, niobium and titanium content whereas

Region 3 is characterized by high chromium content and Region 4 is characterized by high nickel content.

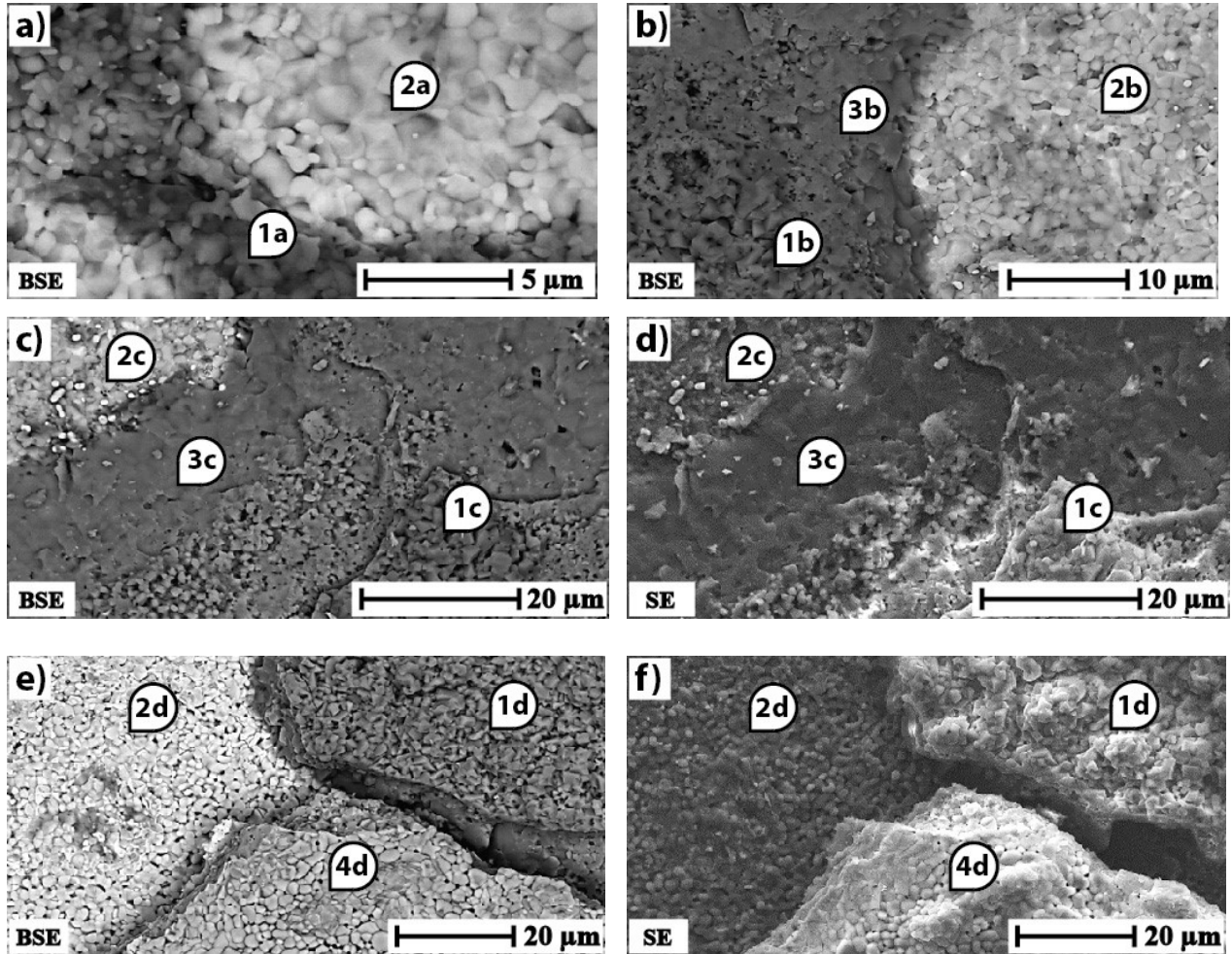


Figure 33: Surface of IN-738 oxidized at 1150°C. a) BSE image of sample oxidized for 0.5 hrs b) BSE image of sample oxidized for 1 hr, c) BSE image of sample oxidized for 2 hrs, d) SE image of sample oxidized for 2 hrs, e) BSE image of sample oxidized for 4 hrs f) SE image of sample oxidized for 4 hrs

Table 17: Composition of regions identified in Figure 33

	at. %										
Element	1a	1b	1c	1d	2a	2b	2c	2d	3b	3c	4d
Al	0.96	3.41	1.59	1.82	0.15	1.06	1.08	0.9	4.79	4.93	-
Co	-	-	-	-	3.06	2.2	2.44	2.27	-	-	2.95
Cr	23.24	18.99	11.78	12.18	5.76	5.7	8.47	6.68	33.78	35.77	3.09
Nb	1.27	1.03	0.98	0.44	4.09	3.98	2.8	3.41	-	-	-
Ni	3.42	1.77	1.07	0.24	15.54	12.79	11.05	12.35	-	-	45.96
O	59.33	55.84	62.39	62.92	55.64	56.83	58.82	56.13	60.22	57.67	45.88
Ta	-	-	-	-	4.07	3.92	2.65	3.92	-	-	-
Ti	11.77	18.96	22.75	22.41	11.68	13.5	11.69	14.34	1.2	1.64	2.12

	wt. %										
Element	1a	1b	1c	1d	2a	2b	2c	2d	3b	3c	4d
Al	0.84	2.99	1.48	1.74	0.1	0.74	0.83	0.63	4.45	4.44	-
Co	-	-	-	-	4.55	3.38	4.11	3.48	-	-	4.5
Cr	39.42	32.06	21.15	22.48	7.56	7.72	12.58	9.04	60.43	62.12	4.15
Nb	3.85	3.11	3.14	1.45	9.59	9.63	7.43	8.25	-	-	-
Ni	6.55	3.37	2.17	0.5	23.02	19.55	18.52	18.87	-	-	69.75
O	30.96	29.01	34.46	35.74	22.47	23.68	26.87	23.38	33.15	30.82	18.98
Ta	-	-	-	-	18.59	18.47	13.69	18.47	-	-	-
Ti	18.38	29.47	37.6	38.08	14.11	16.83	15.98	17.87	1.98	2.62	2.62

Figure 34 shows the progression of oxidation in cross-section, where the labels on Figure 33 indicate the region number (1-6) and the letters indicate the heat treatment time (a=0.5 hrs, b=1 hr, c=2 hrs, d=4 hrs and e=16 hrs). Regions labelled with the same number are believed to correspond (i.e. Region 1 of Figure 33 corresponds to Region 1 of Figure 34) and justification for these conclusions are provided in the following paragraphs. Compositions corresponding to regions identified in Figure 34 are provided in Table 18. Regions 1, 2 and 3 of Figure 33 and Figure 34 are the same. Aside from having similar composition (Table 17 and Table 18), the surface topography coincides with the layering of oxides seen in cross-section. Figure 33d and Figure 33f are SE images showing the topography of the sample at 2 and 4

hours, respectively. Figure 33f illustrates that Region 1 is at the highest elevation followed by Region 3 and then by Region 2. Figure 33d suggests that Region 3 forms beneath Region 1 and is revealed when Region 1 spalls. This is further corroborated by Figure 34a in which Region 1 forms the top layer, Region 3 forms an intermediate layer and Region 2 is directly beneath these regions.

Furthermore, the strain produced by the curing of the epoxy used to cold-mount (Section 3.2.3) produces a stress which consistently shears the interface between Regions 2 and 3 as illustrated in Figure 34b-f. This suggests that the lowest adhesion strength is between Regions 1 and 3. The low adhesion strength results in spallation of Regions 1 and 3 as a single piece of oxide, exposing Region 2 beneath.

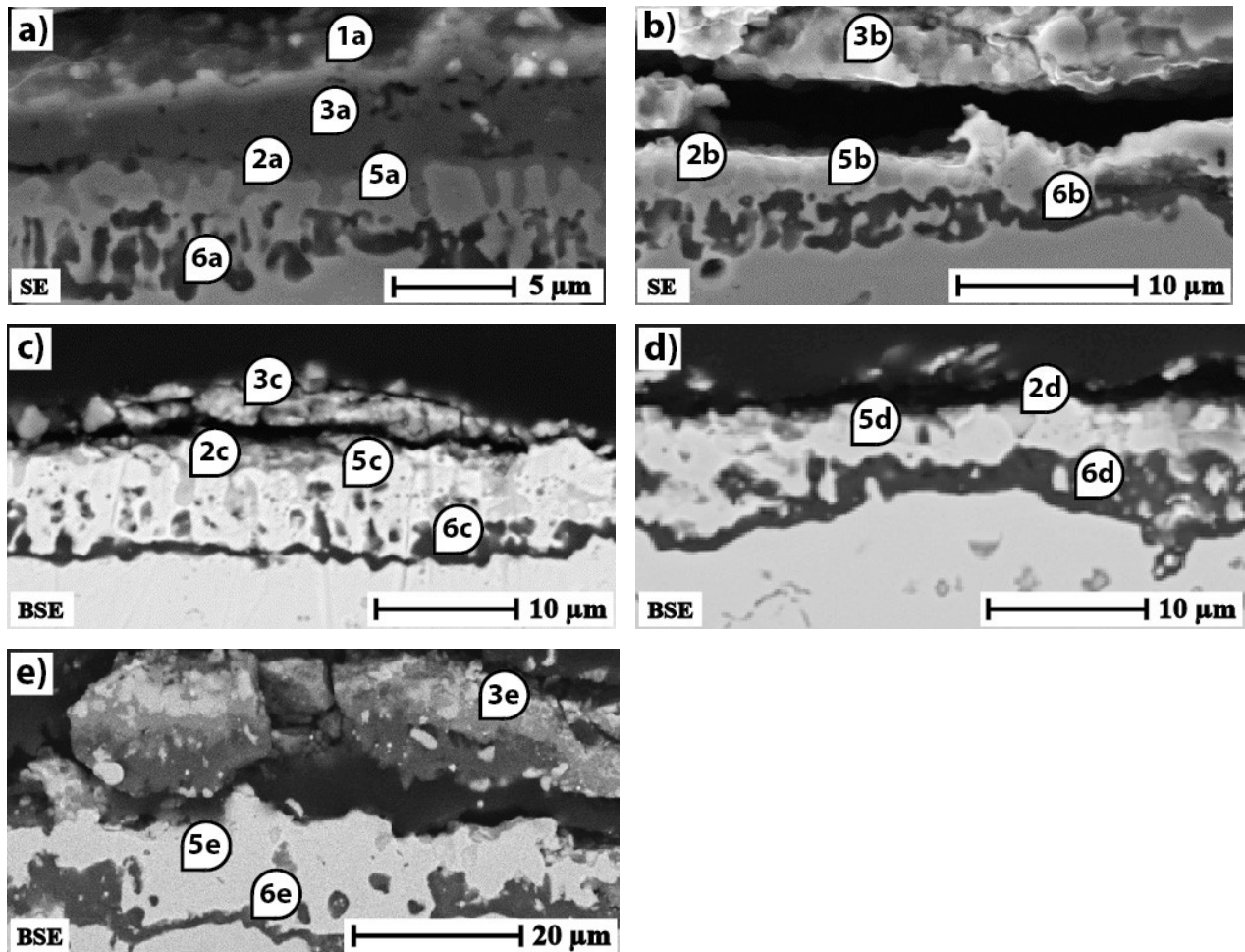


Figure 34: Cross-section of IN-738 oxidized at 1150°C. a) BSE image of sample oxidized for 0.5 hrs b) BSE image of sample oxidized for 1 hr, c) BSE image of sample oxidized for 2 hrs, d) BSE image of sample oxidized for 4 hrs e) BSE image of sample oxidized for 16 hrs

Table 18: Composition of regions identified in Figure 34

	at. %								
	1a	2a	2b	2c	2d	3a	3b	3c	3e
Al	1.79	1.06	-	2.81	-	3.17	5.19	6.92	9.69
Co	-	1.49	1.29	0.51	1.68	-	-	-	-
Cr	22.09	7.57	5.67	6.24	3.46	35.94	32.92	30.28	27.48
Nb	0.38	3.13	3.85	3.61	2.15	-	-	-	-
Ni	0.84	9.07	7.86	3.31	12.22	-	-	-	-
O	56.18	63.02	66.81	59.66	61.56	58.93	59.35	60.03	61.79
Ta	-	3.19	2.79	4.66	5.05	-	-	-	-
Ti	18.74	11.46	11.72	19.23	13.87	1.94	2.54	2.76	1.04

	5a	5b	5c	5d	5e	6a	6b	6c	6d	6e
Al	-	-	-	-	-	33.22	32.87	39.15	34.6	33.82
Co	12.19	10.12	11.58	1.09	-	1.51	1.94	0.94	0.28	-
Cr	3.13	2.85	0.91	0.7	-	0.86	0.5	1.17	1.09	-
Mo	2.27	2.89	2.04	-	-	-	-	-	-	-
Nb	-	2.3	-	-	-	-	-	-	-	-
Ni	75.11	63.1	82.28	94.75	99.9	9.9	11.24	5.6	1.79	-
O	5.79	4.72	2.24	3.45	0.1	54.5	53.45	53.14	62.24	66.18
Ta	-	3.43	-	-	-	-	-	-	-	-
Ti	-	8.77	-	-	-	-	-	-	-	-
W	1.5	1.83	0.95	-	-	-	-	-	-	-

	wt. %								
	1a	2a	2b	2c	2d	3a	3b	3c	3e
Al	1.57	0.82	-	2.06	-	2.86	4.79	6.54	9.58
Co	-	2.53	2.29	0.82	2.63	-	-	-	-
Cr	37.32	11.35	8.87	8.82	4.79	62.5	58.56	55.17	52.36
Nb	1.15	8.39	10.76	9.12	5.31	-	-	-	-
Ni	1.6	15.35	13.88	5.28	19.08	-	-	-	-
O	29.21	29.08	32.15	25.95	26.21	31.53	32.49	33.66	36.23
Ta	-	16.65	15.18	22.92	24.31	-	-	-	-
Ti	29.15	15.82	16.87	25.03	17.66	3.11	4.16	4.63	1.82

	5a	5b	5c	5d	5e	6a	6b	6c	6d	6e
Al	-	-	-	-	-	36.1	34.89	44.92	44.29	46.29
Co	12.23	9.33	11.44	1.12	-	3.58	4.5	2.36	0.78	-
Cr	2.77	2.32	0.79	0.64	-	1.8	1.02	2.59	2.69	-
Mo	3.71	4.34	3.28	-	-	-	-	-	-	-
Nb	-	3.34	-	-	-	-	-	-	-	-
Ni	75.03	57.95	80.96	97.27	99.97	23.4	25.95	13.98	4.98	-
O	1.58	1.18	0.6	0.97	0.03	35.12	33.64	36.16	47.25	53.71
Ta	-	9.71	-	-	-	-	-	-	-	-
Ti	-	6.57	-	-	-	-	-	-	-	-
W	4.69	5.26	2.93	-	-	-	-	-	-	-

An XRD analysis of a sample heat treated for 2 hrs (Figure 35), confirmed the presence of rutile-TiO₂ and Cr₂O₃. This suggests that Region 1 (Figure 33 and Figure 34) is comprised predominantly of rutile-TiO₂ and Cr₂O₃; whereas Region 3 (Figure 33 and Figure 34) is comprised predominantly of Cr₂O₃.

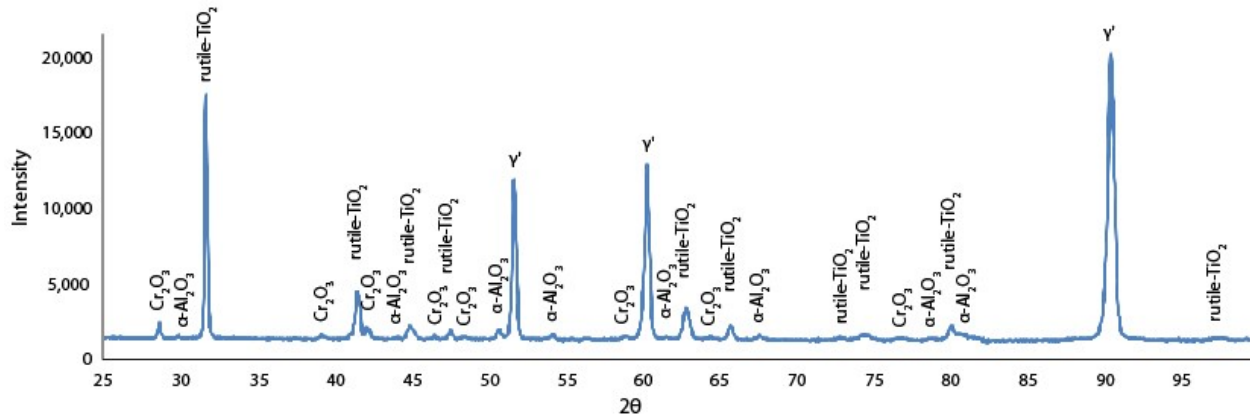


Figure 35: XRD results for IN-738 isothermally oxidized at 1150°C for 2 hrs

Cr_2O_3 has been identified as an external scale on IN-738 in several studies [9, 79, 80, 87]. Studies conducted at 1073°C and 900°C have also confirmed the presence of an external scale of rutile- TiO_2 [79, 80].

Region 4 of Figure 33f and Region 4 of Figure 34f are believed to be related. Both regions are characterized by high Nickel content and both emerge at later oxidation times (4 hrs and 16 hrs). This is corroborated by Figure 31 and Figure 32 in which there is a slight change in the appearance of the surface following 4 hrs of oxidation and a significant change in the surface after 16 hrs of oxidation. Regions of mixed Ni/Ti oxides have been reported to appear at later oxidation times (Zhu et.al [80] noted them after 4 hrs), similar to that observed in oxidation studies of IN-738 [79, 80].

Region 5 (Figure 33 and Figure 34) illustrates the change in composition of the substrate within the oxidized region over time in which Nickel content increases from 75.11 at. % after 0.5 hrs of oxidation to 99.90 at. % after 16 hrs of oxidation.

Region 6 has increasing aluminum content over time with 33.22 at. %Al after 0.5 hrs of oxidation and only Al and O present after 16 hrs of oxidation. The presence of Al and O in isolation strongly suggests the formation of Al_2O_3 . XRD analysis of a sample heat treated for 2 hrs (Figure 35), confirmed the presence of $\alpha\text{-Al}_2\text{O}_3$ and studies done by other authors have also found internal subscales of Al_2O_3 [79].

4.2.2 CMSX-4

Images of the samples after heat treatment are provided in Figure 36.

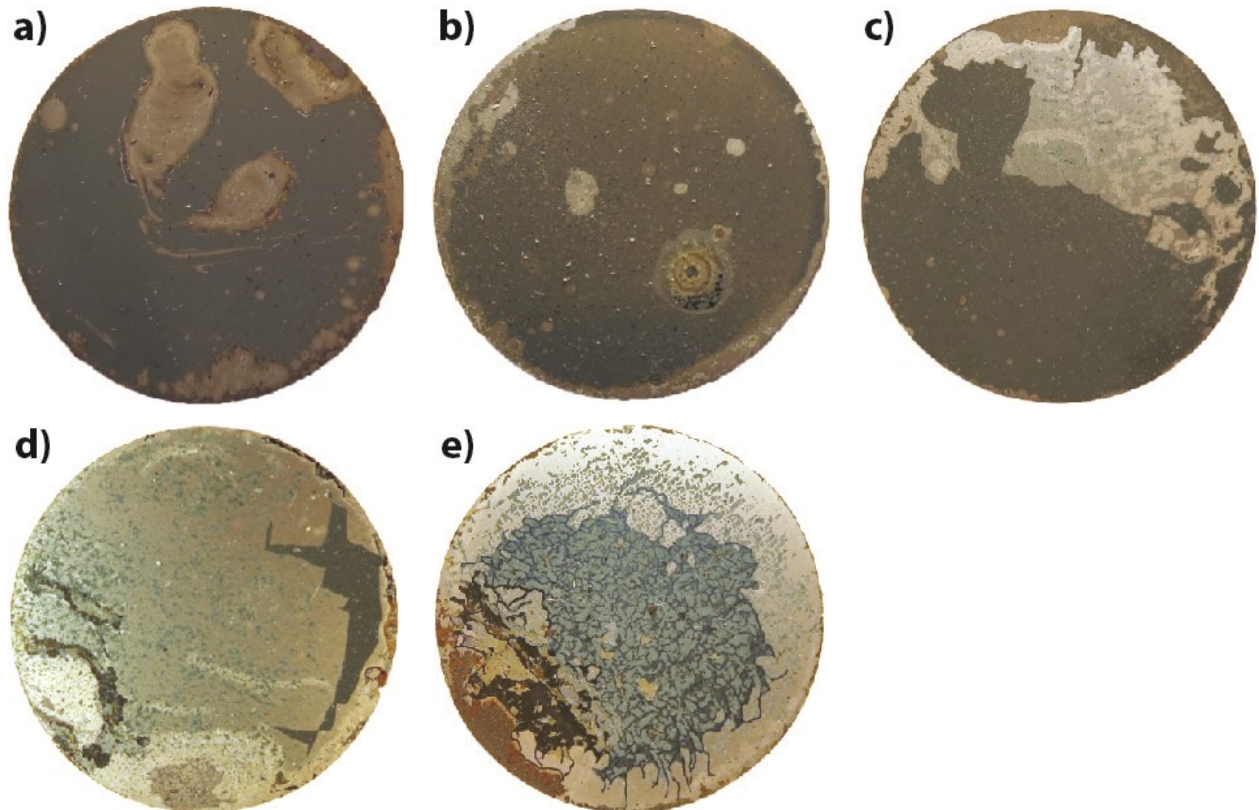


Figure 36: CMSX-4 oxidized at 1150°C for a) 0.5 hrs, b) 1 hr, c) 2 hrs, d) 4 hrs and e) 16 hrs

Images of the sample surface at 0.5, 1, 2, 4 and 16 hrs are provided in Figure 37. Spallation begins after 1 hr of oxidation (Figure 36c and Figure 37c). After 4 hrs of oxidation, the majority of the oxide formed in the earlier stages of oxidation has spalled (Figure 36d). However, some of the oxide remains on the surface (Figure 36d and Figure 37d). By 16 hrs of oxidation, the oxide developed during the earlier stages of oxidation has completely spalled and new oxides have developed (Figure 36e). However, spalled fragments of the previously formed oxides can still be found on the surface (Figure 37e).

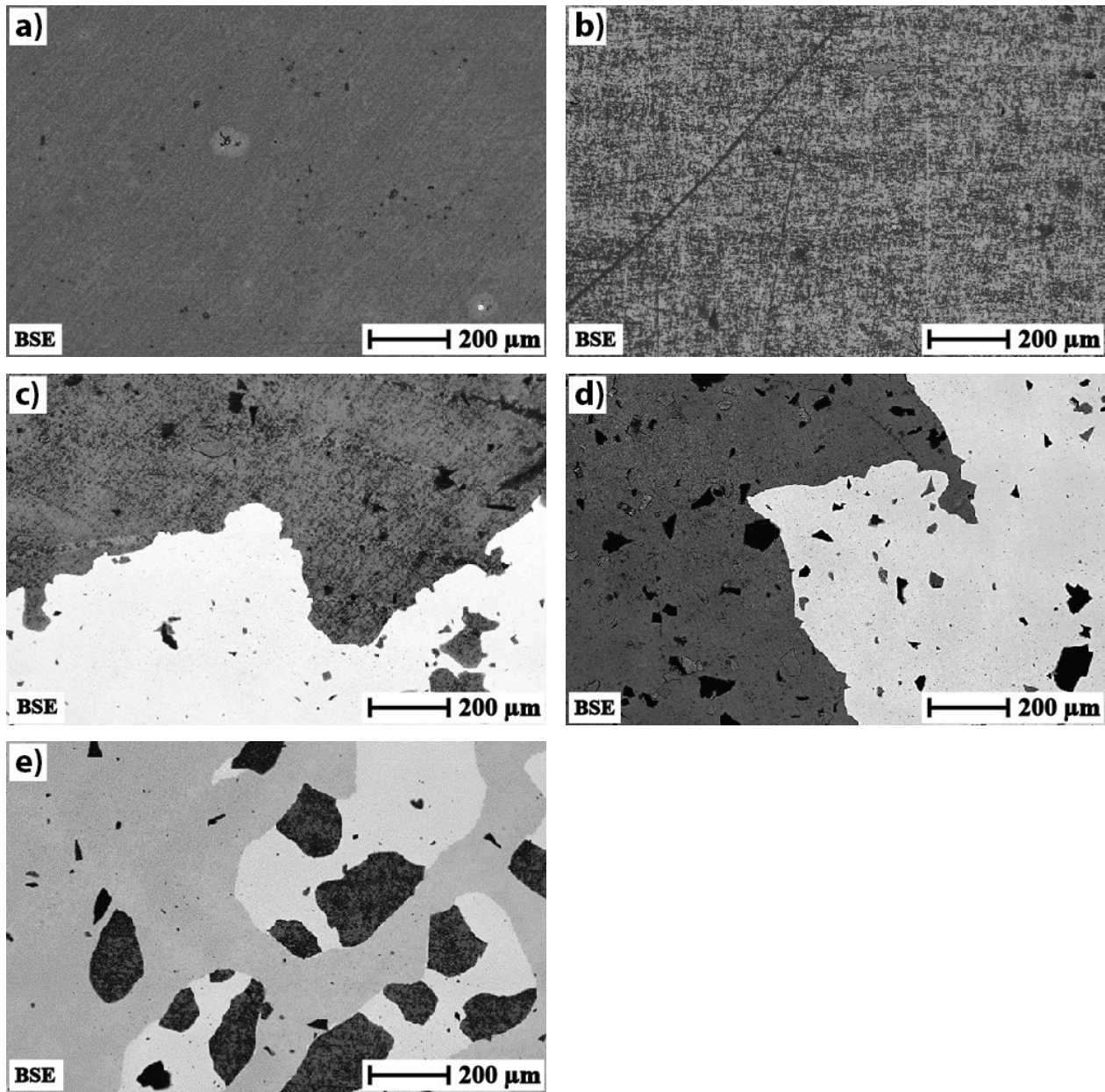


Figure 37: CMSX-4 oxidized at 1150°C for a) 0.5 hrs, b) 1 hr, c) 2 hrs, d) 4 hrs and e) 16 hrs

Figure 38 shows the progression of oxidation on the surface of the sample; where the labels on Figure 38 indicate the region number (1-3) and the letters indicate the heat treatment time (a=0.5 hrs, b=1 hr, c=2 hrs, d=4 hrs and e=16 hrs). Compositions of regions identified in Figure 38 are provided in Table 19. Region 1 is a mixture of aluminum, nickel, cobalt and

chromium oxides. Region 2 is an analysis of the small, relatively lighter-coloured particles precipitating from the oxide identified in Region 1 and is Ta and Ti rich. Region 3 is characterized by high aluminum content.

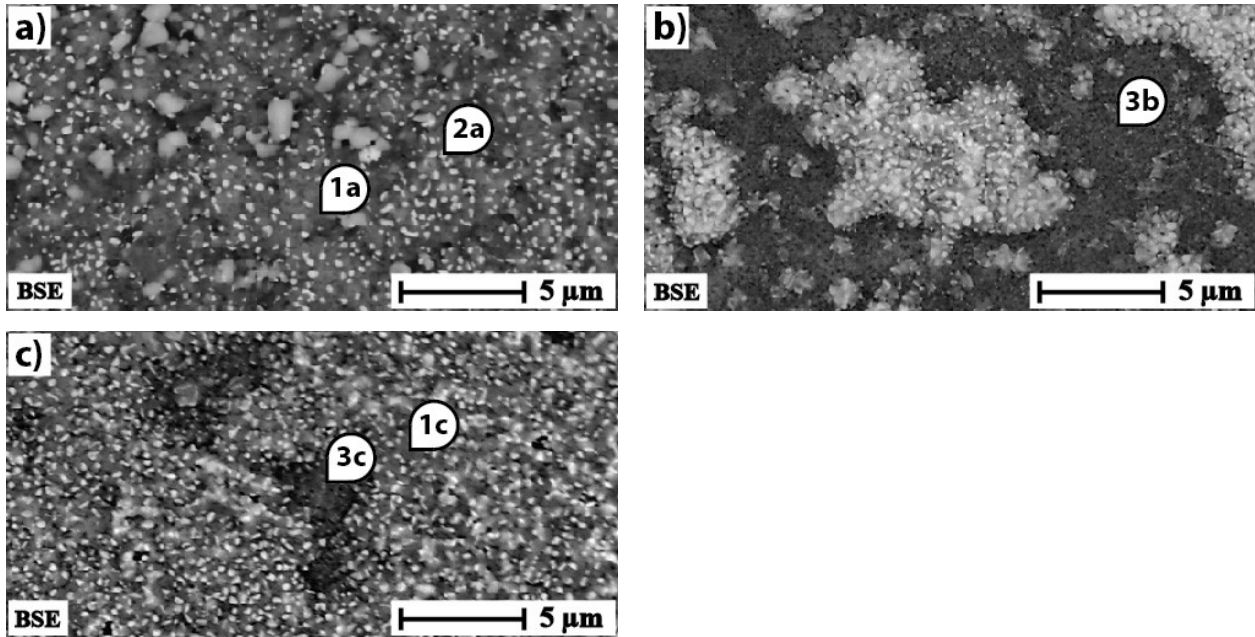


Figure 38: Surface of CMSX-4 oxidized at 1150°C for a) 0.5 hrs b) 1 hr and c) 2 hrs

Table 19: Composition of regions identified in Figure 38

Element	at. %					Element	wt. %				
	1a	1c	2a	3b	3c		1a	1c	2a	3b	3c
Al	20	26.21	17.91	35.73	31.51	Al	17.8	24.34	16.05	38.89	33.65
Co	3.11	2.39	2.87	1.75	1.85	Co	6.05	4.85	5.62	4.16	4.31
Cr	7.21	5.9	6.6	2.12	2.66	Cr	12.37	10.56	11.4	4.45	5.47
Ni	12.74	11.45	11.91	7.84	9.5	Ni	24.67	23.13	23.22	18.56	22.07
O	54.01	52.15	56.99	52.57	54.48	O	28.51	28.72	30.28	33.93	34.5
Ta	1.36	1.15	1.71	-	-	Ta	8.12	7.16	10.28	-	-
Ti	1.58	0.75	1.99	-	-	Ti	2.49	1.24	3.16	-	-

Figure 39 shows the progression of oxidation in cross-section, where the labels on Figure 39 indicate the region number (1, 3 and 4) and the letters indicate the heat treatment time (a=0.5 hrs, b=1 hr, and c=2 hrs). Regions labelled with the same number are believed to

correspond (i.e. Region 1 of Figure 39 corresponds to Region 1 of Figure 38) and justification for these conclusions are provided in the following paragraphs. Compositions corresponding to regions identified in Figure 39 are provided in Table 20.

Region 1 of Figure 39 is predominantly composed of Al, Cr and Ni. Region 4 of Figure 39 has relatively higher Ta concentration than the surrounding regions suggesting that the line of light-coloured oxides identified in Region 4 is composed predominantly of Ta. Other elements detected in Region 4 of Figure 39 are assumed to be detected from the surrounding regions (Regions 1 and 3) due to the 1 μm precision of the EDAX technique. Region 3 has relatively higher Al content than Regions 1 or 2 and is characterized by high Al and Ni with some Co and Cr.

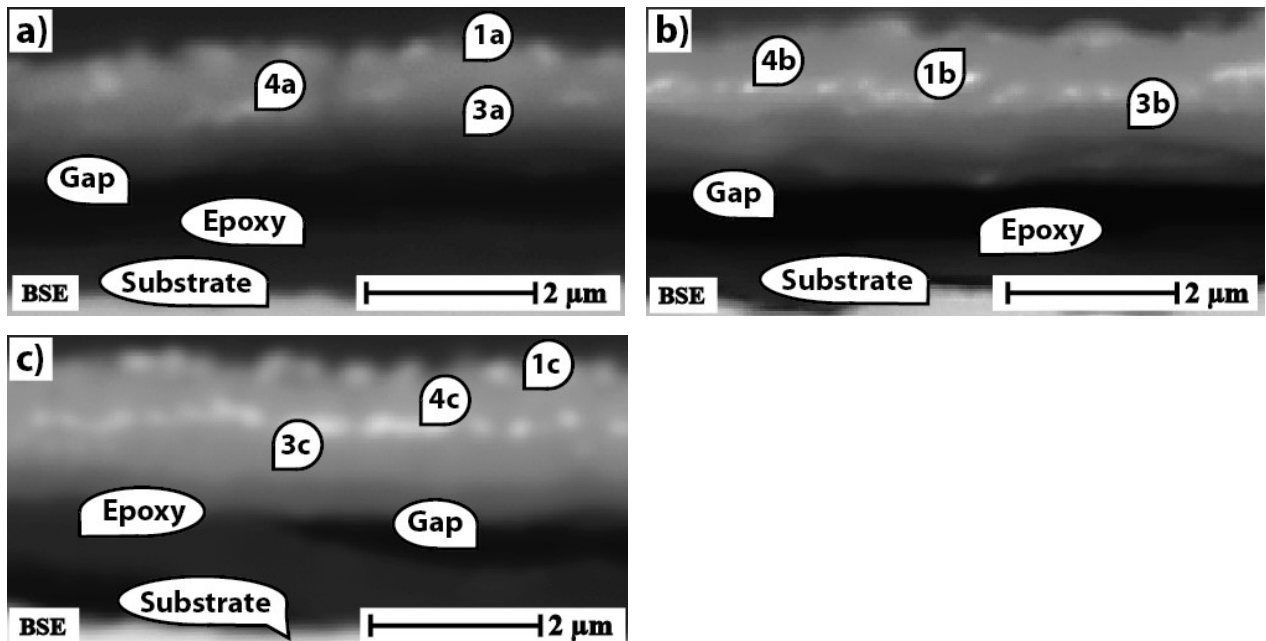


Figure 39: Cross-section of CMSX-4 oxidized at 1150°C for a) 0.5 hrs b) 1 hr and c) 2 hrs

Table 20: Composition of regions identified in Figure 39

	at. %								
Element	1a	1b	1c	3a	3b	3c	4a	4b	4c
Al	24.66	29.44	23.81	37.28	34.3	29.3	28.96	28.09	23.9
Co	4.07	3.75	2.89	3.26	2.21	1.62	3.16	2.59	2.27
Cr	9.26	8.47	7.52	4.01	2.84	2.21	5.63	5.93	5.09
Ni	15.72	14.77	11.68	15.8	11.41	9.34	14.44	12.64	10.86
O	44.57	41.86	52.63	39.65	49.24	57.55	45.43	47.8	56.59
Ta	-	-	-	-	-	-	0.79	1.77	0.64
Ti	1.7	1.72	1.48	-	-	-	1.01	1.18	0.67

	wt. %								
Element	1a	1b	1c	3a	3b	3c	4a	4b	4c
Al	21.44	25.83	22.93	33.89	34.78	32.01	25.82	24.43	23.59
Co	7.73	7.19	6.08	6.47	4.89	3.87	6.15	4.92	4.89
Cr	15.51	14.32	13.95	7.02	5.55	4.65	9.67	9.94	9.68
Ni	29.73	28.19	24.46	31.24	25.17	22.2	28.01	23.91	23.31
O	22.97	21.78	30.05	21.37	29.61	37.28	24.02	24.65	33.12
Ta	-	-	-	-	-	-	4.72	10.32	4.24
Ti	2.62	2.68	2.53	-	-	-	1.6	1.82	1.17

XRD analysis of a sample heat treated for 2 hrs (Figure 40), confirmed that rutile-TiO₂, Ni(Al,Cr)₂O₄, NiO and α-Al₂O₃ are present. Therefore, Region 1 (Figure 38 and Figure 39) which was found to be predominantly composed of Ni, Al and Cr with some Ti is likely Ni(Al,Cr)₂O₄, NiO with some rutile-TiO₂. Similar oxidation studies conducted on CMSX-4 have found NiO and Ti oxides at the scale/gas interface [81]. Region 3 which is predominantly composed of Al is most likely α-Al₂O₃, although high Ni and Cr in this region suggests that there may also be Ni(Al,Cr)₂O₄ present. However, in other work, a layer of Al₂O₃ has been found to develop adjacent to the substrate/scale interface on CMSX-4 following 5-10 hrs of oxidation at 1100°C [81], suggesting that this layer is predominantly α-Al₂O₃. No peaks for oxides of Ta were found (Figure 40). However, in similar oxidation studies conducted on CMSX-4 an intermediate layer

of Cr and Ta oxides were found [81], suggesting that this layer does indeed have high Ta content.

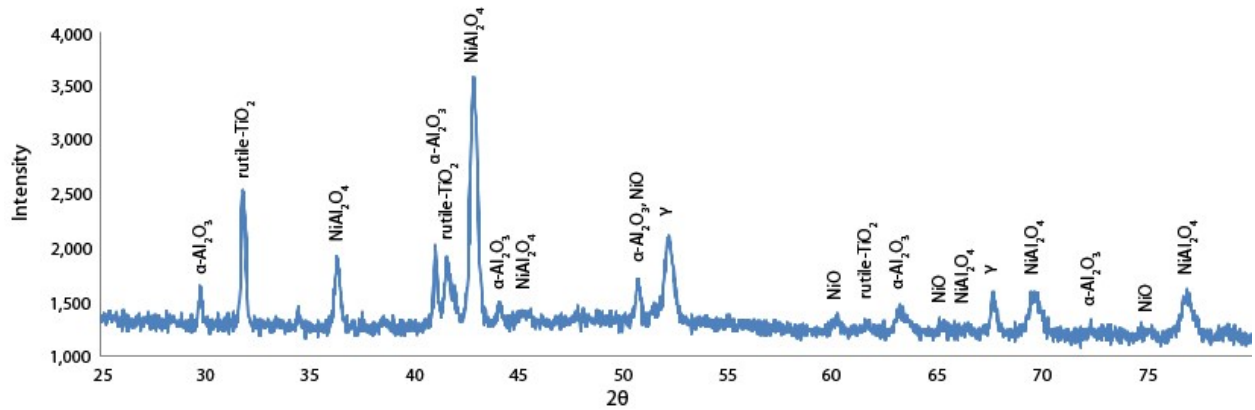


Figure 40: XRD results for CMSX-4 isothermally oxidized at 1150°C for 2 hrs

The average height of “Layer 1” (corresponding to Region 1 of Figure 39) and “Layer 2” (corresponding to Region 3 of Figure 39) are plotted as a function of oxidation time in Figure 41. For each oxidation time, thicknesses were measured at 3 locations along the cross-section. At each location, 3 measurements were taken ($n=9$, $s=0.05\mu\text{m}$).

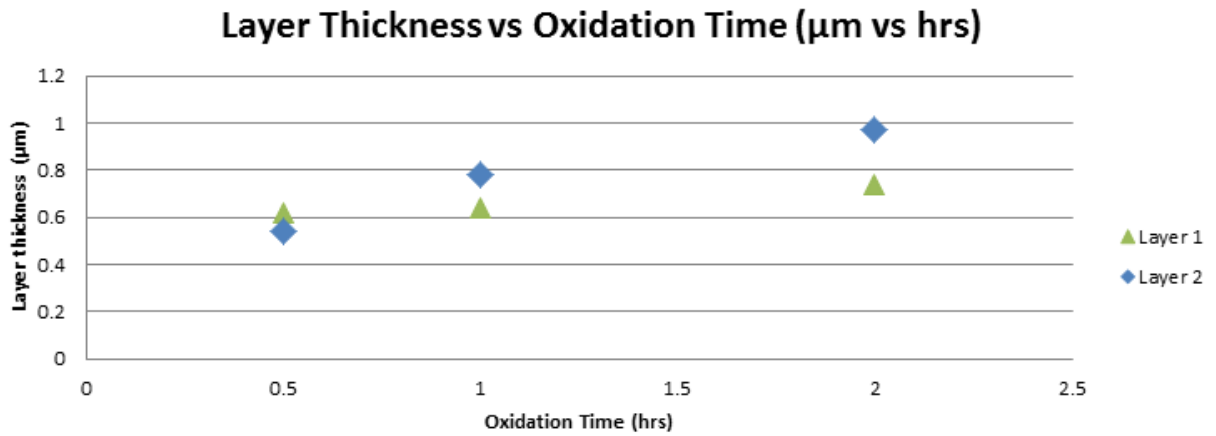


Figure 41: CMSX-4 layer thickness vs oxidation time

Spallation occurs following 4 and 16 hrs of oxidation (Figure 36d-e and Figure 37d-e). Figure 42 shows images of the spalled oxides and exposed on the surfaces of the samples oxidized for 4 and 16 hrs.

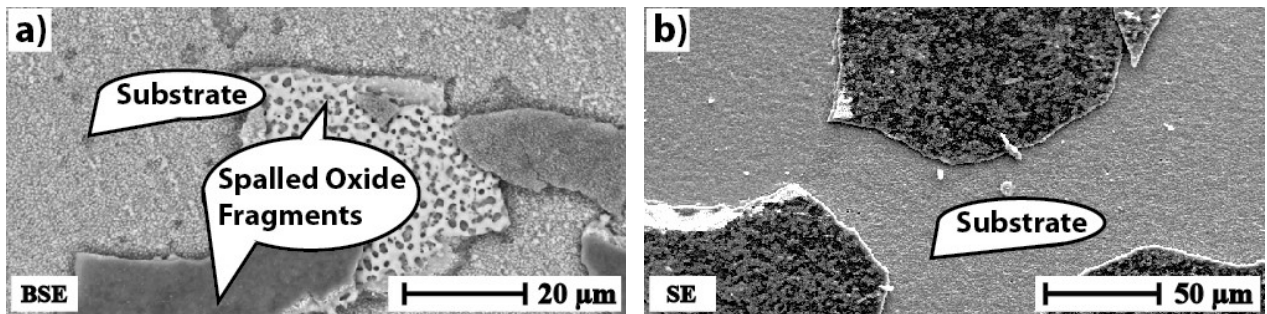


Figure 42: Oxidation of CMSX-4 at 1150°C for showing spallation following a) 4 hrs of oxidation and b) 16 hrs of oxidation

4.2.3 René N5

Images of the samples after heat treatment are provided in Figure 43.

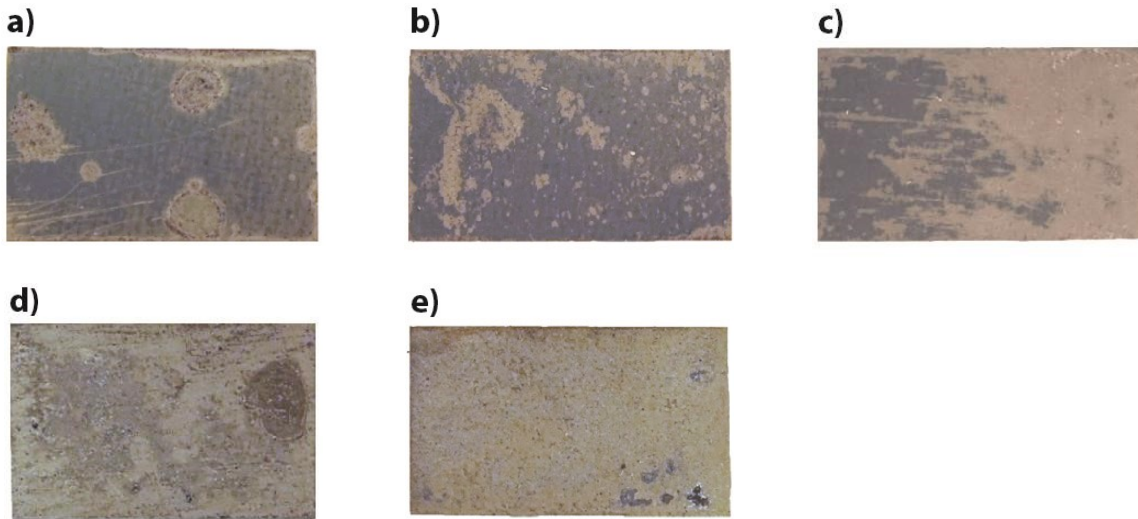


Figure 43: René N5 oxidized at 1150°C for a) 0.5 hrs, b) 1 hr, c) 2 hrs, d) 4 hrs and e) 16 hrs

Images of the sample surface at 0.5, 1, 2, 4 and 16 hrs are provided in Figure 44. Moderate spallation of the relatively dark-coloured oxides begins following 2 hrs of oxidation. The surface of the sample appears to be completely absent of these dark-coloured oxides following 4 hrs of oxidation (Figure 43d). The appearance of sample surface after 16 hrs (Figure 43e) of oxidation is similar to that of the sample oxidized for 4h (Figure 43d) and upon closer observation moderate and gross spallation can be observed on the 4 hrs and 16 hrs samples, respectively (Figure 44d and Figure 44e).

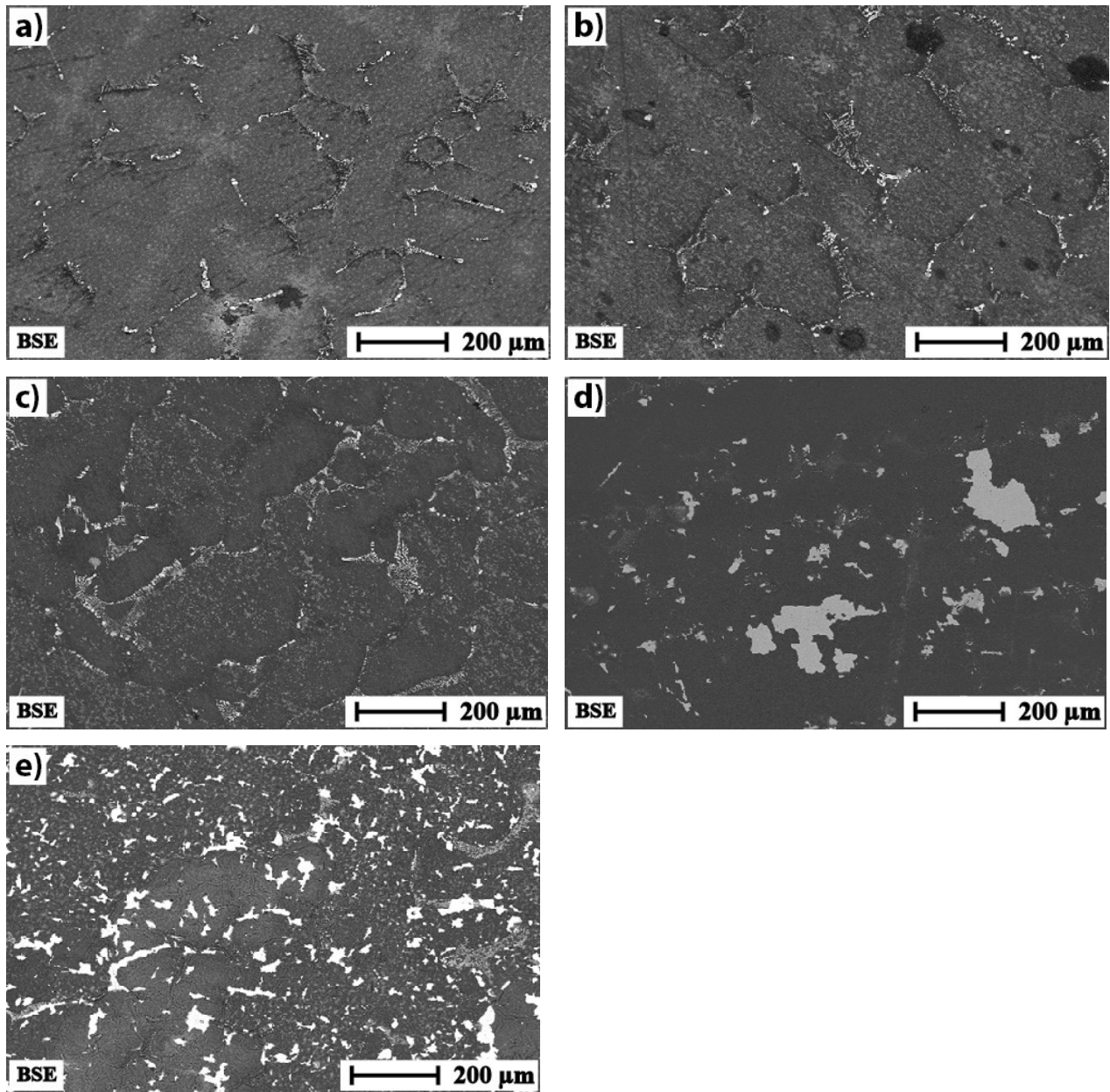


Figure 44: René N5 oxidized at 1150°C for a) 0.5 hrs, b) 1 hr, c) 2 hrs, d) 4 hrs and e) 16 hrs

Oxidation corresponds to the compositionally different regions found on the untreated substrate (Figure 28). Oxidation of the eutectic regions prior to the onset of spallation (0.5, 1

and 2 hrs) are provided in Figure 45 with compositions of the areas identified in the figure listed in Table 21.

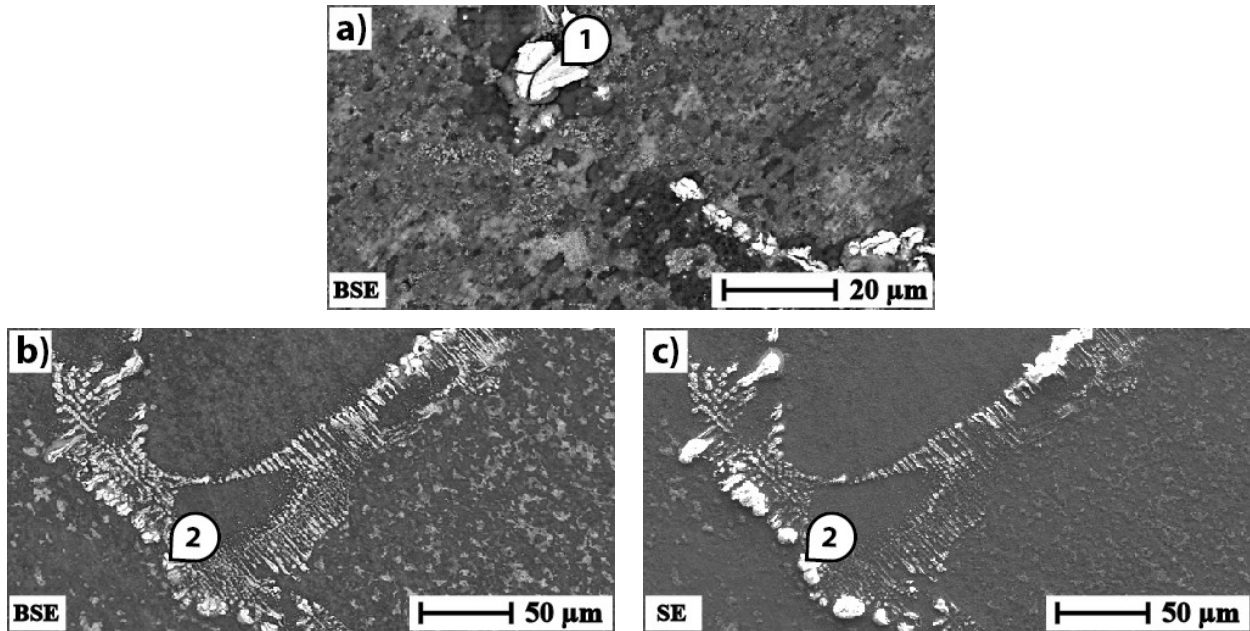


Figure 45: Oxidation of René N5 at 1150°C. a) Hf and Ta rich oxides in a eutectic region after 0.5 hrs of oxidation, b) a eutectic region oxidized for 2 hrs and c) a eutectic region oxidized for 2 hrs

Table 21: Composition of regions identified in Figure 45

Element	at. %		Element	wt. %	
	1	2		1	2
Al	9.4	11.53	Al	2.5	2.58
Co	3.39	2.1	Co	1.97	1.03
Cr	5.44	8.17	Cr	2.79	3.53
Hf	10.08	-	Hf	5.84	0
Ni	13.84	10.99	Ni	2.19	1.46
O	43.64	58.58	O	77.99	87.98
Ta	14.2	8.62	Ta	6.71	3.42

The eutectic regions (Figure 45a, Figure 45b and Figure 45c) are covered predominantly with oxides of Ta; however there are localized regions of high Hf content. The oxidized eutectic regions impart a somewhat uneven surface morphology (Figure 45c), although it is less-pronounced following 2 hrs of oxidation than following 0.5 or 1 hr of oxidation. The Hf oxides

tend to form deep pegs whereas the Ta oxides form shallow pegs as well as regions of internal oxidation (Figure 46a and Figure 46b). Compositions of the regions identified in Figure 46 are provided in Table 22. Both Ta and Hf pegs are surrounded by Al-rich oxides (Region 3, Figure 46a and Region 6, Figure 46b). Although Figure 46 provides images of pegs following 4 and 16 hrs of oxidation, pegs were present at all oxidation times.

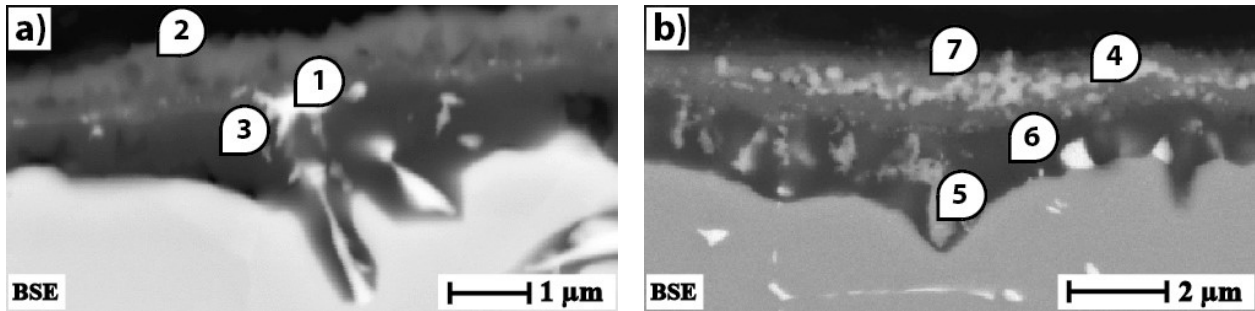


Figure 46: Oxidation of René N5 at 1150°C. a) Hafnium-rich oxide peg after 4 hrs of oxidation and b) Oxidation of the eutectic region after 16 hrs

Table 22: Composition of regions identified in Figure 46

	at. %						
	1	2	3	4	5	6	7
Al	32.98	32.91	40.51	17.34	28.68	35.95	18.56
Co	-	1.91	0.5	1.04	1.37	0.39	0.94
Cr	1.5	4.09	0.79	2.67	1.64	0.6	1.81
Hf	4.49	-	-	-	-	-	-
Ni	2.37	10.26	2.29	6.36	6.86	2.29	6.38
O	58.65	50.82	55.9	68.05	55.56	60.11	70
Ta	-	-	-	4.54	5.89	0.66	2.31

	wt. %						
	1	2	3	4	5	6	7
Al	31.26	33.78	49.86	15.85	23.47	43.31	19.54
Co	-	4.28	1.34	2.08	2.45	1.03	2.16
Cr	2.74	8.09	1.87	4.7	2.59	1.39	3.67
Hf	28.15	-	-	-	-	-	-
Ni	4.89	22.91	6.13	12.65	12.21	6	14.61
O	32.96	30.93	40.8	36.89	26.96	42.94	43.7
Ta	-	-	-	27.83	32.32	5.33	16.31

The majority of the surface is not covered by eutectic regions. In the interdendritic region immediately adjacent to the eutectic region, oxides of predominantly Al form (Figure 47a, Region 2). Aside from these regions, the majority of the interdendritic and dendritic regions oxidize in a similar manner, as is illustrated in Figure 47 and further discussed in Figure 48. Compositions of regions identified in Figure 47 are provided in Table 23.

After 0.5 hrs of oxidation the majority of the surface is covered by a mixture of Al, Ni, Cr and Co rich oxides with trace amounts of Ta (Figure 47b). Further oxidation of these regions leads to an increase in the Aluminum concentration (Figure 47c and Figure 47d). The morphology of these regions after 2 hrs (Figure 47d) is relatively uniform in comparison to the morphology of the eutectic regions after 2 hrs (Figure 45d).

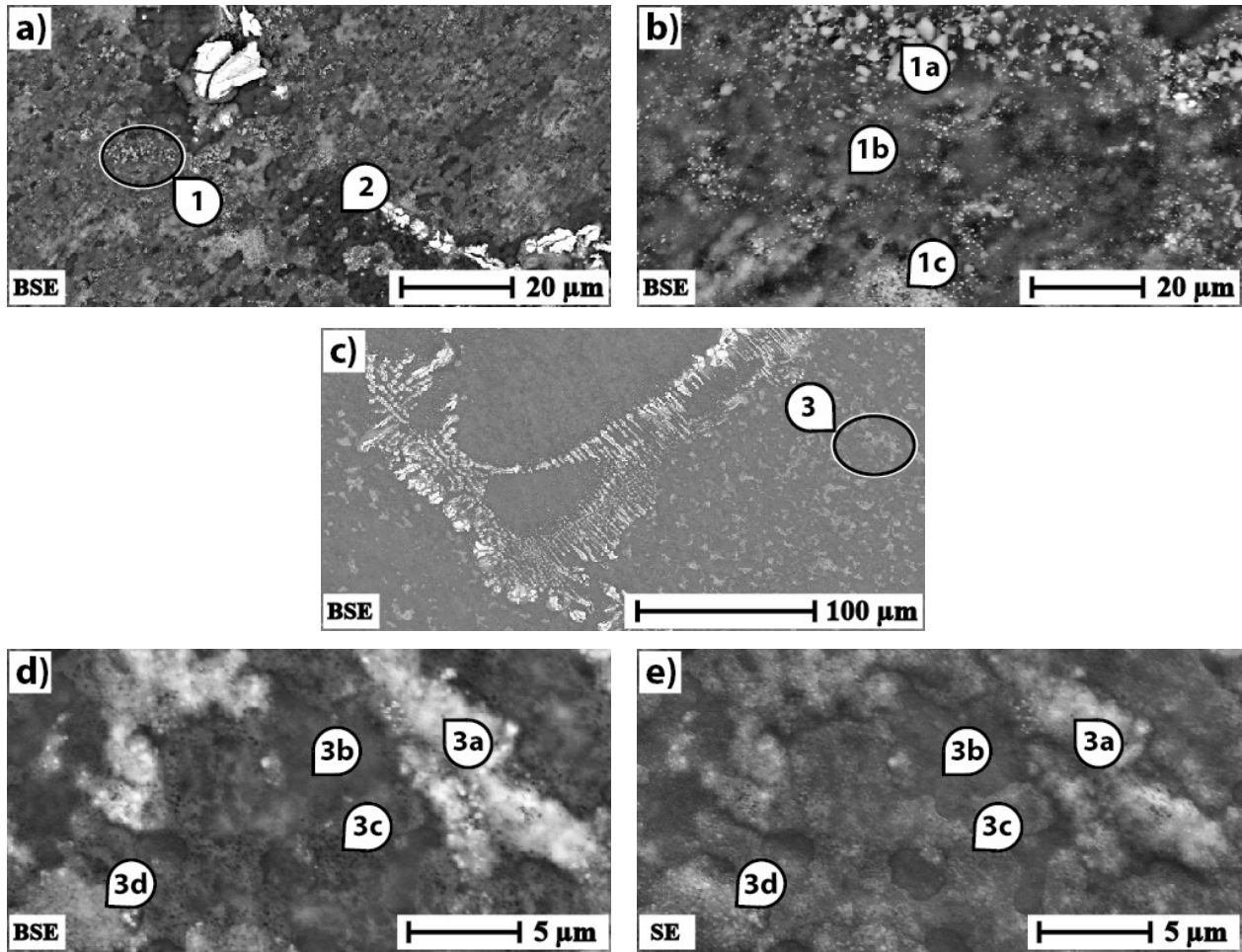


Figure 47: Oxidation of dendritic and interdendritic regions of René N5. a) after 0.5 hrs, b) Nickel, Aluminum, Cobalt and Chromium rich oxides with trace amounts of Tantalum formed after 0.5 hrs, c) Aluminum and Nickel rich oxides formed after 2 hrs, d) morphology after 2 hrs

Table 23: Composition of regions identified in Figure 47

Element	at. %							
	1a	1b	1c	2	3a	3b	3c	3d
Al	18.64	27.1	21.1	31.42	25.77	34.95	35.16	30.16
Co	1.46	1.97	2.22	1.88	1.85	1.74	1.46	1.61
Cr	3.53	6.04	7.05	3.02	6.01	2.76	2.35	4.34
Ni	21.4	11.84	12.67	13.29	9.1	11.82	9.44	8.32
O	54.73	52.61	55.32	49.81	56.08	48.73	51.29	55.06
Ta	0.24	0.43	1.62	0.58	1.19	-	0.31	0.49

Element	wt. %							
	1a	1b	1c	2	3a	3b	3c	3d
Al	17.06	26.34	19.05	30.3	25.16	35.42	36.66	31.39
Co	2.92	4.18	4.38	3.96	3.95	3.85	3.33	3.66
Cr	6.23	11.31	12.27	5.61	11.31	5.39	4.72	8.71
Ni	42.61	25.04	24.88	27.88	19.33	26.06	21.41	18.84
O	29.71	30.32	29.62	28.49	32.47	29.28	31.71	33.98
Ta	1.47	2.8	9.81	3.75	7.79	-	2.17	3.42

In cross-section, these regions appear quite uniform exhibiting a characteristic bi-layered structure (Figure 48). Average compositions of the regions identified in Figure 48 are provided in Table 24. Region 2 is characterized by relatively higher Al content. Region 1 is characterized by high Al and Ni content with some Cr and Co. Region 3 has a relatively higher Ta content in comparison to the surrounding regions suggesting that the light-coloured particles identified in Region 3 are oxides of Ta.

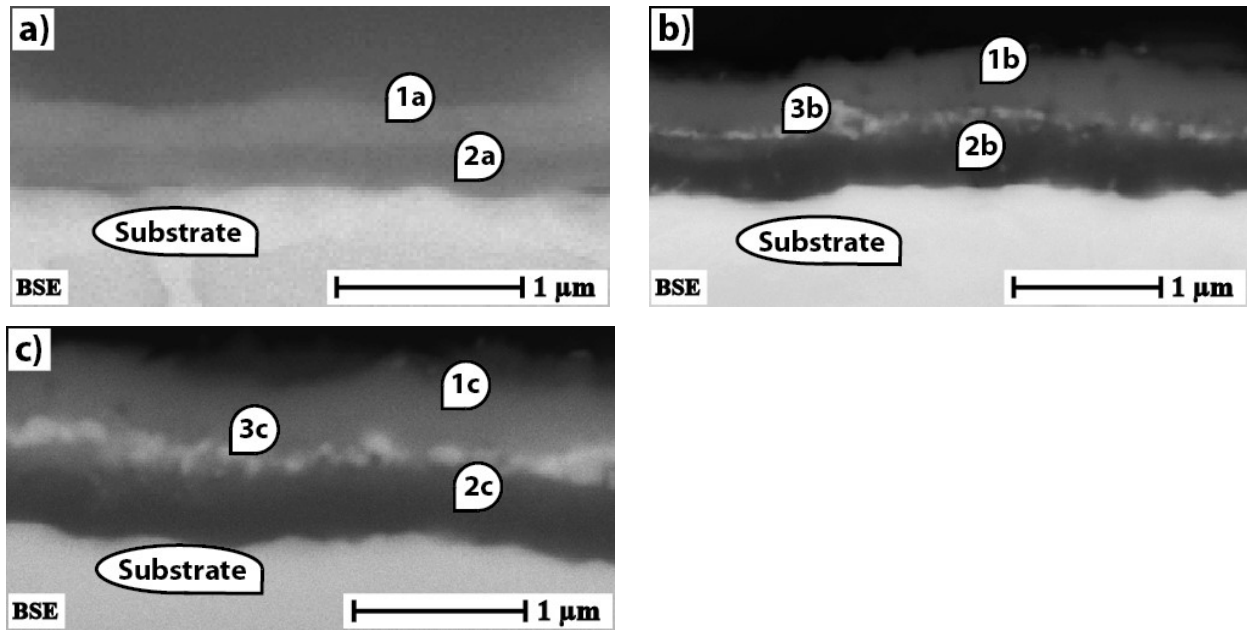


Figure 48: Cross-section of René N5 oxidized at 1150°C for a) 0.5 hrs b) 1 hr and c) 2 hrs

Table 24: Composition of regions identified in Figure 48

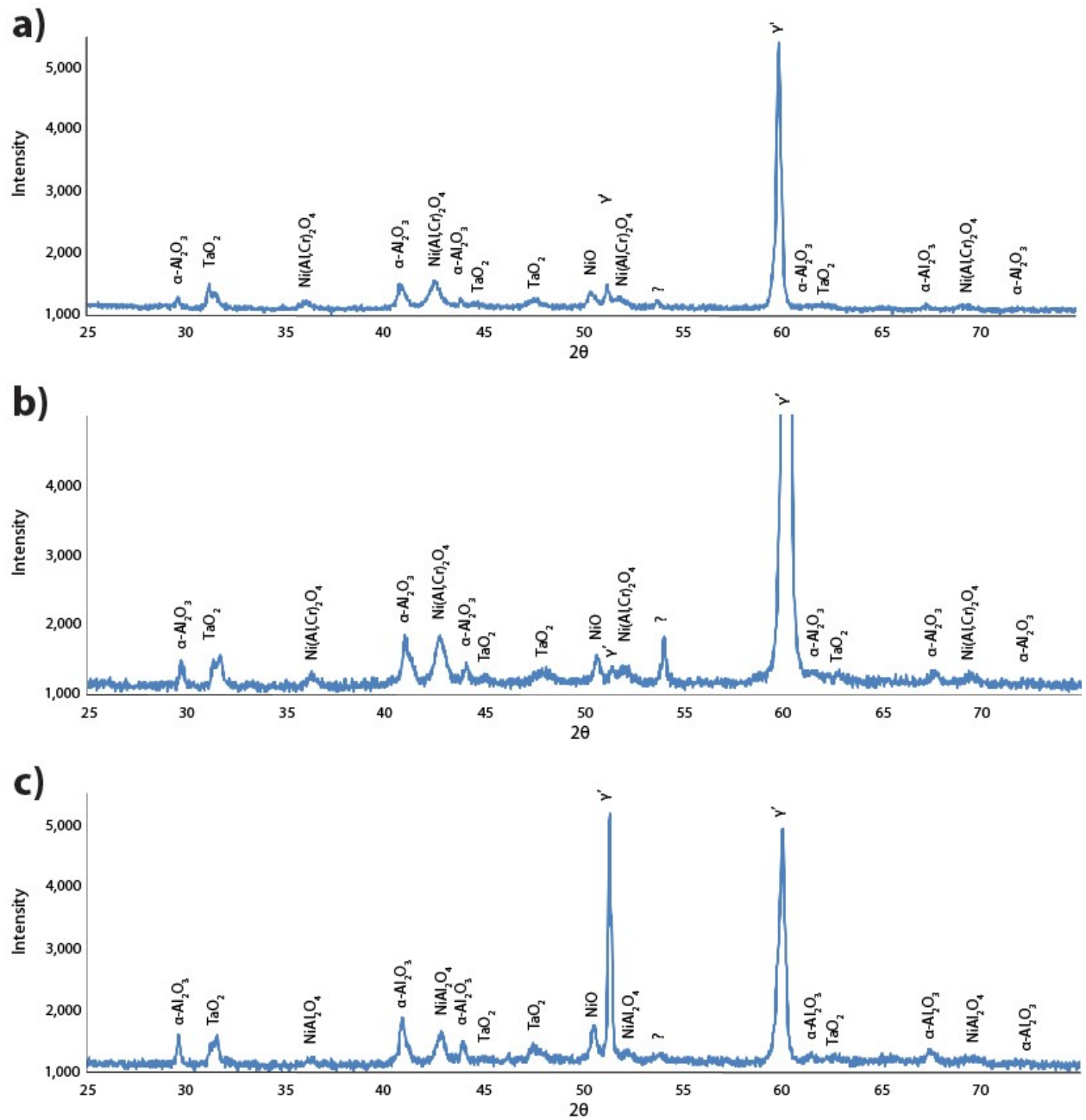
Element	at. %							
	1a	1b	1c	2a	2b	2c	3b	3c
Al	25.02	27.93	24.24	27.11	35.53	28.77	27.42	21.08
Co	3.12	1.41	1.12	2.92	1.31	1.13	1.32	1.17
Cr	3.72	5.77	2.71	3.6	2.47	2.13	4.95	3.36
Ni	25.52	8.49	7.04	24.04	8.71	7.37	8.56	6.76
O	42.62	56.4	64.51	42.34	51.55	60.2	56.48	66.1
Ta	-	-	0.38	-	0.43	0.41	1.27	1.53

Element	wt. %							
	1a	1b	1c	2a	2b	2c	3b	3c
Al	20.89	29.7	27.54	23.01	37.18	32.03	27.29	22.36
Co	5.69	3.27	2.78	5.41	2.99	2.75	2.87	2.71
Cr	5.98	11.82	5.93	5.89	4.98	4.57	9.49	6.87
Ni	46.34	19.64	17.4	44.38	19.83	17.85	18.53	15.6
O	21.1	35.56	43.46	21.31	31.99	39.74	33.33	41.58
Ta	-	-	2.9	-	3.02	3.06	8.48	10.88

XRD analysis was conducted on samples for all heat treatment times (Figure 49). The results show peaks for α -Al₂O₃ following 0.5, 1 and 2 hrs of oxidation with peaks increasing slightly in intensity for each oxidation time. This suggests that Region 2 of Figure 48 is

composed predominantly of α -Al₂O₃. René N5 has been found to develop an α -Al₂O₃ scale following high temperature (~1000°C) oxidation [82, 83, 84].

Peaks for TaO₂ and Ni(Al,Cr)₂O₄, both which have been found in oxidation studies on René N5 at 980°C [82], were detected. Therefore, the Ta-rich eutectic regions are most likely predominantly composed of TaO₂ (Figure 45, Regions 1 and 2) and Region 1 of Figure 48 is composed of Ni(Al,Cr)₂O₄ following up to 2 hrs of oxidation.



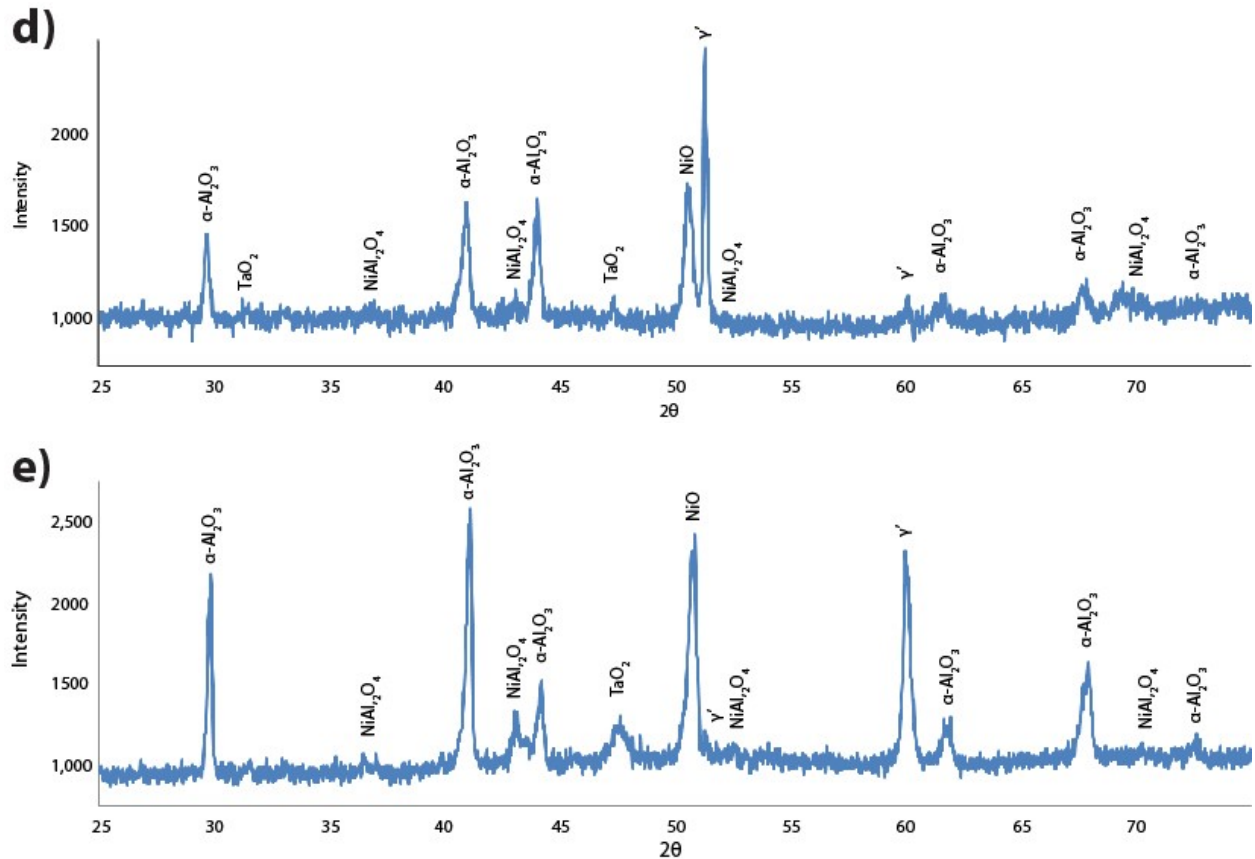


Figure 49: XRD results for René N5 isothermally oxidized at 1150°C for a) 0.5 hrs, b) 1 hr, c) 2 hrs, d) 4 hrs and e) 16 hrs

The average thicknesses of “Layer 1” (corresponding to Region 1 of Figure 48) and “Layer 2” (corresponding to Region 2 of Figure 48) are plotted as a function of oxidation time in Figure 50. For each oxidation time, thicknesses were measured at 3 locations along the cross-section. At each location, 3 measurements were taken ($n=9$, $s=0.02\mu\text{m}$).

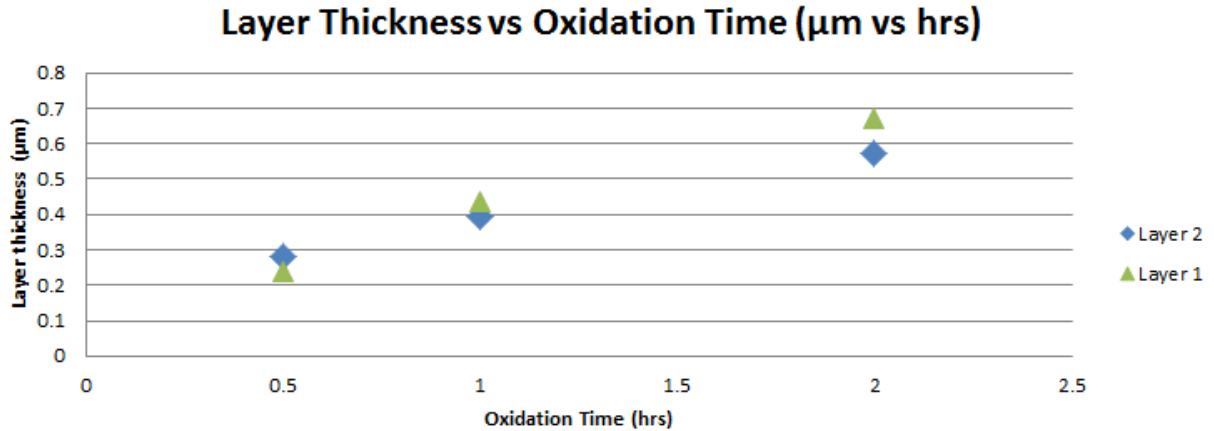


Figure 50: René N5 layer thickness vs oxidation time

After 4 hrs of oxidation, noticeable spallation begins (Figure 44d). Ridges form in the interdendritic regions (Figure 51a). These ridges crack and spall (Figure 51b). The composition on either side of these interfaces is quite similar (Figure 51b); however, the eutectic region is slightly richer in tantalum (Figure 51b, Region 1). The ridges upon which the cracks form (Figure 51b, Region 3) are similar in composition to the adjacent regions. All regions have relatively high aluminum content, suggesting the presence of Al_2O_3 . XRD results did confirm the presence $\alpha\text{-Al}_2\text{O}_3$ for all oxidation times with increasing intensity following 4 and 16 hrs of oxidation (Figure 49). XRD results indicate that NiO is present, suggesting that newly exposed regions of substrate have oxidized to produce oxides of predominantly Ni. NiO has been detected in other CMSX-4 oxidation studies at 980°C [83].

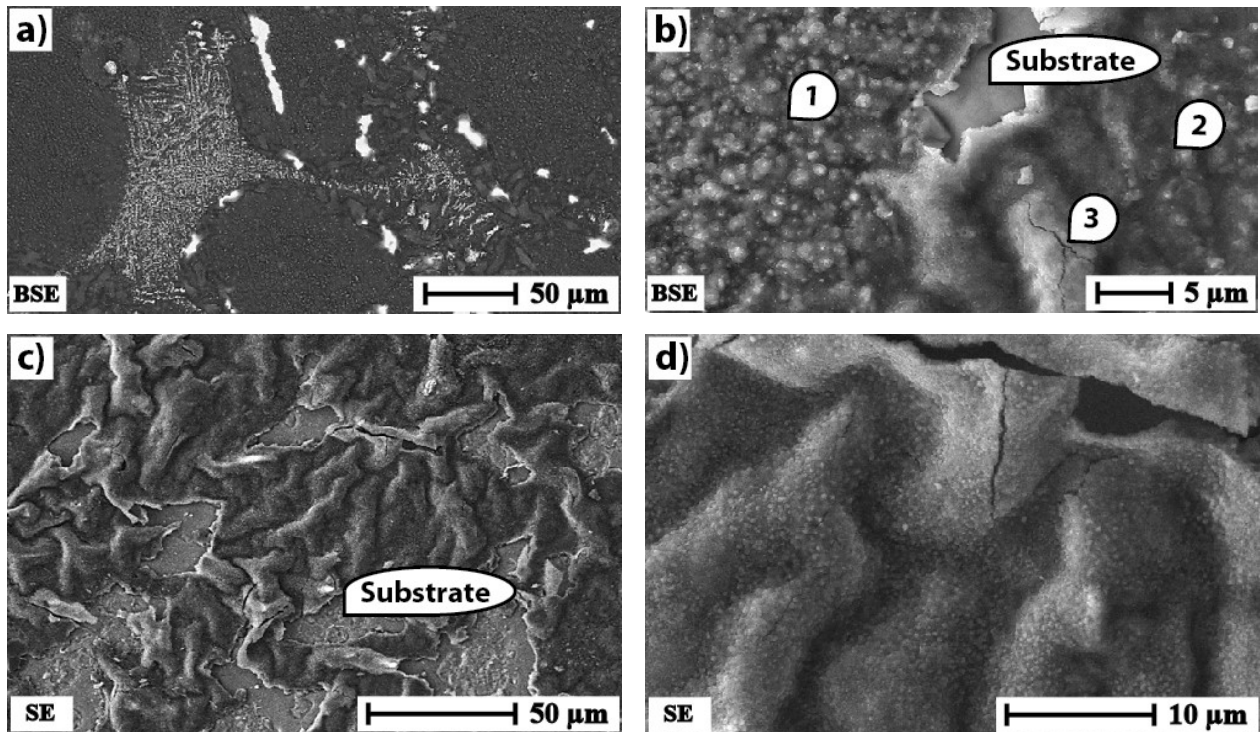


Figure 51: Oxidation of René N5 at 1150°C. a) Spallation adjacent to eutectic regions following 4 hrs of oxidation and b) Interface between eutectic and interdendritic region with cracked ridges following 4 hrs of oxidation c) Ridged morphology and gross spallation following 16 hrs of oxidation and d) ridge morphology following 16 hrs of oxidation

Table 25: Composition of regions identified in Figure 51

Element	at. %		
	1	2	3
Al	37.44	38.65	37.72
Co	0.84	1.05	0.88
Cr	1.83	2.18	2.03
Ni	3.67	6.73	5.46
O	54.28	51.38	53.91
Ta	1.95	-	-

Element	wt. %		
	1	2	3
Al	38.98	42.82	43.16
Co	1.91	2.54	2.2
Cr	3.67	4.65	4.48
Ni	8.31	16.22	13.59
O	33.51	33.76	36.58
Ta	13.62	-	-

After 16 hrs of oxidation, a network of ridges similar to those initially formed in the interdendritic regions following 4 hrs of oxidation cover the surface and there is a significant amount of spallation (Figure 51c and Figure 51d).

4.3 Oxidation Results of Coated René N5

All DVC and Columnar samples failed during the first set of 25 cycles (Section 3.3.3), where failure is defined as 100% spallation of the top coat. As all samples failed during the first 25 cycles, shorter cycles (Section 3.3.3.2) and isothermal hold times (Section 3.3.3.3) were chosen in anticipation that samples would endure the predetermined cycles or hold time without spalling. In spite of this, many samples failed and the shorter cycles or holding times produced samples with very little variation so the impact of holding time and number of cycles was not evident. As such, the impact of the number of cycles and isothermal holding time are not discussed. Instead, the general appearance of both failed samples and samples for which the top coat remained adhered are presented in order to gain insight into the mechanisms which may have led to poor adhesion.

4.3.1 René N5 SPS DVC

Two of the three samples failed during cyclic testing after 3 and 6 cycles (Section 3.3.3.2), while the third remained intact following 6 cycles. Top coats appeared to remain intact on samples following 4, 6 and 10 hrs of isothermal oxidation (Section 3.3.3.3); however, all of these samples were found to be completely delaminated when viewed at higher magnifications in cross-section.

Images of a sample which failed during cyclic testing are provided in Figure 52. These images show the oxidized surface of the exposed substrate following spallation of the top coat. Compositions of marked microstructure constituents in Figure 52 are provided in Table 26.

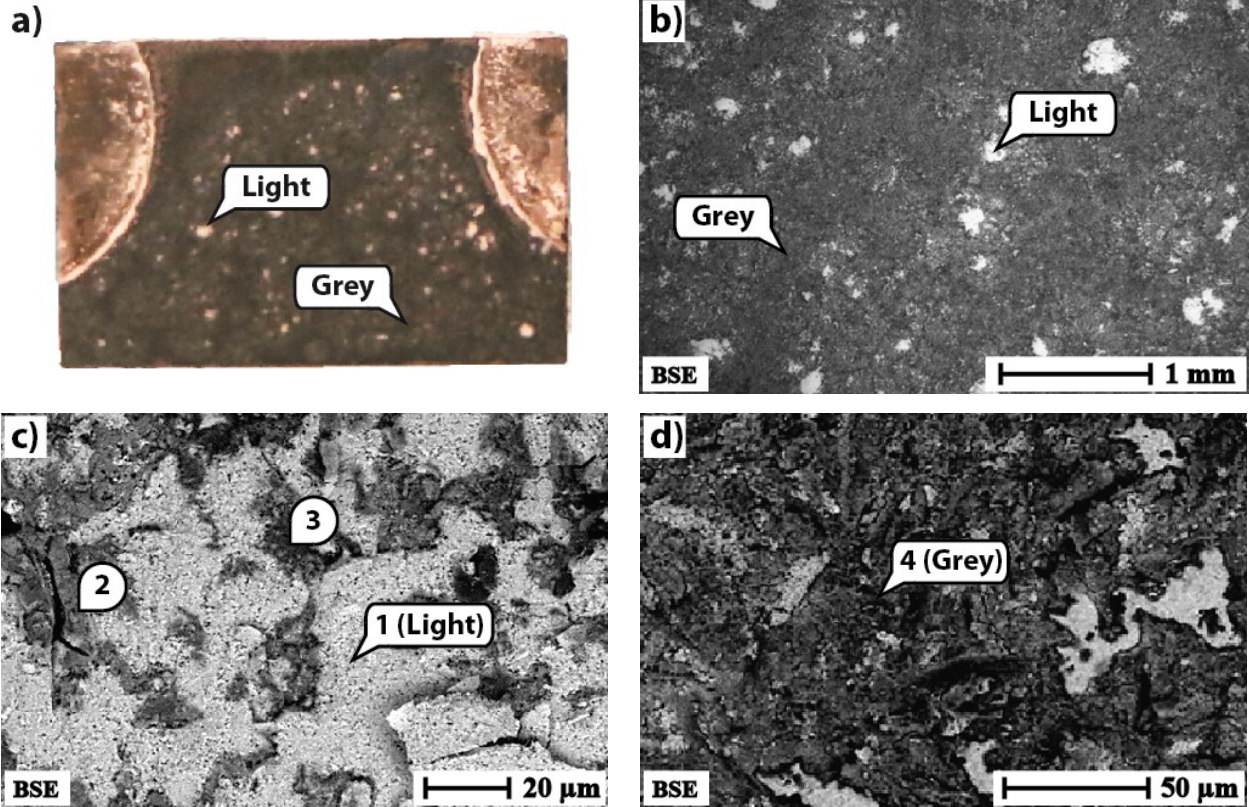


Figure 52: Exposed substrate of DVC coated René N5 sample. a) photograph of sample, b) overall appearance, c) light region, d) grey region

Table 26: Composition of regions identified in Figure 52

Element	at. %			
	1	2	3	4
Al	6.41	13.23	19.67	19.08
Co	0.59	1.93	1.09	1.56
Cr	1.43	7.82	2.52	4.45
Ni	3.7	8.18	8	9.05
O	68.44	64.08	64.86	64.25
Ta	-	0.25	0.23	0.4
Y	1.89	0.56	0.49	0.21
Zr	17.71	3.95	3.13	1.03

Element	wt. %			
	1	2	3	4
Al	5.12	12.58	20.38	19.94
Co	1.03	4.01	2.47	3.56
Cr	2.2	14.33	5.03	8.96
Ni	6.43	16.92	18.03	20.57
O	32.42	36.13	39.85	39.81
Ta	-	1.59	1.6	2.8
Y	4.97	1.75	1.67	0.72
Zr	47.83	12.7	10.97	3.64

The light regions (labeled “Light”) are fragments of top coat which remained adhered to the substrate following top coat spallation (Figure 52c, Region 1). These regions are surrounded by oxides which are slightly darker in appearance and contain phases rich in Al, Cr

and Ni (Figure 52c, Region 2 and 3). Even darker regions of the substrate (labelled “Grey”) are characterized by oxides of high Al, Cr and Ni content (Figure 52d, Region 4).

Images of the backside of the spalled top coat are provided in Figure 53. Compositions of microstructural features in Figure 53 are provided in Table 27.

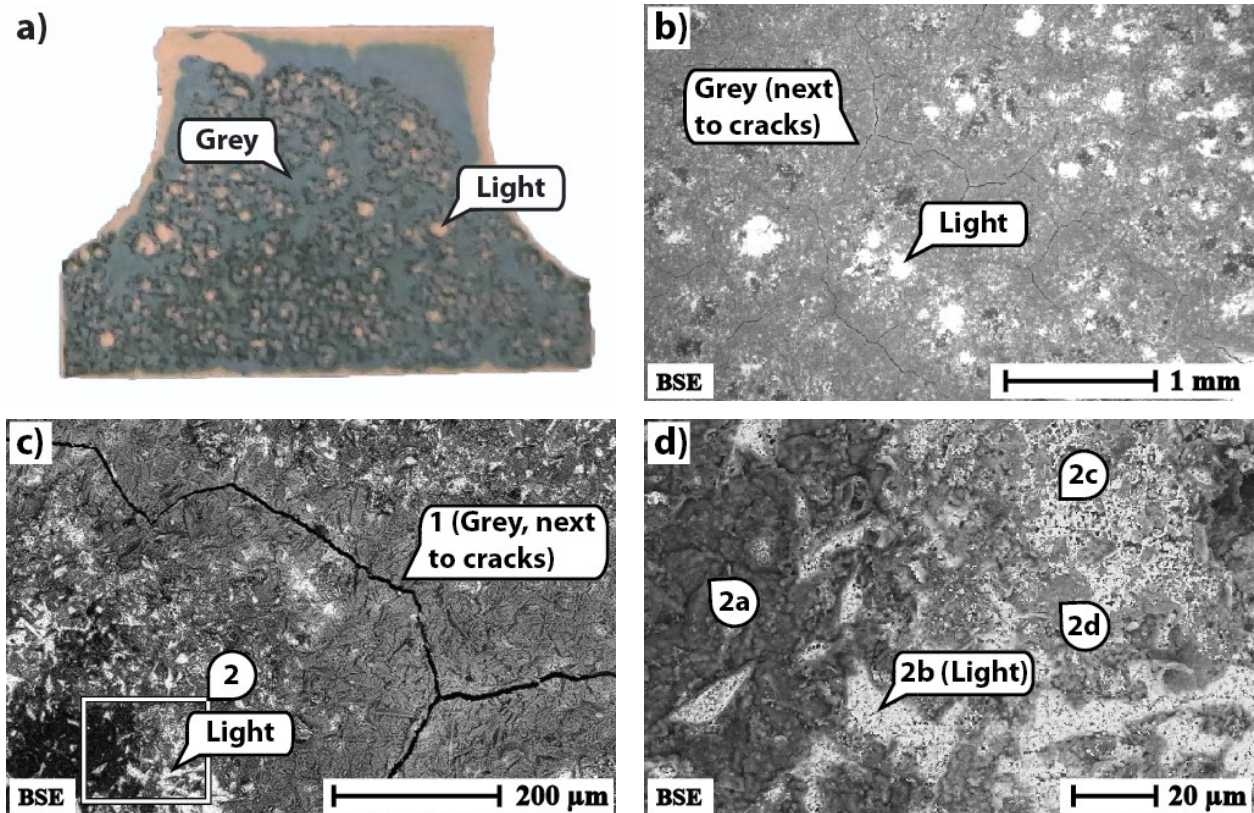


Figure 53: Backside of spalled top coat of DVC coated René N5 sample. a) photograph of sample, b) overall appearance, c) cracks, grey and light region and d) light region and oxides surrounding light region

Table 27: Composition of regions identified in Figure 53

	at. %				
Element	1	2a	2b	2c	2d
Al	10.11	20.62	9.35	11.6	12.96
Co	0.96	0.78	0.61	1.27	1.46
Cr	3.45	1.73	1.78	5.99	3.89
Ni	5.11	4.02	3.38	7.18	6.81
O	72.56	68.69	71.95	66.82	70.37
Ta	-	-	-	2.87	0.38
Zr	7.8	4.17	12.93	4.27	4.12

	wt. %				
Element	1	2a	2b	2c	2d
Al	10.17	23.11	8.67	10.1	13.41
Co	2.11	1.91	1.24	2.42	3.3
Cr	6.69	3.74	3.18	10.05	7.76
Ni	11.19	9.8	6.82	13.6	15.32
O	43.3	45.65	39.56	34.5	43.17
Ta	-	-	-	16.76	2.64
Zr	26.54	15.8	40.54	12.57	14.41

The regions adjacent to the cracks found in the top coat (labelled “Grey”) are characterized by high Al, Cr and Ni content (Figure 53b). Light regions (labelled “Light”) can be found on the sample and have high Zr content (Figure 53d, Region 2b). Surrounding the “Light” regions are oxides of high Ta content (Figure 53d, Region 2c), regions characterized by high Al, Cr and Ni content (Figure 53d, Region 2b) and regions of relatively high Al content (Figure 53a, Region 2a).

Any samples which did not show massive spallation after isothermal or cyclic oxidation had a visible gap between the top coat and the substrate (Figure 54) and when observed in cross-section, the substrate and coating were found to no longer be affixed to one another (Figure 55a).

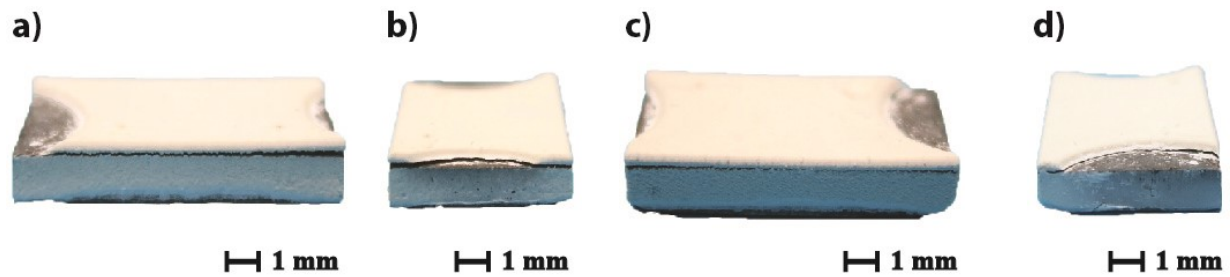


Figure 54: DVC coated René N5 following 6 cycles. a) front, b) right c) back and d) left

Figure 55a is an image of the top coat following 6 cycles. The cracks in the top coat are similar in frequency and severity to those seen in the as-received sample (Figure 29a and Figure 29d). Coated samples were heat treated isothermally for 2 hrs at 1150°C prior to top coat deposition. Figure 55b is an image of the TGO, which is quite irregular and does not resemble the structure of the René N5 samples oxidized for 2 hrs at 1150°C (Figure 48b).

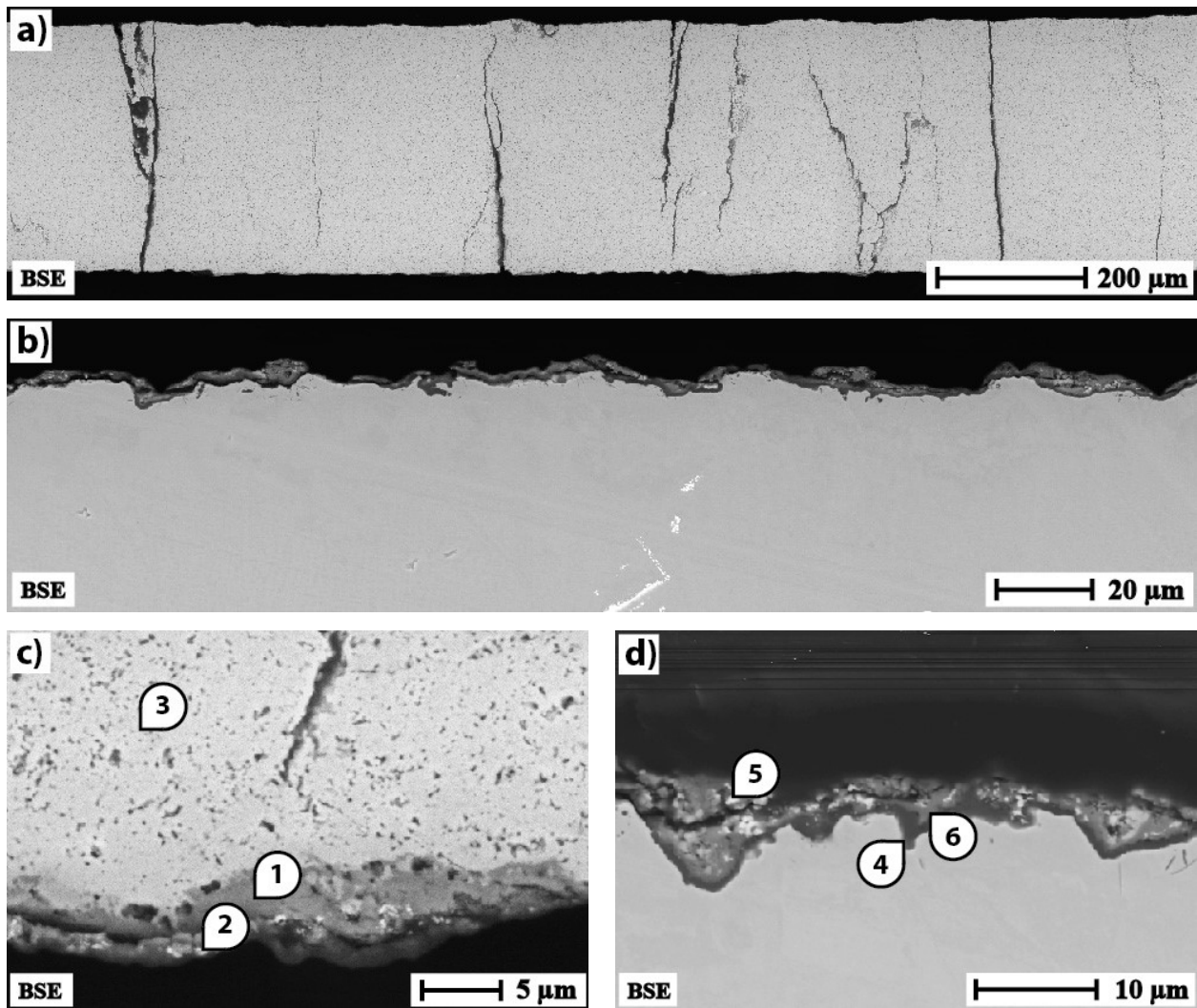


Figure 55: DVC coated René N5 sample following 6 cycles. a) general appearance of top coat, b) general appearance of TGO, c) top coat, d) substrate and e) substrate

Table 28: Composition of regions identified in Figure 55

Element	at. %					
	1	2	3	4	5	6
Al	2.6	5.64	1.09	21.62	8.83	9.36
Co	1.33	0.89	0.71	0.99	1.31	1.52
Cr	7.97	3.71	0.56	1.27	4.33	6.81
Ni	4.48	4.57	3.87	7.29	9.8	11.47
O	80.41	82.69	70.77	68.83	71.9	70.84
Ta	-	-	-	-	3.85	-
Y	-	-	1.77	-	-	-
Zr	3.2	2.51	21.24	-	-	-

Element	wt. %					
	1	2	3	4	5	6
Al	2.92	6.86	0.83	26.08	8.04	10.09
Co	3.26	2.37	1.18	2.61	2.61	3.58
Cr	17.24	8.7	0.82	2.95	7.6	14.15
Ni	10.94	12.09	6.39	19.13	19.41	26.9
O	53.51	59.66	31.85	49.23	38.83	45.28
Ta	-	-	-	-	23.51	-
Y	-	-	4.43	-	-	-
Zr	12.14	10.32	54.51	-	-	-

Compositions corresponding to the regions identified in Figure 55 are provided in Table 28. An image of the top coat at higher magnification is provided in Figure 55c. Oxides of high Al, Cr and Ni content affixed to the top coat (Figure 55c, Regions 1 and 2). Ni was found in the top coat approximately 10 μm from the top coat/substrate interface (Figure 55c, Region 3).

An Image of the substrate at higher magnification is provided in Figure 55d. On the substrate, regions characterized by relatively high Al content (Figure 55d, Region 7), a substantial proportion of Ta (Figure 55d, Region 8) and high Al, Cr and Ni content (Figure 55. Region 9) were identified.

4.3.2 René N5 SPS Columnar

One of the three samples subjected to cyclic testing (Section 3.3.3.2) failed during the first 3 cycles. The other two samples survived 3 and 6 cycles. Two of the three samples spalled prior to completing isothermal oxidation test (Section 3.3.3.3). These samples failed following 6 and 10 hrs of isothermal oxidation. One sample survived 4 hrs of isothermal oxidation; however, this sample was found to be completely delaminated when viewed at higher magnifications in cross-section.

Images of a sample which failed following isothermal heat treatment are provided in Figure 56. These images show the oxidized surface of the exposed substrate following spallation of the top coat. Compositions of microstructural features shown in Figure 56 are provided in Table 29.

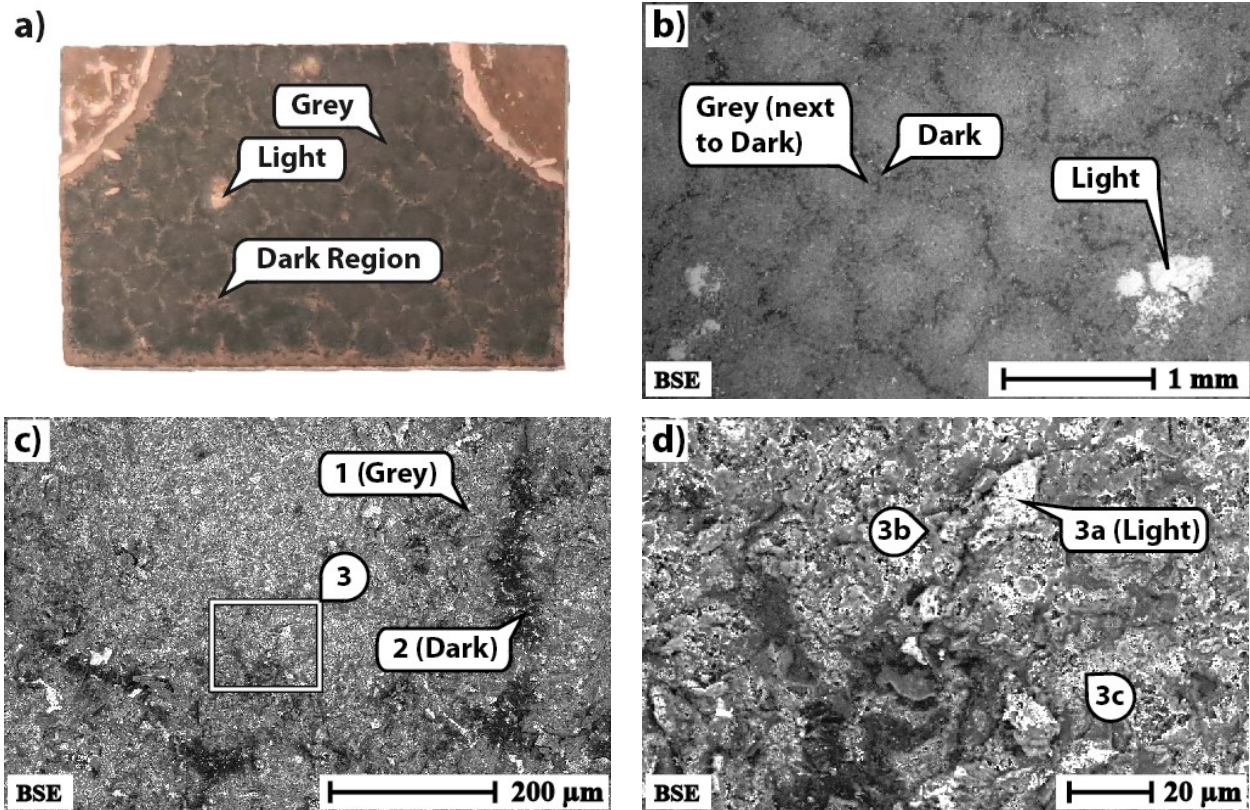


Figure 56: Exposed substrate of Columnar coated René N5 sample. a) photograph of sample, b) overall appearance, c) light, grey and dark regions and d) light region and surrounding oxides

Table 29: Composition of regions identified in Figure 56

Element	at. %					Element	wt. %				
	1	2	3a	3b	3c		1	2	3a	3b	3c
Al	15.92	26.84	8.17	15.91	9.84	Al	15.42	29.31	7.28	16.28	7.92
Co	1.83	0.95	1.09	1.92	1.32	Co	3.87	2.27	2.12	4.29	2.32
Cr	7.36	3.38	4.07	7.55	7.84	Cr	13.74	7.11	6.99	14.89	12.17
Ni	9.82	5.69	5.62	9.51	7.07	Ni	20.69	13.51	10.89	21.17	12.39
O	62.52	61.26	69.48	64.17	67.28	O	35.91	39.66	36.7	38.93	32.13
Ta	0.62	0.34	0.41	0.33	4.31	Ta	4.03	2.49	2.45	2.26	23.28
W	-	-	-	-	1.23	W	-	-	-	-	6.75
Zr	1.94	1.53	11.15	0.63	1.12	Zr	6.35	5.65	33.58	2.18	3.05

The light regions (labelled as “Light”) on the exposed substrate are fragments of top coat which remained adhered to the substrate following top coat spallation. Some of these regions are quite large (Figure 56a and Figure 56b) and some are smaller (Figure 56d, Region 3a). The grey regions (labelled “grey”) are characterized by high Al, Cr and Ni content (Figure 56c, Region 1). The light regions are surrounded by areas of relatively high Ta content (Figure 56d, Region 3c) and areas of high Al, Cr and Ni content (Figure 56d, Region 3b). Dark regions are characterized by a high proportion of Al (Figure 56c, Region 2).

Images of the backside of the spalled top coat are provided in Figure 57. Compositions of Figure 57 are provided in Table 30.

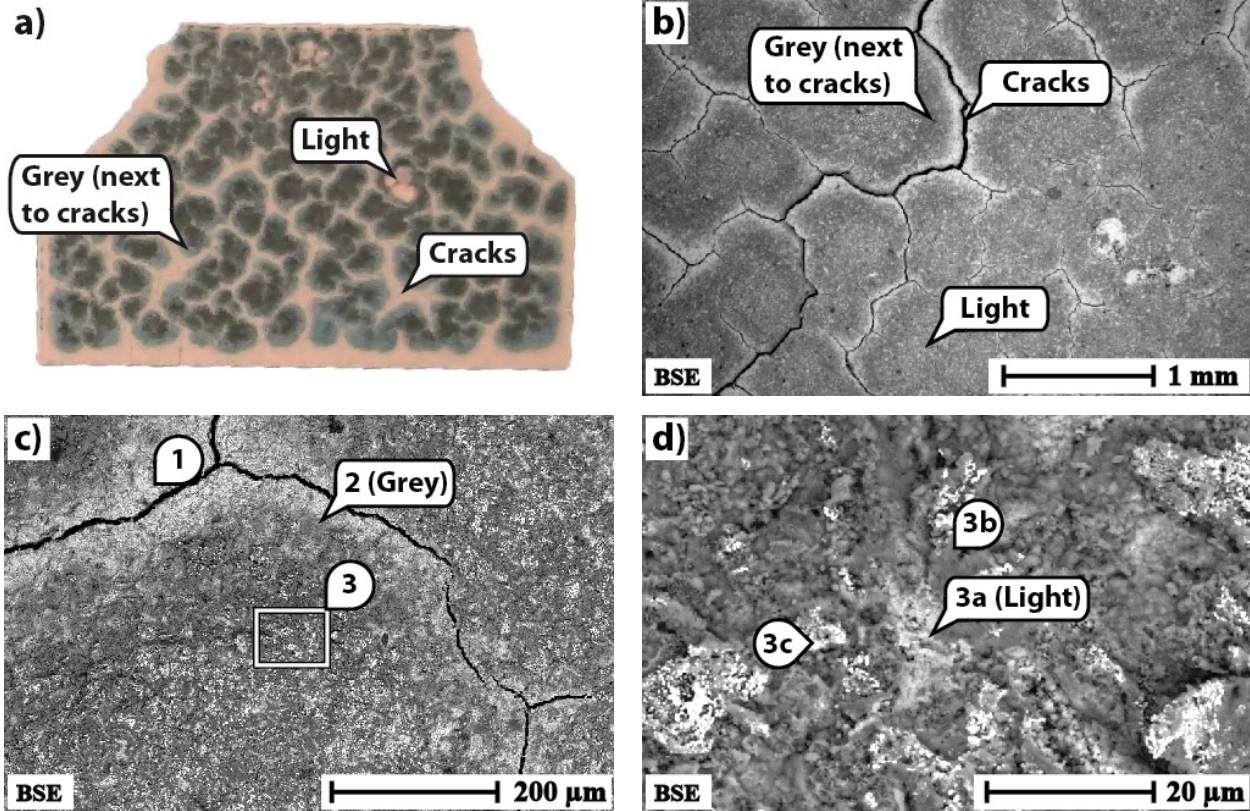


Figure 57: Columnar coated René N5 sample following 10 hrs isothermal heat treatment: a) photograph of backside of spalled top coat, b) backside of spalled top coat, c) exposed substrate following top coat spallation and d) exposed substrate following top coat spallation

Table 30: Composition of regions identified in Figure 57

Element	at. %					wt. %				
	1	2	3a	3b	3c	1	2	3a	3b	3c
Al	5.44	11.14	6.79	8.53	8.43	4.94	11.22	6.17	8.13	7.36
Co	0.44	1.02	0.83	1.77	1.7	0.87	2.24	1.65	3.68	3.24
Cr	2.37	4.06	4.2	10.45	7.27	4.15	7.88	7.35	19.19	12.23
Ni	3	6.29	5.43	7.31	8.34	5.93	13.78	10.73	15.15	15.84
O	74.43	70.87	71.55	66.96	67.21	40.11	42.31	38.55	37.84	34.79
Ta	-	-	0.38	-	1.99	-	-	2.32	-	11.65
Y	-	-	-	0.45	-	-	-	-	1.41	-
Zr	14.32	6.63	10.82	4.53	5.05	44	22.57	33.24	14.59	14.9

The regions adjacent to the cracks found in the top coat (labelled “Grey”) are characterized by high Al, Cr and Ni content (Figure 57c, Region 2). Light regions (labelled “Light”) have high Zr content (Figure 57d, Region 3a). Surrounding the “Light” regions are

oxides of high Ta content (Figure 57d, Region 3c) and regions of high Al, Cr and Ni content (Figure 53d, Region 3b).

Any samples which survived isothermal or cyclic heat treatment without apparent spallation had a visible gap between the top coat and the substrate (Figure 58) and when observed in cross-section, the substrate and coating were found to no longer be affixed to one another (Figure 59a and Figure 59b).

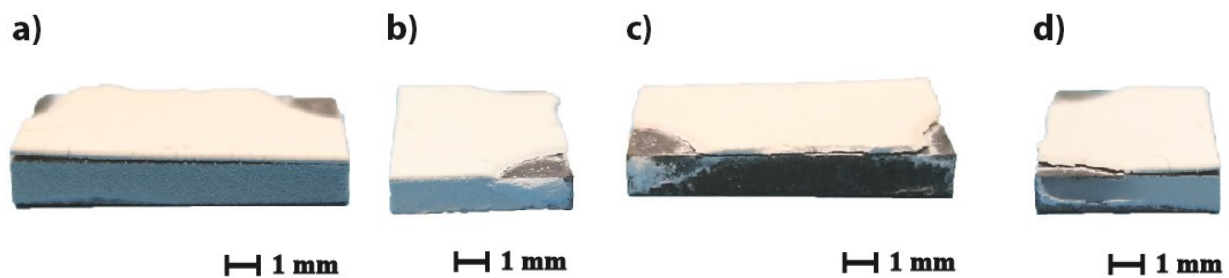


Figure 58: Columnar coated René N5 following 6 cycles. a) front, b) right c) back and d) left

Figure 59a is an image of the top coat following 4 hrs isothermal oxidation. The cracks in the top coat are similar in frequency and severity to those seen in the as-received sample (Figure 30a and Figure 30d). Coated samples were isothermally held for 2 hrs at 1150°C prior to top coat deposition. Figure 59b is an image of the TGO, which is quite irregular and does not resemble the structure of the René N5 samples oxidized for 2 hrs at 1150°C (Figure 48b).

Compositions corresponding to the regions identified in Figure 59 are provided in Table 31. An image of the top coat at higher magnification is provided in Figure 59c. Oxides of high Al, Cr and Ni content affixed to the top coat (Figure 59c, Region 2) as well as oxides containing Ta (Figure 59c, Region 1).

An Image of the substrate at higher magnification is provided in Figure 59d. On the substrate, different regions are characterized by relatively high Al content (Figure 59d, Region 4), a substantial proportion of Ta (Figure 59d, Region 5) and high Al, Cr and Ni content (Figure 59, Region 6).

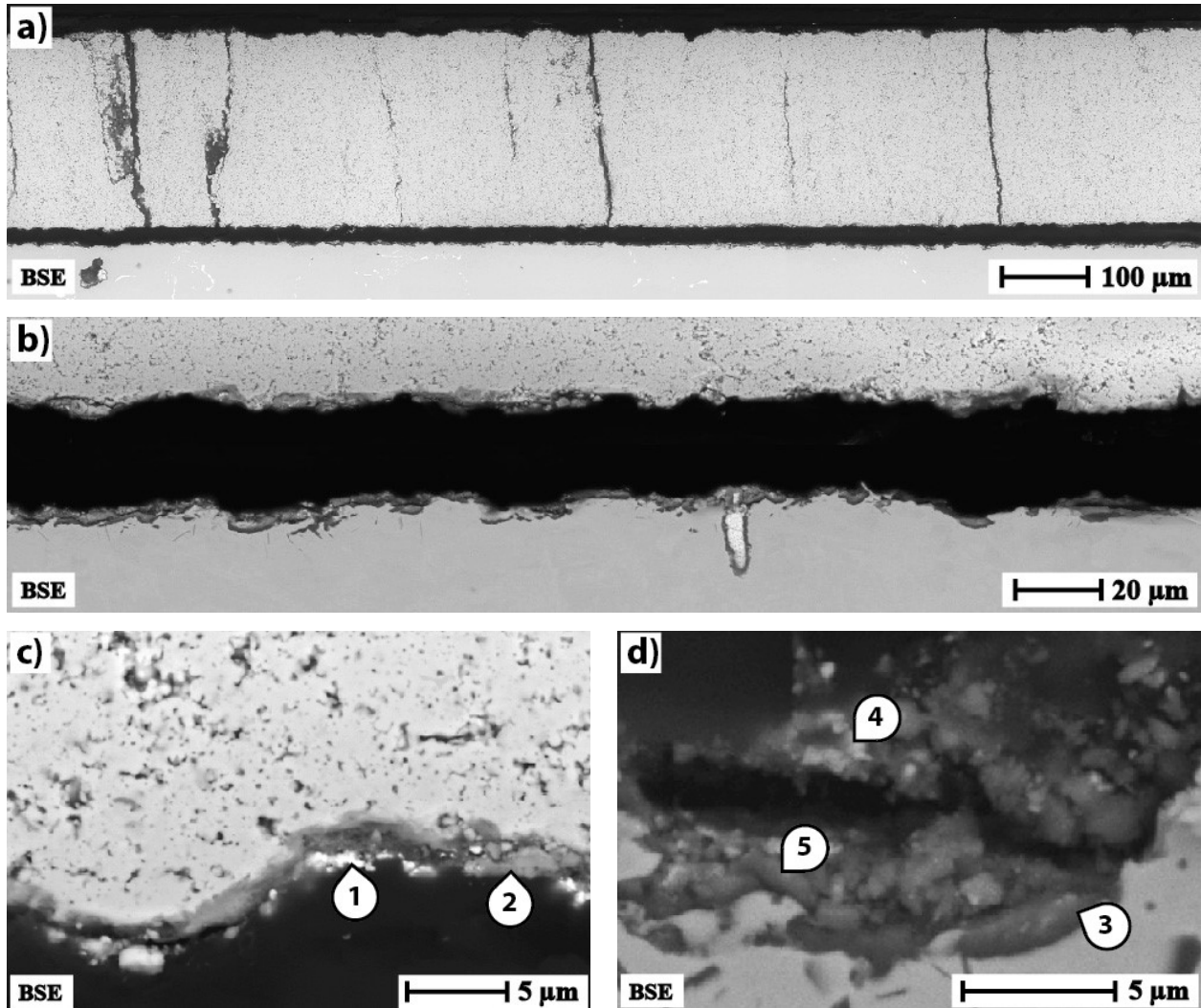


Figure 59: Columnar coated René N5 sample. a) general appearance of top coat following 4 hrs isothermal heat treatment, b) general appearance of substrate/top coat interface following 6 cycles, c) oxides adhered to top coat following 6 cycles and d) oxides adhered to substrate following 6 cycles

Table 31: Composition of regions identified in Figure 59

Element	at. %				
	1	2	3	4	5
Al	3.69	8.89	21.05	9.15	11.54
Co	1.92	1.57	1	2.79	1.2
Cr	7.69	4.68	5.92	8.32	3.14
Ni	10.92	7.21	8.07	19.35	9.23
O	65.12	73.15	62.48	50.56	73.02
Ta	2.34	-	-	6.08	0.86
Zr	8.3	4.47	1.48	3.75	1

Element	wt. %				
	1	2	3	4	5
Al	2.86	9.31	22.33	5.84	12.44
Co	3.26	3.59	2.32	3.89	2.83
Cr	11.5	9.44	12.1	10.23	6.52
Ni	18.44	16.42	18.63	26.84	21.65
O	29.97	45.41	39.31	19.12	46.69
Ta	12.18	-	-	26	6.22
Zr	21.78	15.82	5.31	8.09	3.65

5 Discussion

The results of isothermal oxidation of uncoated samples (Section 4.2) were assessed in terms of the oxide scale produced (Section 5.1). Based on this assessment, René N5 oxidized for 2 hrs was selected for further YSZ coating application. This decision was made based on the general knowledge that in order for an oxide scale to confer bonding to the YSZ and provide oxidation protection it should form an external, dense, adherent and uniform $\alpha\text{-Al}_2\text{O}_3$ scale [63].

Top coat/substrate adhesion was evaluated in this study and found to be very poor. All samples failed in less than 25 cycles, indicating that the work of separation between these interfaces is very low [42]. An assessment of these results is included in Section 5.2.

5.1 Oxidation of IN-738, CMSX-4 and René N5

The oxidized samples were assessed based on the general knowledge that in order for an oxide scale to confer bonding to the YSZ and provide oxidation protection it should form an external, dense, adherent and uniform $\alpha\text{-Al}_2\text{O}_3$ scale [63].

An internally oxidized subscale, not an external scale, formed on IN-738 at all oxidation holding times (Figure 34); as such IN-738 was not considered. CMSX-4 showed substantial spallation following 4 and 16 hrs, which resulted in the loss of the external $\alpha\text{-Al}_2\text{O}_3$ layer. Evidence of this is provided in Figure 42 in which regions of exposed substrate can be seen. René N5 showed moderate spallation following 4 hrs and somewhat more extensive spallation following 16 hrs of oxidation. Regions of exposed substrate can be seen in Figure 51b and

Figure 51c. Both CMSX-4 and René N5 had continuous Al_2O_3 external scales following 0.5, 1 and 2 hrs of oxidation (Figure 36a-c, Figure 37a-c, Figure 39, Figure 43a-c, Figure 44a-c, Figure 48), although some moderate spallation was noted on CMSX-4 following 2 hrs of oxidation (Figure 36c, Figure 37c).

A dense $\alpha\text{-Al}_2\text{O}_3$ scale will serve as an effective cation diffusion barrier, thereby preventing the diffusion and subsequent oxidation of other elements during service [88]. This should correspond to an Al_2O_3 growth exponent (n) of approximately 3 (Equation 6) [40]. Referring to the change in layer thickness vs. oxidation time for René N5 (Figure 50) and utilizing kinetic oxidation theory (Equation 6), Layer 1 (the Al_2O_3 layer adjacent to the scale/gas interface) was determined to have a growth exponent of 1.43, where $R^2=0.9973$ and Layer 2 (the layer adjacent to the substrate) was determined to have a growth exponent of 1.92, where $R^2=0.9999$ (Figure 60).

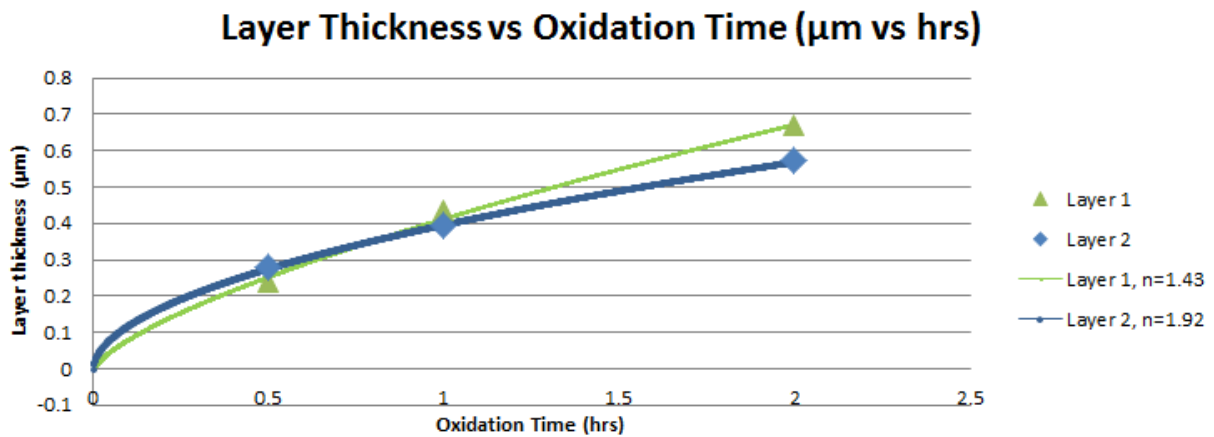


Figure 60: Oxidation kinetics of René N5

A growth exponent of 1.92 ($n \sim 2$) indicates that growth is dictated by diffusion through the scale [8]. This result is corroborated by the growth exponent for the layer at the scale/gas

interface (Layer 1), which is quite high, suggesting that significant cation diffusion is occurring through Layer 2, enabling the continued growth of Layer 1 [65]. Peaks for α - Al_2O_3 were detected on René N5 samples oxidized between 0.5 and 2 hrs, confirming the presence of α - Al_2O_3 (Figure 49a-c). However, a growth exponent of 3 would be indicative of the formation of a dense α - Al_2O_3 layer [40]; therefore, it can be concluded that this layer is not entirely composed of α - Al_2O_3 . As such, the Al_2O_3 layer may be a mixture of Al_2O_3 and other oxides or a mixture of α - Al_2O_3 and other transient Al_2O_3 phases [55, 65, 66]. XRD peaks for transient alumina phases were not distinct enough to be confidently identified (Figure 49). Therefore if transient phases are present they are present in small quantities.

For alloy CMSX-4 (Figure 41), the thickness of Layer 1 (layer adjacent to the scale/gas interface) was found to have almost no growth between 0.5 and 2 hrs of oxidation. Layer 2 (Al_2O_3 layer adjacent to the substrate) has a growth exponent of 2.5, where $R^2=0.9962$ (Figure 61).

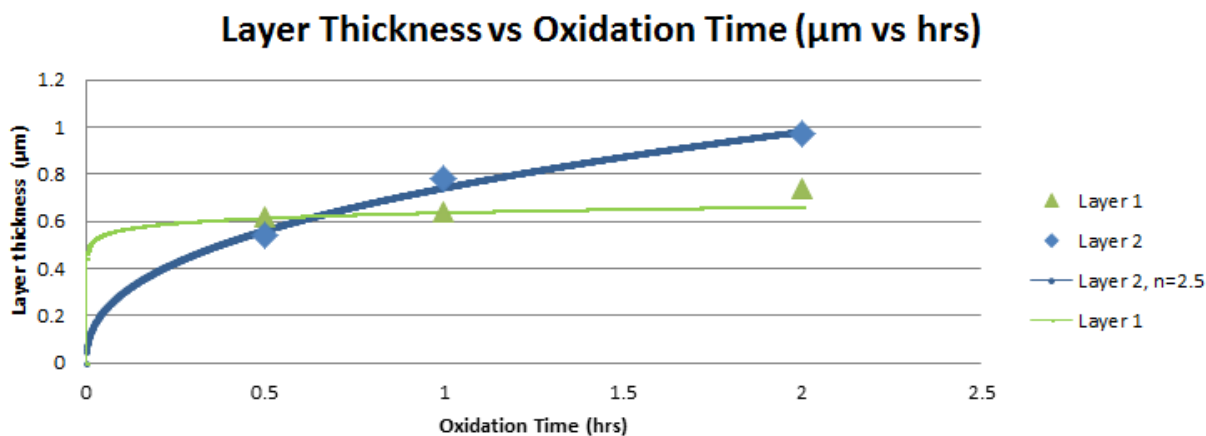


Figure 61: CMSX-4 oxidation kinetics

Near adherence to the cubic rate law suggests the formation of $\alpha\text{-Al}_2\text{O}_3$ [40], which was already confirmed via XRD results (Figure 40). The formation of $\alpha\text{-Al}_2\text{O}_3$ also explains the increasing concentration of Al with respect to time seen in all regions of Figure 38 and Figure 39, as $\alpha\text{-Al}_2\text{O}_3$ forms a diffusion barrier for other elements, reducing the growth of the scale via the cation transport mechanism (Figure 10a) [8, 37]. Furthermore, the lack of growth of the layer at the scale/gas interface suggests that little further cation diffusion to this layer occurred after it was initially established [65]. This conclusion is reached based on the assumption that no spallation of the layer at the scale/gas interface occurred. However, the slight growth of Layer 1 in conjunction with a growth exponent of 2.5 for Layer 2 suggests that perhaps Layer 2 has not yet reached a composition of 100% $\alpha\text{-Al}_2\text{O}_3$ and some transient phases may be present [8, 38, 40, 55, 65, 66]. However, if these phases are present, they are present in low quantity as they were not detected in XRD results (Figure 40).

The $\alpha\text{-Al}_2\text{O}_3$ layer must be adherent to the substrate in order to confer any protection [63]. Evidence suggests that René N5 had better Al_2O_3 scale adhesion to the substrate than

CMSX-4. This conclusion is supported by the significant degree of spallation noted on CMSX-4 (Figure 37) in comparison to René N5 (Figure 44). Furthermore, upon closer observation in cross-section, the scale formed on CMSX-4 (Figure 39) was found to not be adhered to the substrate whereas the scale formed on René N5 (Figure 48) was found to be consistently adhered to the substrate. Furthermore, adhesion will be enhanced by the Ta and Hf pegs present in the scale (Figure 46) [5, 33]. Hf (Figure 45, Region 1) is also known to improve not only TGO/substrate adhesion but also YSZ/TGO adhesion [3, 63].

Both CMSX-4 and René N5 have relatively uniform external Al_2O_3 scales when oxidized between 0.5 and 2 hrs (Figure 37a-c, Figure 39, Figure 44a-c and Figure 48). However, the oxidized eutectic regions on René N5 produce a somewhat uneven surface morphology (Figure 45). This uneven morphology is more pronounced at earlier oxidation times (Figure 44).

In order for an oxide scale to confer bonding to the YSZ and provide oxidation protection it should form an external, dense, adherent and uniform $\alpha\text{-Al}_2\text{O}_3$ scale [63]. Only CMSX-4 and René N5 oxidized from 0.5 to 2 hrs had a continuous $\alpha\text{-Al}_2\text{O}_3$ scale. These Al_2O_3 scales have growth exponents of 1.92 and 2.5 for CMSX-4 and René N5, respectively. This suggests that the Al_2O_3 layer formed on CMSX-4 may be denser than the one formed on René N5. However, in order for an oxide scale to confer bonding to the YSZ and to provide oxidation protection it should form an adherent $\alpha\text{-Al}_2\text{O}_3$ scale [63]. Evidence suggests that René N5 had better Al_2O_3 scale adhesion to the substrate than CMSX-4. Adhesion may be enhanced by the formation of pegs and the presence of Hf [3, 5, 33, 63]. René N5 has a relatively uniform external Al_2O_3 when oxidized between 0.5 and 2 hrs. Although the oxidized eutectic regions on

René N5 produce a somewhat uneven surface morphology, this effect is less-pronounced at 2 hrs than it is following 0.5 and 1 hrs of oxidation. Therefore, although CMSX-4 was found to have a denser Al_2O_3 scale, René N5 oxidized for 2 hrs was more adherent and somewhat similar in uniformity. Furthermore, Hf is anticipated to improve not only the adhesion of the scale to the substrate but to also improve the adhesion of the scale to the YSZ [3, 63]. As a result, SPS columnar and SPS DVC YSZ coatings were applied to the René N5 samples oxidized for 2 hrs.

5.2 Coated Samples

Top coat/substrate adhesion was very poor for all samples examined in this study. All samples failed in less than 25 cycles, indicating that the work of separation between these interfaces is very low [42]. In cyclic (Section 3.3.3.2) and isothermal (Section 3.3.3.3) oxidation testing even samples which did not show massive spallation were found to not be adhered to the substrate upon closer observation (Figure 55a-b and Figure 59a-b). Prior to any testing, DVC samples showed some adhesion to the substrate (Figure 29a); however, upon closer observation, a small gap was noted between the top coat and the substrate (Figure 29e). The gap was more evident for the columnar samples (Figure 30a and Figure 30e). The gaps seen in the samples were present even though a diffusion heat treatment (Section 3.2.2) had been conducted to promote bonding. The lack of adequate interfacial contact area lowers the work of separation between the top coat and the substrate (Equation 7) [42].

The oxide scale formed on the René N5 samples oxidized for 2 hrs (Figure 48c) prior to coating deposition is absent in the as-coated samples (Figure 55b, Figure 55d, Figure 59b and

Figure 59d). Although similar types of oxides can be found on the surfaces of these coated samples, they are scattered and not structured the same way (the bi-layered structure is no longer evident). Samples were grit-blasted prior to SPS coating deposition as coating failed to deposit on the as-oxidized René N5. It is believed that grit blasting prior to SPS coating application damaged the pre-existing α -Al₂O₃ layer. In this case, α -Al₂O₃ could no longer bond with the YSZ and at the same time will no longer provide a cation diffusion barrier [88]. This is particularly deleterious as one of the primary functions of the α -Al₂O₃ scale is to serve as an effective cation diffusion barrier, thereby preventing the diffusion and subsequent oxidation of other elements during service [88]. In particular, lack of an α -Al₂O₃ diffusion barrier is associated with an increased amount of spinel, Ni(Al,Cr)₂O₄, formation [65]. Elements present in high concentration (such as Ni) and elements with low standard free energies of formation (such as Cr) will most likely oxidize [8] upon being exposed to an oxidizing environment since YSZ is oxygen transparent [4]. This may explain the high proportion of these oxides seen on the surface.

The presence of islands of top coat material on the exposed substrate and the grey oxide region on the YSZ (Figure 62) suggests that there is some bonding between the oxidized René N5 and YSZ top coat where there may be sufficient alumina present.

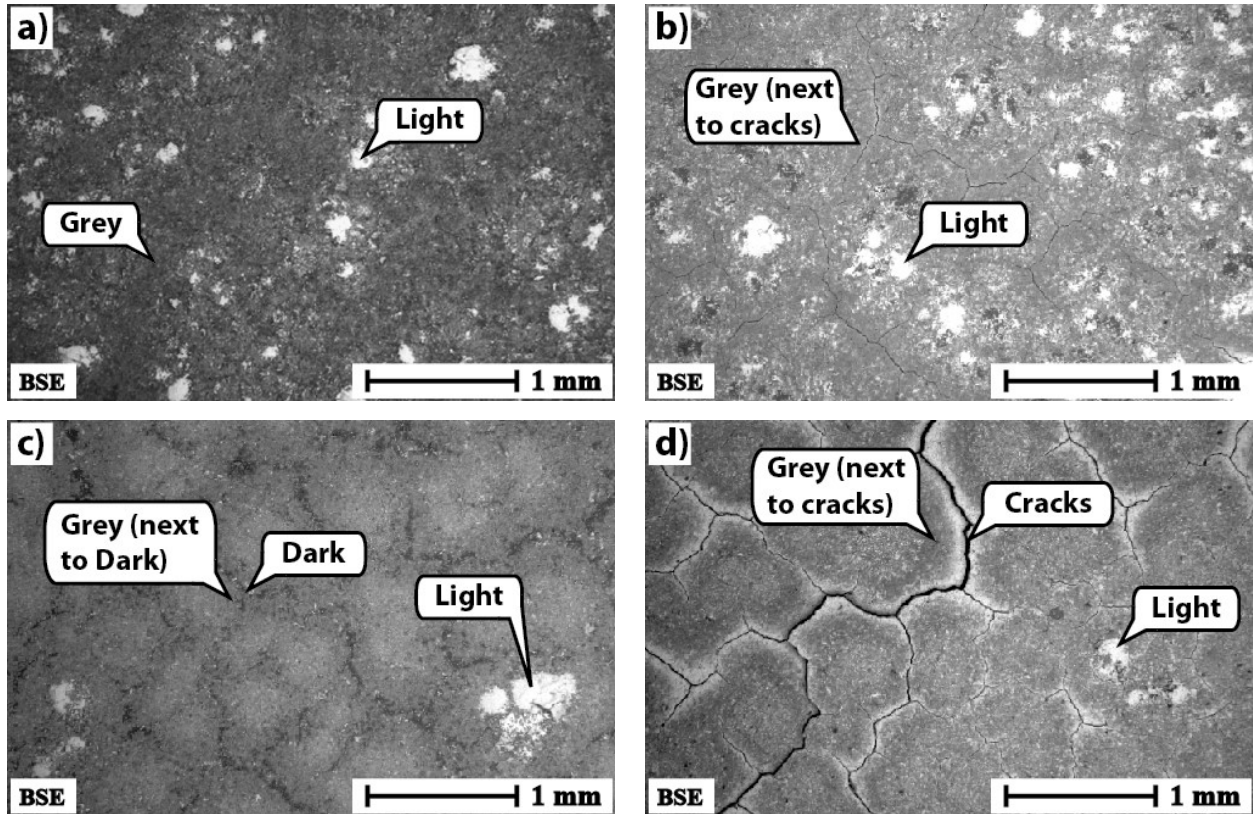


Figure 62: Coated René N5 following spallation. a) exposed substrate of DVC coated sample, b) backside of spalled top coat of DVC coated sample, c) exposed substrate of DVC coated sample, d) backside of spalled top coat of DVC coated sample

“Light” regions indicated in Figure 62 are believed to be regions in which pieces of top coat adhered to the substrate or in which pieces of coating were removed from the top coat. This suggests that the stresses generated during oxidation exposure were sufficient to tear pieces from the top coat [41]. These areas are characterized by higher Ta content than other areas as well as a greater proportion of Al (Figure 52c, Figure 53d, Figure 56d and Figure 57d). This suggests that both Al and Ta in these localized regions had good adhesion to the coating [41]. However, these elements were scattered non-uniformly across the surface and therefore, the fraction of interfacial contact area with the top coat was low [41]. Tantalum has been found to improve TGO adhesion in small quantities in nickel-based superalloys but to have a

profoundly negative effect at slightly higher concentrations [78]. This may be related to the linear growth kinetics of its most stable oxide, Ta₂O₅ which would lower interfacial contact area in contrast to its anticipated favourable adhesion to ceramics due to the 7 vacancies present in its 5d subshell (Table A-2) [42]. However, the concentration of Ta in the un-oxidized substrate was localized. In this system it seems to have provided a positive effect on adhesion.

No regions of bare alloy were found on the substrate surfaces following spallation (Figure 52b and Figure 56b) suggesting that TGO adhesion to the substrate was good [41]. This may have been related to the presence of Ta and Hf oxide pegs as these pegs would be anticipated to mechanically key the oxide to the alloy surface [3, 5, 33].

Oxides rich in Ni, Cr and Al were found on every coated sample (Figure 52, Figure 53, Figure 55, Figure 56, Figure 57 and Figure 59). These oxides are associated with spinel, Ni(Al,Cr)₂O₄. Spinel is often reported in literature as it is generally believed to have a particularly deleterious impact on TGO performance due to its specific volume mismatch and rapid growth rate [61, 65, 68, 70]. The thicker and more continuous the spinel layer is, the greater the deleterious impact on TGO performance [65].

These oxides may have come from a variety of sources. One likely source is the pre-oxidized sample itself - René N5 oxidized at 1150°C for 2 hrs had a high proportion of spinel at what would become the TGO/top coat interface (Figure 48, Region 1 and Figure 49c). Following diffusion heat treatment substantial amounts of Ni (9.5-9.9 at. %) were found diffused into the top coat materials (Figure 29e, Region 2 and Figure 30e, Region 2), suggesting that spinel had been present at the TGO/top coat interface prior to vacuum diffusion heat

treatment (no new oxides will form in vacuum so only pre-existing oxides/elements would have diffused into the coating).

6 Conclusions and Future Work

The first phase of this thesis focused on the evaluation of oxides formed on three superalloy substrates. The following observations were made:

- IN-738 oxidized to produce an external scale composed of islands of Cr_2O_3 overlaid with rutile- TiO_2 oxides. The alloy formed an internal oxide scale adjacent to the surface composed predominantly of oxides of Nb, Ta and Ti. At increasing depth, an internal subscale of predominantly $\alpha\text{-Al}_2\text{O}_3$ was present. Spallation of the Cr_2O_3 and rutile- TiO_2 external scale occurred following up to 4 hrs of oxidation.
- CMSX-4 produced a uniform, external scale with a predominantly $\alpha\text{-Al}_2\text{O}_3$ layer adjacent to the substrate and an outer layer composed mainly of rutile- TiO_2 , NiAl_2O_4 and NiO at the scale/gas interface. A thin layer of Ta-rich oxides was found between these two layers. Moderate spallation occurred following 2 hrs of oxidation with substantial spallation following 4 hrs of oxidation.
- René N5 produced a relatively uniform external scale with a layer composed predominantly of $\alpha\text{-Al}_2\text{O}_3$ adjacent to the substrate and a layer composed mainly of $\text{Ni}(\text{Al,Cr})_2\text{O}_4$ and NiO at the scale/gas interface. A thin layer of Ta-rich oxides was found between these two layers. Moderate spallation occurred following 4 hrs of oxidation with substantial spallation following 16 hrs of oxidation. Oxidized eutectic regions rich in predominantly Ta_2O_5 were scattered across the

sample surface with localized Hf-rich oxides. These regions produced Ta- and Hf-rich oxide pegs.

The oxidized samples were assessed based on the general knowledge that in order for an oxide scale to confer bonding to the YSZ and provide oxidation protection it should form an external, dense, adherent and uniform α -Al₂O₃ scale. IN-738 had an internal Al₂O₃ subscale; whereas CMSX-4 and René N5 produced external α -Al₂O₃ scales with growth exponents of 2.5 and 1.92, respectively. Although CMSX-4 produced a more uniform external scale and had a slightly higher growth exponent suggesting that the Al₂O₃ layer was denser, it showed poor adhesion to the substrate. The adhesion of René N5 to the substrate was quite good and was most likely enhanced by the presence of Ta and Hf oxide pegs. As the somewhat uneven surface morphology found on René N5 was less pronounced following 2 hrs of oxidation, René N5 was coated with SPS DVC and Columnar YSZ top coats and tested further.

Top coat/substrate adhesion was very poor. All samples failed in less than 25 cycles, indicating that the interface adhesion is very low. The primary reason for the low adhesion is the lack of sufficient surface coverage of a pure α -Al₂O₃ scale. The oxide scale which formed on René N5 oxidized for 2 hrs is completely absent on the as-coated samples. Samples were grit-blasted prior to SPS coating deposition and it is believed that grit the blasting process damaged the pre-existing α -Al₂O₃ layer. For this reason samples analyzed prior to any testing revealed that the YSZ was not adhered to the substrate. Gaps were noted between the top coat and the substrate on both DVC and columnar samples. The gaps seen in the samples were present even though a diffusion heat treatment had been conducted to promote bonding.

Furthermore spinel, $\text{Ni}(\text{Al,Cr})_2\text{O}_4$, formation also contributed to the poor top coat and TGO adhesion. René N5 oxidized at 1150°C for 2 hrs had a high proportion of spinel at what would become the TGO/top coat interface.

In contrast to top coat/TGO adhesion, substrate/TGO adhesion was considered to be relatively strong, as no bare regions of substrate were found on the surface of the coated samples. This may have been related to the presence of Ta and Hf oxide pegs as these pegs would be anticipated to mechanically key the oxide to the alloy surface. Aluminum and Tantalum were found to have good adhesion to the coating. However, these elements were scattered non-uniformly across the surface and therefore, interfacial contact area with the top coat was low.

Directly depositing a top coat onto a substrate requires further investigation. A substrate which produces an external, dense, adherent and uniform $\alpha\text{-Al}_2\text{O}_3$ scale is a necessity [63]. Spinel should be eliminated [61, 65, 68, 70]. This may be achieved via oxidation in a low-oxygen environment in which the partial pressure of oxygen required for selective Al_2O_3 formation could be estimated using Equations 1-4 [7, 37]. Selective oxidation of Al_2O_3 would eliminate the spinel layer adjacent to the scale/gas interface [8].

As illustrated in other studies [85] and as emphasized in this study, substrate selection is paramount. The substrate must have sufficient Al concentration to form a steady state Al_2O_3 scale [8]. To enhance adhesion, a substrate with a high proportion of REs: La, Y or Ce [3] or any combination of them (as combinations of REs are noted to have a synergistic effect [3, 4]) would most likely be beneficial.

To eliminate the need for grit blasting prior to SPS YSZ deposition, the samples could be grit blasted prior to pre-oxidation heat treatment. This would allow the $\alpha\text{-Al}_2\text{O}_3$ scale present following pre-oxidation to remain intact which would help reduce or completely eliminate spinel formation during subsequent oxidation [65].

References

- [1] C. Soares, Gas Turbines: A Handbook of Air, Land and Sea Applications, Burlington: Butterworth-Heinemann, 2008.
- [2] M. P. Boyce, Gas Turbine Engineering Handbook, Burlington: Gulf Professional Publishing, 2006.
- [3] B. Geddes, H. Leon and X. Huang, Superalloys: Alloying and Performance, Materials Park: ASM International, 2010.
- [4] R. C. Reed, The Superalloys: Fundamentals and Applications, New York: Cambridge University Press, 2006.
- [5] H. Xu and H. Guo, Thermal Barrier Coatings, Philadelphia: Woodhead Publishing, 2011.
- [6] R. J. Hunt, "The History of the Industrial Gas Turbine (Part 1 The First Fifty Years 1940-1990)," The Institution of Diesel and Gas Turbine Engineers, Bedford Heights, 2011.
- [7] R. Chang, Chemistry, 10th Ed., New York: McGraw-Hill, 2010.
- [8] D. J. Young, High Temperature Oxidation and Corrosion of Metals, Oxford: Elsevier, 2008.
- [9] M. J. Donachie and S. J. Donachie, Superalloys: A Technical Reference, Materials Park: ASM International, 2002.
- [10] Y. Tamarin, Protective Coatings for Turbine Blades, Materials Park, OH: ASM International, 2002.
- [11] D. R. Askeland, P. P. Fulay and W. J. Wright, The Science and Engineering of Materials, 6th edition, Stamford: Cengage Learning, Inc., 2010.
- [12] S. Zhang and D. Zhao, Aerospace Materials Handbook, Boca Raton, FL: CRC Press, 2013.
- [13] C. Xu and W. Gao, "Pilling-Bedworth Ratio for Oxidation of Alloys," *Material Research Innovations*, vol. 3, no. 4, pp. 231-235, 1999.
- [14] A. Szczotok and B. Chmiela, "Effect of Heat Treatment on Chemical Segregation in CMSX-4

- Nickel-Base Superalloy," *Journal of Materials Engineering and Performance*, vol. 23, no. 8, pp. 2739-2747, 2014.
- [15] P. Limkitjaroenporn, J. Kaewkhao and S. Asavavisithchai, "Determination of Mass Attenuation Coefficients and Effective Atomic Numbers for Inconel 738 Alloy for Different Energies Obtained from Compton Scattering," *Annals of Nuclear Energy*, vol. 53, p. 64–68, 2013.
- [16] I. Guzman, E. Granda, R. Mendez, G. Lopez, J. Acevedo and D. Gonzalez, "Particle Size of Gamma Prime as a Result of Vacuum Heat Treatment of INCONEL 738 Super Alloy," *Journal of Materials Engineering and Performance*, vol. 22, no. 4, pp. 1143-1148, 2013.
- [17] A. T. Egbewande, R. A. Buckson and O. A. Ojo, "Analysis of Laser Beam Weldability of Inconel 738 Superalloy," *Materials Characterization*, vol. 61, no. 5, pp. 569-574, 2010.
- [18] H. Zhang and O. A. Ojo, "Cr-rich Nanosize Precipitates in a Standard Heat-treated Inconel 738 Superalloy," *Philosophical Magazine*, vol. 90, no. 6, p. 765–782, 2010.
- [19] K. Harris and G. L. Erickson, "Single Crystal Alloy Technology". United States Patent 4643782, 17 February 1987.
- [20] U. Bruckner, A. Epishin and T. Link, "Local X-ray Diffraction Analysis of the Structure of Dendrites in Single-Crystal Nickel-Base Superalloys," *Acta Materialia*, vol. 45, no. 12, p. 5223–5231, 1997.
- [21] B. C. Wilson, J. A. Hickman and G. E. Fuchs, "The Effect of Solution Heat Treatment on a Single-Crystal Ni-Based Superalloy," *The Journal of The Minerals, Metals & Materials Society*, vol. 55, no. 3, pp. 35-40, 2003.
- [22] D. Ma and U. Grafe, "Microsegregation in Directionally Solidified Dendritic-Cellular Structure of Superalloy CMSX-4," *Materials Science and Engineering*, vol. 270, no. 2, p. 339–342, 1999.
- [23] M. Karunaratne, D. C. Cox, P. Carter and R. C. Reed, "Modelling of the Microsegregation in CMSX-4 Superalloy and its Homogenization During Heat Treatment," in *Superalloys 2000*, Metals Park, 2000.
- [24] U. Hemmersmeier and M. Feller-Kniepmeier, "Element Distribution in the Macro- and Microstructure of Nickel-Base Superalloy CMSX-4," *Materials Science and Engineering*, vol. 248, no. 1-2, p. 87–97, 1998.

- [25] P. A. Shade, M. D. Uchic, D. M. Dimiduk, G. B. Viswanathan, R. Wheeler and H. L. Fraser, "Size-Affected Single-Slip Behavior of René N5 Microcrystals," *Materials Science and Engineering*, vol. 535, pp. 53-61, 2012.
- [26] C. S. Wukusick and L. Buchakjian, "Improved Property Balanced Nickel-base Superalloys for Producing Single Crystal Articles". United Kingdom Patent GB2235697, 13 March 1991.
- [27] P. Caron and T. Khan, "Evolution of Ni-based Superalloys for Single Crystal Gas Turbine Blade Applications," *Aerospace Science and Technology*, vol. 3, no. 8, pp. 513-523, 1999.
- [28] Y. A. Bondarenko, E. N. Kablov and G. I. Morozova, "Effect of High Gradient Directed Crystallization on the Structure and Phase Composition of a High-Temperature Alloy of the Type Rene N5," *Metal Science and Heat Treatment*, vol. 41, no. 2, pp. 61-64, 1999.
- [29] National Research Council (U.S.) Committee on Coatings for High-Temperature Structural Materials, "Coatings for High-Temperature Structural Materials: Trends and Opportunities," National Academy Press, Washington, D.C., 1996.
- [30] P. L. Fauchais, J. V. Heberlein and M. I. Boulos, *Thermal Spray Fundamentals From Powder to Part*, New York: Springer, 2014.
- [31] K. N. Lee, "Protective Coatings For Gas Turbines," in *The Gas Turbine Handbook*, U.S. Department of Energy-National Energy Technology Laboratory (NETL), 2006, pp. 419-432.
- [32] X. Huang, P. Puetz, Q. Yang and Z. Tang, "Characterisation of Transient Oxide Formation on NiCrAlY after Heat Treatment in Vacuum," *Surface Engineering*, vol. 27, no. 5, pp. 368-375, 2011.
- [33] E. A. Jarvis and E. A. Carter, "The Role of Reactive Elements in Thermal Barrier Coatings," *Computing in Science and Engineering*, vol. 4, no. 2, pp. 33-41, 2002.
- [34] A. Ganvir, N. Curry, S. Bjorklund, N. Markocsan and P. Nylen, "Characterization of Microstructure and Thermal Properties of YSZ Coatings Obtained by Axial Suspension Plasma Spraying (ASPS)," *Journal of Thermal Spray Technology*, vol. 24, no. 7, pp. 1195-1204, 2015.
- [35] Northwest Mettech Corporation, "Thermal Barrier Coatings: Variable Density Microstructures," Northwest Mettech Corp., 2015. [Online]. Available: <http://www.mettech.com/coating-solutions/thermal-barrier-coatings.php>. [Accessed 26 November 2015].

- [36] H. Dong, *Surface Engineering of Light Alloys*, Boca Raton: Woodhead Publishing, 2010.
- [37] I. Anžel, "High Temperature Oxidation of Metals and Alloys," *Metallurgija - Journal of Metallurgy (MJoM)*, vol. 13, no. 4, pp. 325-336, 2007.
- [38] N. Birks, G. H. Meier and F. S. Pettit, *Introduction to the High Temperature Oxidation of Metals*, Second Edition, Cambridge: Cambridge University Press, 2006.
- [39] C. Wagner, "The Evaluation of Data Obtained with Diffusion Couples of Binary Single-Phase and Multiphase Systems," *Acta Metallurgica*, vol. 17, no. 2, pp. 99-107, 1969.
- [40] W. J. Quadackers, D. Naumenko, E. Wessel and V. Kochubey, "Growth Rates of Alumina Scales on Fe-Cr-Al Alloys," *Oxidation of Metals*, vol. 61, no. 1/2, pp. 17-37, 2004.
- [41] P. R. Dillon, "High-Temperature Adhesives and Bonding," in *High Temperature Materials and Mechanisms*, New York, CRC Press, 2014, pp. 69-93.
- [42] A. Christensen, E. A. Asche and E. A. Carter, "Atomic-Level Properties of Thermal Barrier Coatings: Characterization of Metal-Ceramic Interfaces," in *Chemical Dynamics in Extreme Environments*, Singapore, World Scientific Publishing Co. Pte. Ltd., 2001, pp. 490-546.
- [43] M. W. Finnis, "The Theory of Metal-Ceramic Interfaces," *Journal of Physics: Condensed Matter*, vol. 8, p. 5811-5836, 1996.
- [44] P. Aloke, L. Tomi, V. Vesa and D. V. Sergiy, *Thermodynamics, Diffusion and the Kirkendall Effect in Solids*, Cham: Springer, 2014.
- [45] D. Li, H. Guo, D. Wang, T. Zhang, S. Gong and H. Xu, "Cyclic Oxidation of β -NiAl with Various Reactive Element Dopants and 1200°C," *Corrosion Science*, vol. 66, pp. 125-135, 2013.
- [46] H. E. Evans, "Oxidation Failure of TBC Systems: An Assessment of Mechanisms," *Surface & Coatings Technology*, vol. 206, no. 7, p. 1512-1521, 2011.
- [47] M. Daroonparvar, M. A. Mat Yajid, N. M. Yusof, H. R. Bakhsheshi-Rad, Z. Valefi and E. Hamzah, "Effect of Y₂O₃ Stabilized ZrO₂ Coating with Tri-Model Structure on Bi-Layered Thermally Grown Oxide Evolution in Nano Thermal Barrier Coating Systems," *Journal of Rare Earths*, vol. 32, no. 1, pp. 57-77, 2014.
- [48] D. Li, H. Guo, D. Wang, T. Zhang and G. Shengkai, "Cyclic Oxidation of β -NiAl with Various Reactive Element Dopants and 1200°C," *Corrosion Science*, vol. 66, pp. 125-135, 2013.

- [49] N. B. Pilling and R. E. Bedworth, "The Oxidation of Metals at High Temperatures," *Journal of the Institute of Metals*, vol. 29, pp. 529-591, 1923.
- [50] J. Stringer, "Stress Generation and Relief in Growing Oxide Films," *Corrosion Science*, vol. 10, pp. 513-543, 1970.
- [51] W. G. Fahrenholtz, E. J. Wuchina, W. E. Lee and Y. Zhou, *Ultra-High Temperature Ceramics: Materials for Extreme Environment Applications*, Hoboken, NJ: John Wiley & Sons, Inc., 2014.
- [52] R. Eriksson, S. Johansson, H. Brodin, E. Broitman, L. Östergren and X.-H. Li, "Influence of Substrate Material on the Life of Atmospheric Plasma Sprayed Thermal Barrier Coatings," *Surface & Coatings Technology*, vol. 232, pp. 795-803, 2013.
- [53] W. R. Chen, X. Wu, D. Dudzinski and P. C. Patnaik, "Modification of Oxide Layer in Plasma-Sprayed Thermal Barrier Coatings," *Surface & Coatings Technology*, vol. 200, no. 20-21, pp. 5863-5868, 2006.
- [54] M. Moniruzzaman, M. Maeda, Y. Murata and M. Morinaga, "Degradation of High-temperature Oxidation Resistance for Ni-based Alloys by Re Addition and the Optimization of Re/Al Content," *ISIJ International*, vol. 43, no. 3, pp. 386-393, 2003.
- [55] H. Svensson, P. Knutsson and K. Stiller, "Formation and Healing of Voids at the Metal-Oxide Interface in NiAl Alloys," *Oxidation of Metals*, vol. 71, no. 3-4, p. 143-156, 2009.
- [56] W. R. Chen, X. Wu, B. R. Marple and P. C. Patnaik, "Oxidation and Crack Nucleation-Growth in an Air-Plasma-Sprayed Thermal Barrier Coating with NiCrAlY Bond Coat," *Surface & Coatings Technology*, vol. 197, no. 1, pp. 109-115, 2005.
- [57] C. Kaplin and M. Brochu, "The Effect of Grain Size on the Oxidation of NiCoCrAlY," *Applied Surface Science*, vol. 301, p. 258-263, 2014.
- [58] J. A. Haynes, E. D. Rigney, M. K. Ferber and W. D. Porter, "Oxidation and Degradation of a Plasma-Sprayed Thermal Barrier Coating System," *Surface & Coating Technology*, Vols. 86-87, no. 1, pp. 102-108, 1996.
- [59] E. A. Shillington and D. R. Clarke, "Spalling Failure of a Thermal Barrier Coating Associated with Aluminum Depletion in the Bond-Coat," *Acta Metallurgica*, vol. 47, no. 4, pp. 1297-1305, 1999.
- [60] A. Rabiei and A. G. Evans, "Failure Mechanisms Associated with the Thermally Grown Oxide

- in Plasma-Sprayed Thermal Barrier Coatings," *Acta Materialia*, vol. 48, no. 15, p. 3963–3976, 2000.
- [61] C. H. Lee, H. K. Kim, H. S. Choi and H. S. Ahn, "Phase Transformation and Bond Coat Oxidation Behavior of Plasma-Sprayed Zirconia Thermal Barrier Coating," *Surface and Coatings Technology*, vol. 124, no. 1, p. 1–12, 2000.
- [62] B. H. Kear, F. S. Pettit, D. E. Fornwalt and L. P. Lemaire, "On the Transient Oxidation of a Ni-15Cr-6Al Alloy," *Oxidation of Metals*, vol. 3, no. 6, pp. 557-569, 1971.
- [63] R. V. McVay, P. Williams, G. H. Meier, F. S. Pettit and J. L. Smialek, "Oxidation of Low Sulfur Single Crystal Nickel-Base Superalloys," in *Superalloys 1992*, Warrendale, PA, The Minerals, Metals & Materials Society, 1992, pp. 807-816.
- [64] J. Muller and D. Neuschütz, "Efficiency of α -alumina as Diffusion Barrier between Bond Coat and Bulk Material of Gas Turbine Blades," *Vacuum*, vol. 71, no. 1-2, pp. 247-251, 2003.
- [65] M. H. Sullivan and D. R. Mumm, "Transient Stage Oxidation of MCrAlY Bond Coat Alloys in High Temperature, High Water Vapour Content Environments," *Surface & Coatings Technology*, vol. 258, pp. 963-972, 2014.
- [66] M. J. Stiger, "Correlation of Short-Term to Long-Term Oxidation Testing for Alumina Forming Alloys and Coatings".
- [67] Y. F. Su, L. F. Allard, D. W. Coffey and W. Y. Lee, "Effects of an α -Al₂O₃ Thin Film on the Oxidation Behavior of a Single-Crystal Ni-Based Superalloy," *Metallurgical and Materials Transactions*, vol. 35, no. 3, pp. 1055-1065, 2004.
- [68] D. Mercier, B. D. Gauntt and M. Brochu, "Thermal stability and oxidation behavior of nanostructured NiCoCrAlY coatings," *Surface & Coatings Technology*, vol. 205, no. 17-18, p. 4162–4168, 2011.
- [69] A. Hesnawi, H. Li, Z. Zhou, G. Shengkai and H. Xu, "Isothermal Oxidation Behaviour of EB-PVD MCrAlY Bond Coat," *Vacuum*, vol. 81, p. 947–952, 2007.
- [70] M. Daroonparvar, M. A. Mat Yajid, N. M. Yusof, M. S. Hussain and H. R. Bakhsheshi-Rad, "Formation of a Dense and Continuous Al₂O₃ Layer in Nano Thermal Barrier Coating Systems for the Suppression of Spinel Growth on the Al₂O₃ Oxide Scale During Oxidation," *Journal of Alloys and Compounds*, vol. 571, pp. 205-220, 2013.

- [71] L. Rivoaland, V. Maurice, M. P. Bacos and P. Marcus, "Sulphur Segregation on Free and Oxidized NiAl(001)," *Surface and Interface Analysis*, vol. 34, no. 1, pp. 400-404, 2002.
- [72] S. Y. Hong, A. B. Anderson and J. L. Smialek, "Sulfur at Nickel-Alumina Interfaces: Molecular Orbital Theory," *Surface Science*, vol. 230, no. 1-3, pp. 175-183, 1990.
- [73] A. B. Anderson, S. P. Mehandru and J. L. Smialek, "Dopant Effect of Yttrium and the Growth and Adherence of Alumina on Nickel-Aluminum Alloys," *Journal of the Electrochemical Society*, vol. 132, no. 7, pp. 1695-1701, 1985.
- [74] M. Zagula-Yavorska, J. Romanowska and M. P. J. Sieniawski, "The Microstructure and Oxidation Resistance of the Aluminide Coatings Deposited by CVD Method on Pure Nickel and Hafnium-doped Nickel Superalloys," *Archives of Civil and Mechanical Engineering*, vol. 15, pp. 862-872, 2015.
- [75] J. Stringer, "The Oxidation of Tantalum at High Temperatures: Geometrical Effects," *Journal of Less-Common Metals*, vol. 16, pp. 55-64, 1968.
- [76] R. E. Pawel and J. J. Campbell, "Stress Measurements During the Oxidation of Tantalum and Niobium," *Acta Metallurgica*, vol. 14, pp. 1827-1833, 1966.
- [77] H. Nagai and M. Okabayashi, "Deleterious Effect of Ti Addition on the Oxidation Resistance of Ni-20Cr Alloy," *Transactions of the Japan Institute of Metals*, vol. 22, no. 10, pp. 691-698, 1981.
- [78] S. W. Yang, "Effect of Ti and Ta on the Oxidation of a Complex Superalloy," *Oxidation of Metals*, vol. 15, no. 5, pp. 375-397, 1981.
- [79] B. G. Cade, W. F. Caley and N. L. Richards, "Comparison of Oxidation Performance of Two Nickel Base Superalloys for Turbine Applications," *Canadian Metallurgical Quarterly*, vol. 53, no. 4, pp. 460-468, 2014.
- [80] C. Zhu, M. Shi, S. Yang, H. Zhang, Z. Yang and B. Ding, "Growth of Radial Arranged TiO₂ Nanorods by Direct Oxidation of Al-Coated In-738 Superalloy," *Journal of Alloys and Compounds*, vol. 485, no. 1-2, p. 328-332, 2009.
- [81] M. M. Smith, "Comparative Oxidation Study of Un-Coated and Coated CMSX-4 and CMSX-486 Single Crystal Superalloys," Department of Mechanical and Manufacturing Engineering: University of Manitoba, Winnipeg, AB, 2012.
- [82] M. Bensch, A. Sato, N. Warnken, E. Affeldt, R. C. Reed and U. Glatzel, "Modelling of High

- Temperature Oxidation of Alumina-Forming Single-Crystal Nickel-Base Superalloys," *Acta Materialia*, vol. 60, no. 15, pp. 5468-5480, 2012.
- [83] M. Bensch, J. Preußner, R. Huttner, G. Obigodi, S. Virtanen, J. Gabel and U. Glatzel, "Modelling and Analysis of the Oxidation Influence on Creep Behaviour of Thin-Walled Structures of the Single-Crystal Nickel-Base Superalloy Rene N5 at 980C," *Acta Materialia*, vol. 58, no. 5, p. 1607–1617, 2010.
- [84] K. Pruessner and H. Harada, "Microstructural Observations on Oxidized Ni-Based Superalloy TMS-75 and PGM-Doped Derivatives," *Journal of The Electrochemical Society*, vol. 157, no. 11, pp. 95-98, 2010.
- [85] R. T. Wu, K. Kawagishi, H. Harada and R. C. Reed, "An Investigation of the Compatibility of Nickel-Based Single Crystal Superalloys with Thermal Barrier Coating System," in *Superalloys 2008*, 2008.
- [86] V. Kuznetsov, G. Petzow and G. Effenberg, Ternary Alloys, Vol. 7, New York: VCH Publishers, 1993.
- [87] W. Kai, C. H. Lee, T. W. Lee and C. H. Wu, "Sulfidation Behavior of Inconel 738 Superalloy at 500-900C," *Oxidation of Metals*, vol. 56, no. 1-2, pp. 51-71, 2001.
- [88] J. Müller and D. Neuschütz, "Efficiency of α -Al₂O₃ as Diffusion Barrier between Bond Coat and Bulk Material of Gas Turbine Blades," *Vacuum*, vol. 71, no. 1-2, pp. 247-251, 2003.
- [89] M. W. Chase, Jr., C. A. Davies, J. R. Downey, Jr., D. J. Frurip, R. A. McDonald and A. N. Syverud, "NIST - JANAF Thermochemical Tables," National Institute of Standards and Technology, 2013. [Online]. Available: <http://kinetics.nist.gov/janaf/>. [Accessed 5 December 2015].
- [90] J. M. Andersson, "Controlling the Formation and Stability of Alumina Phases," Linköping University, Linköping, Sweden, 2005.
- [91] E. A. Brandes and G. B. Brook, *Smithells Metals Reference Book*, 7th Ed., Woburn: Butterworth Heinemann, 1992.
- [92] W. M. Haynes, *Handbook of Chemistry and Physics*, 96th Ed., New York: CRC Press, 2015.

Appendix A

Table A-1: Standard free energy of formation at 1150°C (1425K), densities and the PBR of common binary oxides of elements found in nickel-based superalloys

Oxide	ΔG° (kJ)	ln(k)	PBR	Ref
Al ₂ O ₃ (α)	-1221	103.1	1.28	[89, 90]
Al ₂ O ₃ (γ)	-1210	102.1	1.48	[89, 90]
Al ₂ O ₃ (δ)	-1215	102.6	-	[89]
Al ₂ O ₃ (θ)	-	-	1.43	[89, 90]
CeO ₂	-796	67.2	1.15	[91, 92]
Co ₃ O ₄	-368	31.1	1.97	[89, 92]
CoO	-134	11.3	1.75	[89, 92]
Cr ₂ O ₃	-762	64.3	2.00	[89, 92]
HfO ₂	-842	71.1	1.62	[91, 92]
La ₂ O ₃	-1391	117.4	1.11	[91, 92]
MoO ₂	-333	28.1	2.10	[89, 92]
MoO ₃	-412	34.7	3.26	[89, 92]
Nb ₂ O ₅	-1286	108.6	2.74	[89, 92]
NbO	-292	24.6	1.38	[89, 92]
NbO ₂	-543	45.8	1.95	[89, 92]
NiO (γ)	-113	9.5	1.69	[91, 92]
ReO ₂	-177	14.9	2.14	[91, 92]
Ta ₂ O ₅	-1430	120.7	2.43	[89, 92]
TaO ₂	-240	20.3	1.93	[89, 92]
TiO (α)	-408	34.4	1.22	[89, 92]
TiO ₂ (anatase)	-681	57.5	1.93	[89, 92]
TiO ₂ (Rutile)	-687	58.0	1.80	[89, 92]
WO ₂	-335	28.3	2.10	[89, 92]
WO ₃	-484	40.8	3.38	[89, 92]
Y ₂ O ₃	-1475	126.3	1.13	[89, 92]
ZrO ₂	-831	70.2	1.55	[89, 92]

Table A-2: Standard free energy of formation at 1150°C (1425K) and densities of common ternary oxides found in nickel-based superalloys

Element	Density (g/cm ³)	Atomic Mass	Number of electron vacancies per subshell				Group	Ref
			3d	4d	4f	5d		
Al	2.70	26.982					Metalloid	[91, 7]
Ce	6.77	140.116			13	9	Rare Earth	[91, 7]
Co	8.86	58.933	3				Transition	[91, 7]
Cr	7.15	51.996	5				Transition	[91, 7]
Dy	8.55	160.500			4		Rare Earth	[91, 7]
Er	9.07	167.259			2		Rare Earth	[91, 7]
Eu	5.24	151.964			7		Rare Earth	[91, 7]
Fe	7.87	55.845	4				Transition	[91, 7]
Gd	7.90	157.250			7	9	Rare Earth	[91, 7]
Hf	13.30	178.490				8	Transition	[91, 7]
Ho	8.80	164.930			3		Rare Earth	[91, 7]
Ir	22.56	192.217				3	Transition	[91, 7]
La	6.15	138.905				9	Rare Earth	[91, 7]
Lu	9.84	174.967				9	Rare Earth	[91, 7]
Mn	7.30	54.938	5				Transition	[91, 7]
Mo	10.20	95.960		5			Transition	[91, 7]
Nb	8.57	92.906		6			Transition	[91, 7]
Nd	7.01	144.242			10		Rare Earth	[91, 7]
Ni	8.90	58.693	2				Transition	[91, 7]
Os	22.59	190.230				4	Transition	[91, 7]
Pm	7.26	145.000			9		Rare Earth	[91, 7]
Pr	6.77	140.908			11		Rare Earth	[91, 7]
Pt	21.50	195.084				1	Transition	[91, 7]
Re	20.80	186.207				5	Transition	[91, 7]
Rh	12.40	102.906		2			Transition	[91, 7]
Ru	12.10	101.070		3			Transition	[91, 7]
Sc	2.99	44.956	9				Rare Earth	[91, 7]
Sm	7.52	150.360			8		Rare Earth	[91, 7]
Ta	16.40	180.948				7	Transition	[91, 7]
Tb	8.23	158.925			5		Rare Earth	[91, 7]
Tc	11.00	98.000		5			Transition	[91, 7]
Ti	4.51	47.867	8				Transition	[91, 7]
Tm	9.32	168.934			1		Rare Earth	[91, 7]
V	6.00	50.942	7				Transition	[91, 7]
W	19.30	183.840				6	Transition	[91, 7]
Y	4.47	88.906		9			Rare Earth	[91, 7]
Yb	6.90	173.054					Rare Earth	[91, 7]
Zr	6.52	91.224		8			Transition	[91, 7]